Nanophotonics with Optically Active Defects in Wide-bandgap Semiconductors

A thesis submitted in partial fulfilment of the requirements for the degree of Doctor of Philosophy

University of Technology Sydney

Faculty of Science

School of Mathematical and Physical Science

By

Milad Nonahal

Supervisors

Prof. Igor Aharonovich

Dr Mehran Kianinia

November 2022

CERTIFICATE OF ORIGINAL AUTHORSHIP

I, Milad Nonahal, declare that this thesis, is submitted in fulfilment of the requirements for the award of Doctor of Philosophy, in the School of Mathematical and Physical Sciences at the University of Technology Sydney. This thesis is wholly my own work unless otherwise referenced or acknowledged. In addition, I certify that all information sources and literature used are indicated in the thesis. This document has not been submitted for qualifications at any other academic institution.

Signature:
Production Note:
Signature removed prior to publication.

Date: 30.06.2022

i

Abstract

Quantum nanophotonics offers significant opportunities for all the critical areas of modern quantum technologies, including quantum information processing, quantum sensing and communication. Integrated quantum photonics (IQP) refers to an emerging class of photonic devices that can generate and control coherent quantum states of light and/or matter with quite steadily increasing complexity and scale. Based on the unique properties of quantum mechanics to encode, transmit, and process information, IQP technology provides a path to revolutionize information technology in the near future. One of the fundamental aspects of chip-scale integrated devices is the manipulation of light at the nanoscale, where a quantum emitter can create a quantum state of information. Towards such applications, a robust and high-quality fabrication technique and an efficient integration of quantum emitters are required. Herein, we explored a variety of fabrication and integration techniques for the realization of hybrid and monolithic IQP components in wide bandgap semiconductors. The drawback and benefits of each fabrication and integration techniques were highlighted, and the functionality of the fabrication technique was examined through different characterization methods in four main experimental chapters as outlined below:

In the first experimental chapter, a bottom-up method for monolithic device fabrication from polycrystalline diamond is developed with the realization of single-crystal diamond photonic structures. As a potential tool to achieve emission enhancement, quantum emitters were site-specifically generated into the photonic structure through the patterned growth method. To further explore light/matter interaction, in the following two chapters, we studied the hybrid integration of quantum emitters in 2D material into two different optical cavities resonance namely, whispering gallery modes (WGM) and bound state in the continuum (BIC) modes. We have demonstrated light/matter coupling in weak and strong coupling regimes leading to emission enhancement and rabi splitting, respectively. Finally, as a pathway for the monolithic integration of SPEs, we demonstrated different fabrication techniques to realize a set of common IQP components, including waveguides and cavities.

Acknowledgements

I consider myself extremely fortunate to work with so many intelligent, passionate, and caring people during my PhD program. First and foremost, I would like to express my sincere gratitude to my mentor Professor Igor Aharonovich for his unending patience, dedication and insightful guidance. Working with him was a turning point in my life. I learnt so many valuable lessons from him over the past years, making me forever grateful to him. He taught me how to think differently, how to be able to solve big problems and how to overcome obstacles I face not only in research but also in my everyday life.

I also would like to express my deep appreciation to my co-supervisor, Dr Mehran Kianinia, who also has taught me a lot in scientific and personal matters. Next, I would like to extend my profound appreciation to all the members of our group, Professor Milos Toth, Chi Li, Toan Trong Tran, John Scott, Johannes Froch, Blake Regan, Simon White, Minh Nguyen, Angus Gale, James Bishop, Sejeong Kim, Yongliang Chen, Thinh Tran, Rittika Rittika, Lesley Spencer, Helen Zeng, Madeline Hennessey, Otto Cranwell and Vanya Zhigulin. Without your support, I could not have finished my PhD projects. You have made the rocky path PhD journey much easier for me. I must also thank my collaborators, Dr Ha Son Tung, and Dr Do Thi Thu Ha, for all their support and fruitful discussions.

I am sincerely thankful to my parents, sister and brothers, who supported me with all their hearts from thousands of miles away.

Lastly, I would like to give special thanks to my other half, Ghazal, who provided me with unwavering support and unconditional love that helped me overcome my downs and increased the quality of my ups throughout my PhD journey.

Table Of Content

List of figures

Abbreviations

SEM	-	Scanning Electron Microscope
EBL	-	Electron Beam Lithography
FIB	-	Focused Ion Beam
RIE	-	Reactive Ion Etcher
IBE	-	Ion Beam Etcher
IQP	-	Integrated Quantum Photonics
PCC	-	Photonic Crystal Cavity
BIC	-	Bound State In the Continuum
SPE	-	Single Photon Emitter
WGM	-	Whispering Gallery Mode
TIR	-	Total Internal Reflection
ODMR	-	Optically Detected Magnetic Resonance
FWHM	-	Full Width Half Maximum
FDTD	-	Finite Difference Time Domain
SPDC	-	Spontaneous Parametric Down Conversion
1D	-	One Dimensional
HBT	-	Hanbury Brown and Twiss
2D	-	Two Dimensional
3D	-	Three Dimensional
CW	-	Continuous Wave

AFM	-	Atomic Force Microscopy
APD	-	Avalanche Photo Diode
TM	-	Transverse Magnetic
TE	-	Transverse Electric
ZPL	-	Zero Phonon Line
PSB	-	Phonon Side Band
hBN	-	Hexagonal Boron Nitride
PLE	-	Photoluminescent Excitation
QKD	-	Quantum Key Distribution
QIP	-	Quantum Information Processing
MPCVD	-	Microwave Plasma Chemical Vapor Deposition
PMMA	-	Polymethyl Methacrylate
QD	-	Quantum Dot
TMDC	-	Transition Metal Dichalcogenide
SCCM	-	Standard Cubic Centimeter
FSR	-	Free Spectral Range

List of Publications

1) **Milad Nonahal**, Simon J. U. White, Blake Regan, Chi Li, Aleksandra Trycz, Sejeong Kim, Igor Aharonovich, Mehran Kianinia "*Bottom-Up Synthesis of Single Crystal Diamond Pyramids Containing Germanium Vacancy Centers*" Advanced Quantum Technologies, 2021. **4**(7): p. 2100037.

2) **Milad Nonahal**, Chi Li, Febiana Tjiptoharsono, Lu Ding, Connor Stewart, John Scott, Milos Toth, Son Tung Ha, Mehran Kianinia, Igor Aharonovich "*Coupling Spin Defects in Hexagonal Boron Nitride to Titanium Oxide Ring Resonators*" arXiv preprint arXiv:2205.04031, 2022.

3) Mika T. Westerhausen, Aleksandra T. Trycz, Connor Stewart, **Milad Nonahal**, Blake Regan, Mehran Kianinia, and Igor Aharonovich "*Controlled doping of GeV and SnV color centers in diamond using chemical vapor deposition*" ACS applied materials & interfaces, 2020. **12**(26): p. 29700-29705.

4) Chi Li, Johannes E. Fröch, **Milad Nonahal**, Thinh N. Tran, Milos Toth, Sejeong Kim, and Igor Aharonovich "*Integration of hBN quantum emitters in monolithically fabricated waveguides*" ACS Photonics, 2021. **8**(10): p. 2966-2972.

5) Yongliang Chen, Chi Li, Simon White, **Milad Nonahal**, Zai-Quan Xu, Kenji Watanabe, Takashi Taniguchi, Milos Toth, Toan Trong Tran, and Igor Aharonovich "*Generation of High-Density Quantum Emitters in High-Quality, Exfoliated Hexagonal Boron Nitride*" ACS Applied Materials & Interfaces, 2021. **13**(39): p. 47283-47292.

6) Zhao Mu, Soroush Abbasi Zargaleh, Hans Jürgen von Bardeleben, Johannes E. Fröch, **Milad Nonahal**, Hongbing Cai, Xinge Yang, Jianqun Yang, Xingji Li, Igor Aharonovich, and Weibo Gao "*Coherent manipulation with resonant excitation and single emitter creation of nitrogen vacancy centers in 4H silicon carbide*" Nano letters, 2020. **20**(8): p. 6142-6147.

Chapter 1: Introduction

In the past few decades, quantum mechanics has revolutionized the field of information and communication technologies by employing the peculiar properties of quantum mechanics to encode, transmit, and process information. Using photons as quantum information, quantum photonics is recognized as one of the fundamental aspects of quantum science and is expected to play a major role in future technologies. The development of a fully integrated quantum photonic circuit, however, is necessary to realize the full potential of photons in quantum information technologies. In this case, a unified device consisting of different components including a single photon source, a quantum logic processor and a single photon detector must be designed and integrated into a single circuit. Through the use of photons as quantum information and manufacturing approaches based on modern nanofabrication techniques, integrated quantum photonic circuits hold the potential to reach the level of component integration and performance needed for information processing. Although a few well-established material systems and nanofabrication techniques are available for the fabrication of nanophotonic devices, development of the future quantum nanophotonics requires a large-scale material platform and fabrication technique which is currently available for the fabrication of their classical counterpart. Next-generation quantum nanophotonics will face challenges in increasing the density of integrated components, generating, and manipulating quantum information in a single device. This thesis investigates the fabrication of nanophotonic devices for on-chip applications and the integration of optically active defects within semiconductor devices. Herein, in the first two chapters, the theoretical and experimental framework are introduced and following that some of the key achievement in this work are demonstrated as outlined below.

Chapter 2 contains a fundamental introduction to the topic of integrated quantum photonics and a brief overview on its key components. This chapter also covers the basics of single photon emitters, light-matter interaction, methods of integration and nanofabrication techniques.

Chapter 3 demonstrates the possibility of bottom-up fabrication of single-crystal diamond photonic structure from a polycrystalline diamond substrate. The site-specific integration of Germanium vacancy centers into the photonic structure were achieved via the growth of diamond through the restricted apertures in the presence of germanium precursors. The functionality of the photonic structures was then examined in room and cryogenic temperature.

Chapter 4 presents the developed fabrication of suspended ring resonator and the integration of spin defect in a thin hexagonal boron nitride flake to the whispering gallery modes of the resonator. The objective of this project was to improve a scalable method for the integration of spin defect to a high-quality cavity via hybrid approach.

Chapter 5 shows the hybrid integration of quantum emitters in few-layer hBN film to the cavity mode of an array of TiO_2 nanopillars. Angle-resolved analysis of the hybrid system shows a strong coupling between the quantum emitter and the cavity photons. This was confirmed by the observation of anti-crossing behavior and Rabi splitting of the two systems.

Chapter 6 focuses on the fabrication of different types of hBN nanophotonic structures via monolithic approach. We attempt to fabricate tapered waveguide, and we successfully demonstrate integration of emitters into the waveguide via side excitation scheme. In this chapter, other nanophotonics structures such as 1D PCC and BIC grids were fabricated via a high-resolution fabrication technique.

Chapter 7 summarizes the outcome of our projects throughout this thesis and gives an overall outlook for the potential research direction towards the fabrication of integrated nanophotonics and its practical applications.

Chapter 2: Background

As a fundamental part of quantum science, quantum photonics is expected to play a key role in the advancement of future technologies. Utilizing the quantum state of light, quantum photonics is capable of controlling, encoding, and transmitting quantum information which promises revolutionized future information technology. In the following, first I will briefly introduce the Integrated quantum photonics and its components and next, the concept of single-photon emitter will be discussed followed by a detailed introduction on light-matter interactions.

2.1. Integrated quantum photonics (IQP)

With the quantum state of light, it has become feasible to demonstrate quantum mechanical experiments such as entanglement [1], squeezed states [2], retro-causality [3], and Bell inequality [4]. Photons are excellent candidate for the realization of quantum mechanical phenomena as they are weakly coupled to the surrounding environment and consequently, they do not suffer from decoherence problems. Despite the long history of quantum photonic research, recently, more attention has been paid to its potential application and practical implementations. By taking advantage of the peculiar features of quantum mechanics, quantum photonics has long been envisioned as a tool capable of going beyond the limits of current technologies.

Quantum cryptography [5], for example, prevents eavesdropping and enables absolutely secured communications. Moreover, under certain circumstances, quantum computation may become more efficient than classical counterpart by utilizing the full complexity of a multi-particle quantum wavefunction.[6] Although, these benefits have been investigated experimentally and the underlying principles are well-understood, the key challenge is to design a scalable platform for real-world deployment and commercialization. Similar to how micro-electronics revolutionized the modern world with the advent of integrated circuit, which is now the backbone of almost all electronic devices, quantum photonics requires an equivalent sophisticated platform with a large number of components to realize its full potential. Therefore, by exploiting the quantum state of light (photon) as

information carrier in conjunction with a large-scale nanofabrication technique, IQP has emerged as a powerful platform for the development of quantum technologies. Figure 2.1 illustrates the key milestones that paved the way for the development of the IQP technology and its quantum applications.
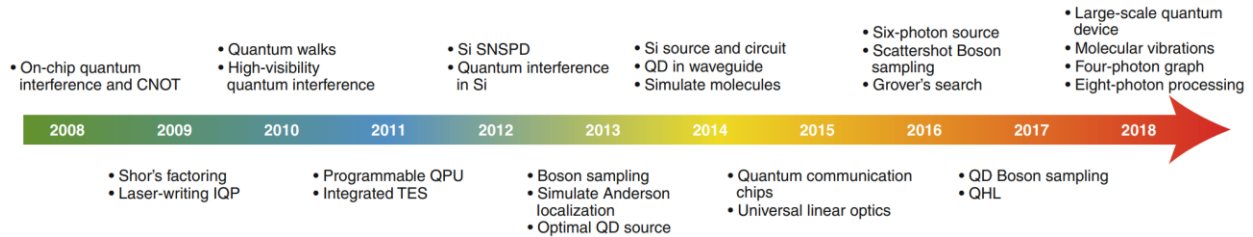
Figure 2.1. key milestones in IQP progress. The first observation of on-chip quantum interference and integrated Controlled-NOT gate [7], Shor's algorithm [8], direct laser-writing fabrication of IQP circuits, quantum walks of correlated photons [9], two-photon quantum interference, multifunctional quantum processor unit (QPU) [10], waveguide transition edge sensor (TES) [11], Si based superconducting nanowire single-photon detectors (SNSPD) [12], quantum interference in Si [13], Boson sampling with photons [14], Anderson localizations with entangled photons [15], generation of single photons from a single quantum dot (QD) [16], integration of spontaneous four-wave mixing (SFWM) sources with quantum circuits [17], coupling of QD source into waveguide [18], quantum simulation of the ground state of a molecule [19], on-chip quantum key distribution (QKD) and entanglement [20], universal linear-optic circuit [21], on-chip generation of six photons [22], scattershot Boson sampling [23], Grover's search algorithm [24], Boson sampling based on a QD [25], quantum Hamiltonian learning (QHL) algorithm [26], large-scale quantum device in Si with 670 components [27], simulation of molecular vibrations [28], four-photon graph state and silicon based generation of eight photons [29]. Reproduced from [30]

In general, the realization of above-mentioned quantum applications on IQP circuits requires three distinct components: (1) the generation of quantum state of light, (2) manipulation of the generated photons including guiding, amplifying, and interfering and finally (3) detection of the processed photon. Figure 2.2 represents a programmable integrated quantum photonic circuit being able to employ quantum algorithms for the quantum application and several examples of individual components (Figure 2.2 b to g). Although challenging, the combination of all these components into a unified system enables a new generation of powerful quantum optical processors which is promising for the future quantum computation, communication, and sensing.
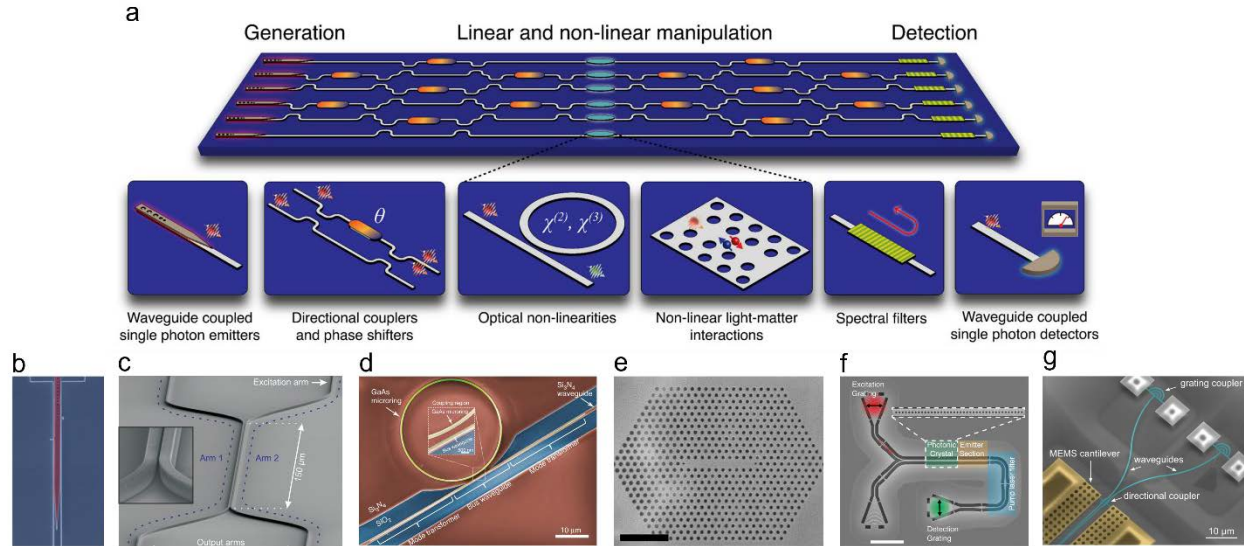
Figure 2.2. Illustration of the main IQP components. *(a) Schematic representation of device components. Reproduced from [31] (b) waveguide coupled single-photon emitter [32] (c) on-chip beam splitter and coupler [33] (d) optical ring resonator [34] (e) photonic crystal cavity [35] (f) waveguide and spectral filter [36] (g) out-coupler guiding photons toward single-photon detector. [37]*

The first element of the main building block of IQP consists of the generation of deterministic single-photon emitters (SPEs). We will elaborate upon the definition of the SPEs in the section 2.2. Briefly, to generate a coherent quantum information, single-photon sources that produce one photon at a time are required (figure 2.2 b). Next module contains linear and non-linear reconfigurable photonic elements for manipulating the generated photon through the circuit. This part is mainly constructed by a combination of low-loss waveguides from which basic manipulation including beam-splitters, filters and phase shifter can be implemented (figure 2.2 c and d). Moreover, quantum memories are another integral part of the manipulation section (figure 2.2 e). To be able to store and retrieve quantum information with high fidelity, efficient light-matter interaction is required. Under certain special conditions, photons can coherently interact with matter, thereby allowing quantum information to be effectively stored, retrieved, and reproduced. Light-matter interaction will be discussed in detail in chapter 2.4. Ultimately, following the manipulation of the photons, a sensitive single-photon detector is needed to measure the results of the process.

A variety of optical material platforms have been developed for IQP applications since different device sections require different properties for quantum photonic chips.

Depending on the application, an appropriate material platform is selected based on its photophysical properties including refractive index (for light confinement efficiency), bandgap (or transparency window). Moreover, probabilistic IQP protocols require other types of devices that exhibit nonlinearities at the level of single photons. Therefore, the crystallinity of the selected material plays an important role in the realization of nonlinear photonic devices. Some of the most relevant optical and structural properties of these materials are summarized in figure 2.3. For thorough overview on the topic of device material, the reader is referred to Kim et al. [31] and Bogdanov et al. [38].
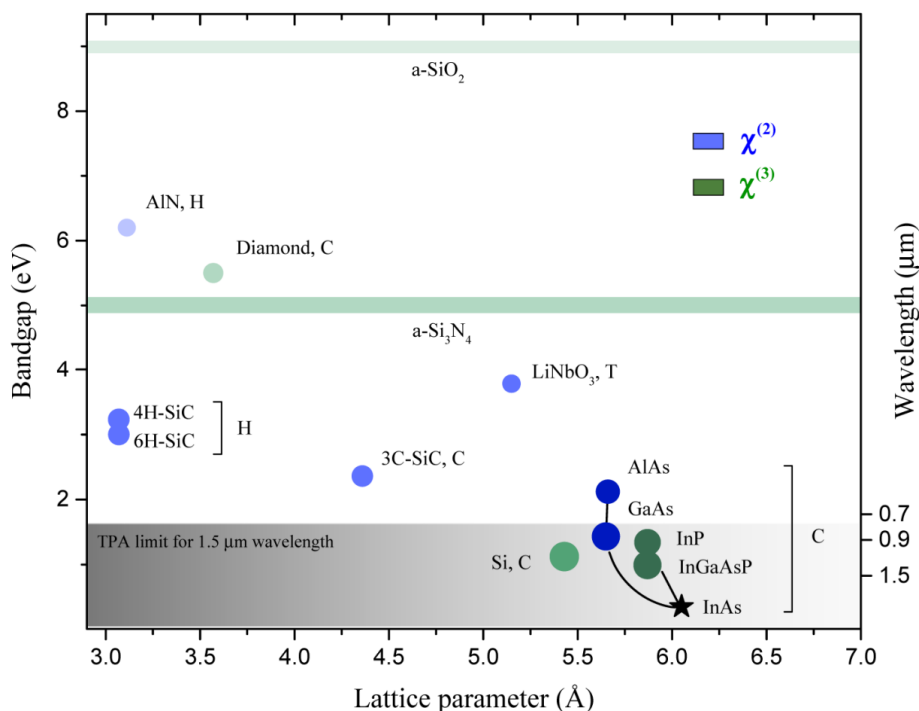
Figure 2.3. Optical properties of variety of material platforms used in IQP. Blue and Green colors correspond to second and third nonlinearities respectively. Circles represent crystalline materials whilst amorphous materials are shown with strips. The circle diameter and the strips thickness indicate refractive indices. The material crystallinities are indicated by C, H and T as short for Cubic, Hexagonal and Trigonal respectively. Reproduced from [38]

2.2. Single-photon emitter for on-chip photonics

A prerequisite for the implementation of IQP for quantum algorithms is a high-quality light source that emits individual photons at a time into a specific spatiotemporal mode. Such light source, emit identical photons, so if they are separated by a beam splitter, they

produce full interference. In general, For the most applications, an ideal single-photon emitter needs to meet three main criteria: (a) high stability (i.e. a source that does not bleach or blink) (b) high brightness or emission rate (i.e short life-time of the source) (c) high purity and indistinguishability (i.e. low probability of multiphoton emission). Over the past few decades, several processes have been studied to generate an ideal on-demand single-photon sources. In the following, I will first introduce the concept of single-photon emitter and then review different available systems with an emphasis on solid-state sources for the IQP applications and finally I will discuss over the deterministic integration of SPEs into IQP devices.

As shown in figure 2.4, an ideal single-photon source can be pictured as a two-level system wherein the electron jumps between quantized energy levels E_1 and E_2. A quantum state of light of angular frequency ω is then absorbed or emitted to satisfy:

$$E_2 - E_1 = \hbar\omega \tag{2.1}$$

The excitation of the electron corresponds to the absorption of a photon with the same energy ω, whilst relaxation of the prompted electron after a certain amount of time (known as lifetime) accompanied by the emission of a single quantum of light into the free space (figure 2.4 a). The abovementioned transitions can result in the emission of light with delta spectrum corresponding to the energy difference between E_1 and E_2, similar to that of what observed in mercury lamp (figure 2.4 b).

Even though such a two-level system is quite simple in concept, it is extremely complex in reality. The electron existing in a distinct state (ground state or excited state) is associated with a specific wave function similar to that of atomic orbitals (figure 2.4 c). Therefore, transitions between the wave functions in Fermionic particles underlies symmetry rules and thus must obey the "selection rules". As a result, the transitions involve a particular orientation of electric field known as "dipole orientation". Therefore, the absorption and emission are both equally polarization specific. In other words, the oriented dipole, emits photon with specific polarization when it relaxes to the ground state and the excitation efficiency is maximized if it receives a photon of similar polarization aligned with the transition dipole. Moreover, due to the existence of other orbitals or spin-selection rules, radiative transitions between certain orbitals are forbidden. This might

7

lead to non-radiative transitions which decrease emission efficiency (also known as "Debye Waller factor") of the emitter (figure 2.4 d).
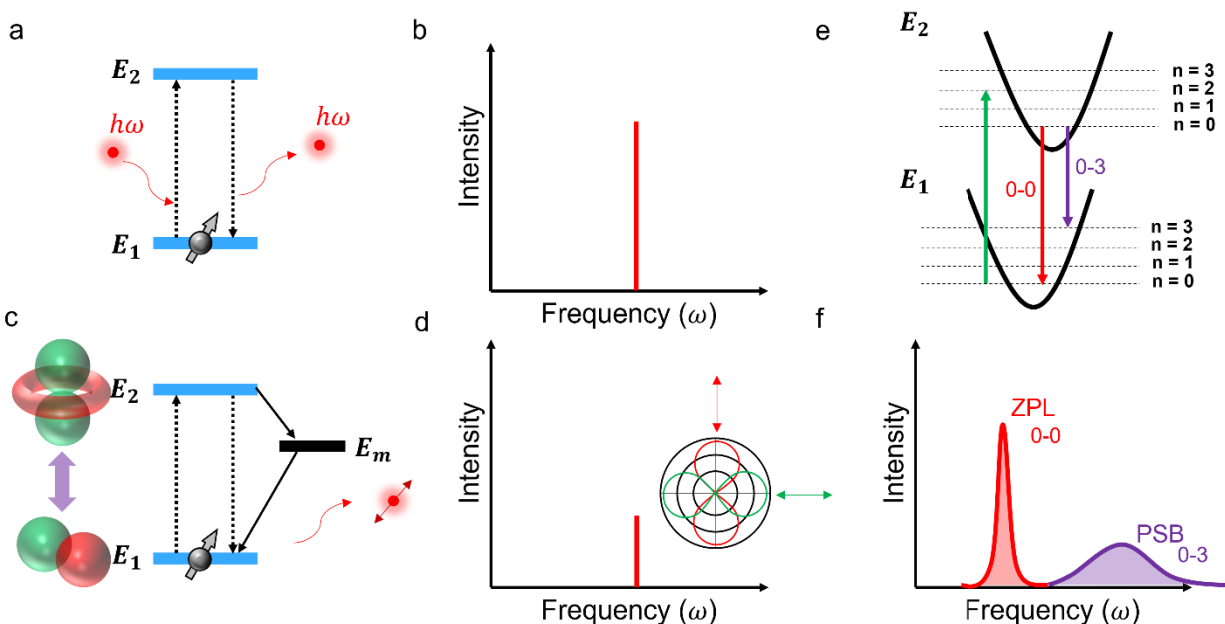
Figure 2.4. Schematic representation of a two-level system. *(a) an ideal two-level system with a delta-like transition shown in (b). (c) modified two-level system shown as atomic orbitals and intermediate energy level and its corresponding delta-like emission (d). Photons in this transition can be polarized and intensity might be decreased compared to (b) due to non-radiative transitions. (e) Franck-Condon model of energy diagram (f) more realistic spectrum of a two-level system consisting of zero phonon line (ZPL) and phonon side band (PSB).*

Having a better insight into a more realistic model of a single-photon emitter, one must consider that the ground state (E_1) may not be explicitly occupied by a single electron. Instead, a pair of electrons can exist and as a result, the atomic orbital may be related to singlet, doublet or triplet states. In this case, if an electron is added or removed from the orbital, the charge state can be changed and consequently, resulting in change in the frequency of the emitted photon (this phenomenon is also known as spectral diffusion in the literature) [39].

Moreover, the interaction of the orbital with its surrounding environment may result in broadening of the spectrum. Even for a pure two-level system, observing a delta function

is impossible owing to the uncertainty principle ($\Delta\omega\Delta t \geq \hbar/2$). Therefore, the linewidth of the spectrum is at least limited by the lifetime of the emission. The spectrum linewidth can be further broadened as a consequence of interaction with surrounding phonon bath (this phenomenon is known as dephasing) [40]. Phonons, especially in solid state single-photon emitters, may also contribute to the transition process as shown in figure 2.4 e. The zero-phonon line (ZPL) is then defined as the intrinsic difference between ground and excited state ($E_2 - E_1$, also denoted as "0-0") whilst phonon sideband (PSB) is determined by the transition where local environments are involved (e.g., 0-3). These corresponding transition spectra are shown in figure 2.4 f.

To experimentally determine a single-photon emitter, we employ Hanbury-Brown and Twiss (HBT) interferometer setup as shown schematically in figure 2.5 a. In this experiment, the incoming photon stream is separated by a non-polarizing 50:50 beam splitter and sent towards the two avalanche photodiode (APD) detectors. A clock is activated when the "start" detector receives the first photon and then is deactivated by receiving the subsequent photon at the "stop" detector. To show the coincidence of the photon's arrival, the signals recorded by the APDs are time correlated. A histogram of the coincidence versus delay is then recorded while repeating the cycle (figure 2.5 b).
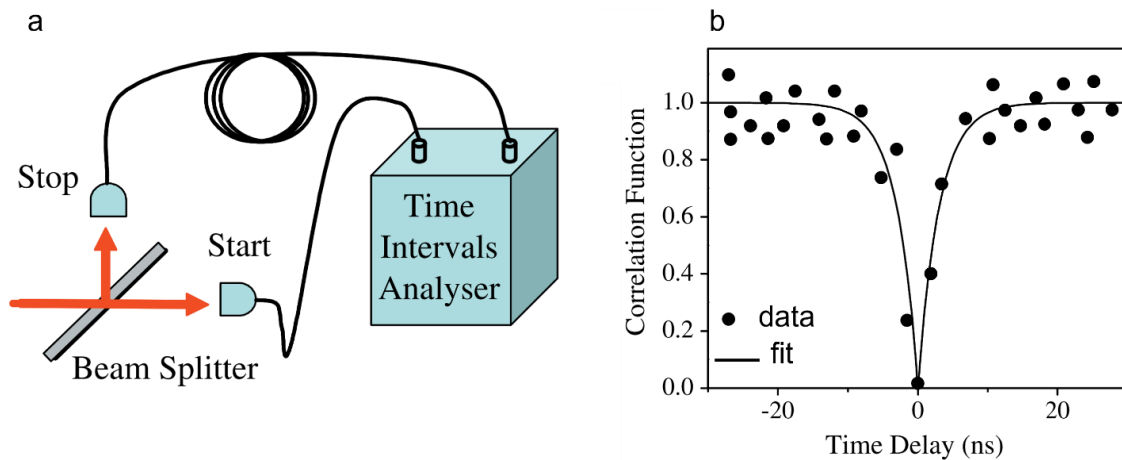
Figure 2.5. Experimental identification of a single-photon emitter. (a) Hanbury-Brown and Twiss (HBT) interferometer setup (b) second-order autocorrelation curve fitted to the histogram of arrival photons. Reproduced from [41].

We thus determine the coincidence of photon intensities using a second-order auto-correction function:

$$g^2(\tau) = \frac{<I(t)I(t+\tau)>}{<I(t)>^2} \qquad (2.2)$$

Where, I corresponds to the intensity, t is the arrival time, τ is the time interval between the two photons, respectively. From photon statistics point of view, the autocorrelation function can be derived as:

$$g^2(0) = 1 - \frac{1}{n} \qquad (2.3)$$

Where, n corresponds to photon number state. For an ideal SPE, it is expected to observe zero correlation between the two detectors at $\tau = 0$, $g^2(0) = 0$. Whilst the function is $g^2(0) = 1$ for coherent light and $g^2(0) > 1$ was observed for classic (thermal) light source as shown in figure 2.6.
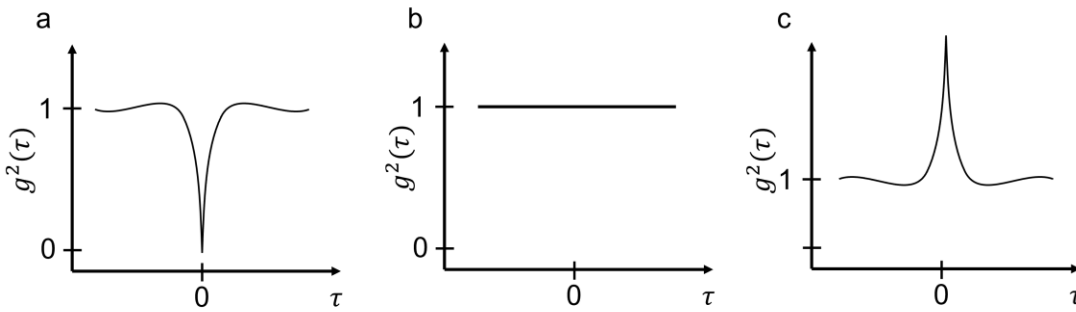
Figure 2.6. Schematic representation of autocorrelation diagram. *(a) an ideal single-photon source (b) coherent light (laser) (c) classic light source*

Over the years, numerous processes have been investigated in order to create a single-photon source. Based on the mechanism, there are mainly two types of single-photon sources. First category relies on probabilistic techniques using non-linear optics like spontaneous parametric down conversion (SPDC) and attenuated laser. The other types of single photon source are generated from a completely deterministic method such as trapped ion, cold atom and solid state based single-photon emitter. We first briefly describe the probabilistic method and then thoroughly review the second type with an emphasis on solid state single-photon emitters.

Down conversion source relies on a non-linear process in which a pair of down-converted photons with lower frequencies are generated from an incoming pulse laser. [42] Under

certain conditions, entangled photons with complementary states can be produced through this method. [43] Moreover, SPDC source can produce single-photons with high purity, indistinguishability, temporal stability and narrow linewidth. Due to its unique properties, this source is widely used in quantum applications including quantum key distribution (QKD) and quantum information processing (QIP). [44-47] However, down conversion sources are limited by their probabilistic nature of the photon generation. In this method, the brightness of the source is inversely proportional to the purity (multi-photon probability). The increase in brightness, therefore, results in a low single-photon probability, which reduces the degree of indistinguishability. [48] Additionally, the absence of spin-photon interactions presents an obstacle to its application in IQP.

One of the earliest demonstrations of a single photon source came from a transition occurring within sodium atoms as a two-level system. [49] The use of trapped ions and cold atoms as sources of quantum emission is still highly investigated thanks to the development of equipment being able to manipulate and position trapped ions and cold atoms.[50] Recently, efforts have been made towards integration of ions to electronic chips as well as integration of optically trapped neutral ions to photonic nanostructures. [51-53] Even though such sources provide on-demand and near identical qubits (they show the most resemblance to an ideal two-level system), their use in IQP still involves complicated setups for trapping and cooling ions, resulting in very slow operation rates.

As we discussed earlier, any two-level system can provide a single-photon source. With this definition in mind, another type of SPE source can be introduced which is based on atom-like defects or excitonic bound states in wide bandgap crystals as shown in figure 2.7.
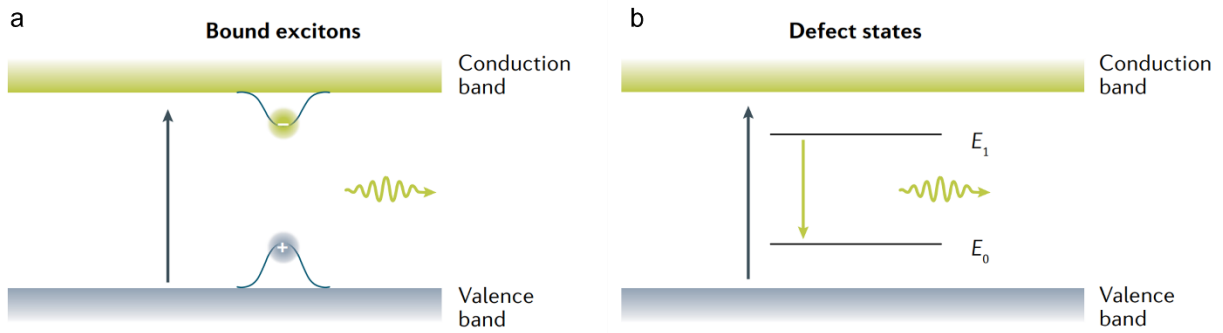
Figure 2.7. Single-photon emission mechanism in solid-state materials. *(a) excitonic bound state in semiconductors. (b) point defect in wide band gap crystal. Reproduced from [54]*

Currently, solid-state SPEs are among the most promising types of single-photon sources due to their potential for on-chip integrability as well as their spin properties, which allow application as quantum memories. [55-58] Depending on the characteristics of the emitter and the solid-state host geometry, these sources can be divided into three major categories: quantum dots, atomic defects, and bound excitons in crystals of different geometry (figure 2.8).
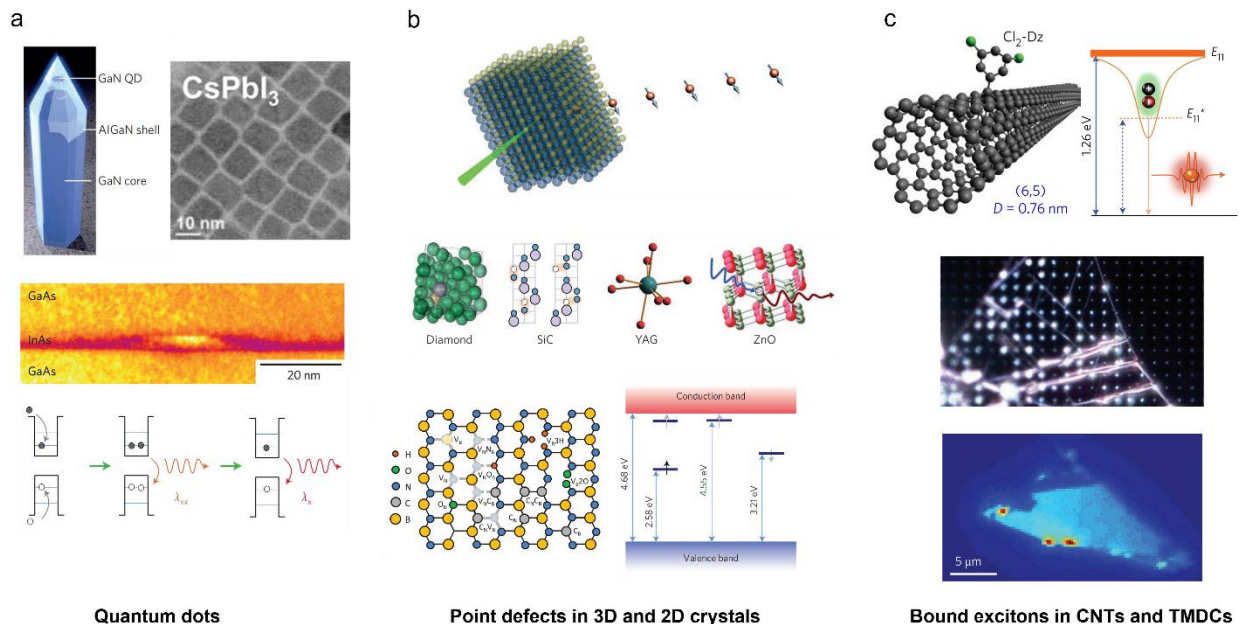
Figure 2.8. Solid-state single-photon emitters. *(a) quantum dots with confided bandgap which result in excitonic emission. (b) point defects in bulk and 2D crystals creating a two-level system within wide bandgap materials. (c) bound excitons in 1D and 2D acting as single-photon source. Reproduced from [48, 56, 59-*

63]Since the charge carriers move freely in the continuum state of semiconductors, a bandgap difference with nanoscopic features (less than exciton Bohr radius) within the bulk semiconductor, can result in strong quantum confinement. It is possible to achieve this, for instance, by altering the stoichiometry of epitaxially grown semiconductors (e.g. GaAs/InAs/GaAs quantum dot). As a result, the electrons and holes can be spatially trapped within the quantum dot region with the formation of quantized levels of conduction and valance band. Therefore, the wavefunction is spatially localized (bound state) due to Columb interaction and the resulting quasiparticle can radiatively recombine and act as a single-photon emitter (figure 2.7a). [64] More than one electron and hole trapped in a QD can produce several additional many-particle states. Biexcitons, in particular, provide a means of creating polarization-entanglement photon pairs, which are required in a variety of quantum technologies. Although they exhibit high single-photon purity, sharp emission linewidth, and the ability to generate multi-photon entangled states, they suffer from dephasing and linewidth broadening due to coupling with their environment, which severely limits their performance. [65]

Point defects in crystals, on the other hand, can be defined as spatially localized electron wave functions, which introduce discretized energy levels inside the bandgap of the host material. Sub-bandgap energy levels which are positioned far beyond the conduction and valance band can act as a two-level system (figure 2.7b). This allows us to excite these quantized transitions selectively and generate a stream of single-photon emission. [58, 63, 66, 67]

Among the most prominent examples of point defect in wide bandgap materials are color centers in diamond [68, 69], point defects in SiC [70, 71], rare earth ion (REI) doped crystals [72, 73]. Such sources offer a promising platform for the development of bright and deterministic single photon sources that are ideal for on-chip integration. However, owing to the 3D structure of these materials and the interactions with the surrounding environment, the optical properties of the defect can be significantly affected. Moreover, the extraction of photons from bulk material is quite challenging, especially from emitters embedded in high refractive index host material. Over the past decade, scientists have done extensive research aimed at minimizing these detrimental effects. The engineering

of solid-state SPEs has diversified beyond the originally studied color centers and quantum dots to include lower dimensional solid-state host materials, such as two-dimensional (2D) materials [74, 75], and carbon nanotubes (CNTs) [76].

Analogous to the point defects in the conventional wide bandgap materials such as diamond and SiC, a defect-related single-photon emitter in 2D material, namely, hexagonal boron nitride (hBN) was first reported in 2015 and caused growing interest due to its unique photophysical properties and associated spin states. [60, 77-82] There are other types of 2D hosts, including transition metal dichalcogenides (TMDCs) [83-86], in which the quantum defects are attributed to localized, weakly bound excitons mainly resulting from localized strain gradient. The effect was observed by placing the TMDCs on arrays of nanopillars for the purpose of creating site-specific emitters. [62] However, some recent studies have also demonstrated that the formation of vacancies in TMDCs crystal can also result in the generation of single emitters. [87]

In general, 2D materials are the most attractive platforms for integrated quantum photonics due to photon extraction efficiency and the ease of integration. Since the single-photon emitters are embedded in 2D structure, total internal reflection can be avoided which results in high photon extraction efficiency. Moreover, the thickness of the host material is of crucial important for device fabrication, as these require nanoscale proximity to maximize coupling efficiency which is typically difficult for SPEs in bulk crystals.
In CNTs, as 1D host, the source of single-photon emitters, are attributed to their bound excitons generated during structural manipulation. Having ZPL above 1 μm in wavelength, CNTs are promising for the integration with current telecom technologies. [61, 76, 88-91] To have a brief overview of the solid-state single-photon sources, figure 2.9 provides the common solid-state SPEs and their ZPL positions.
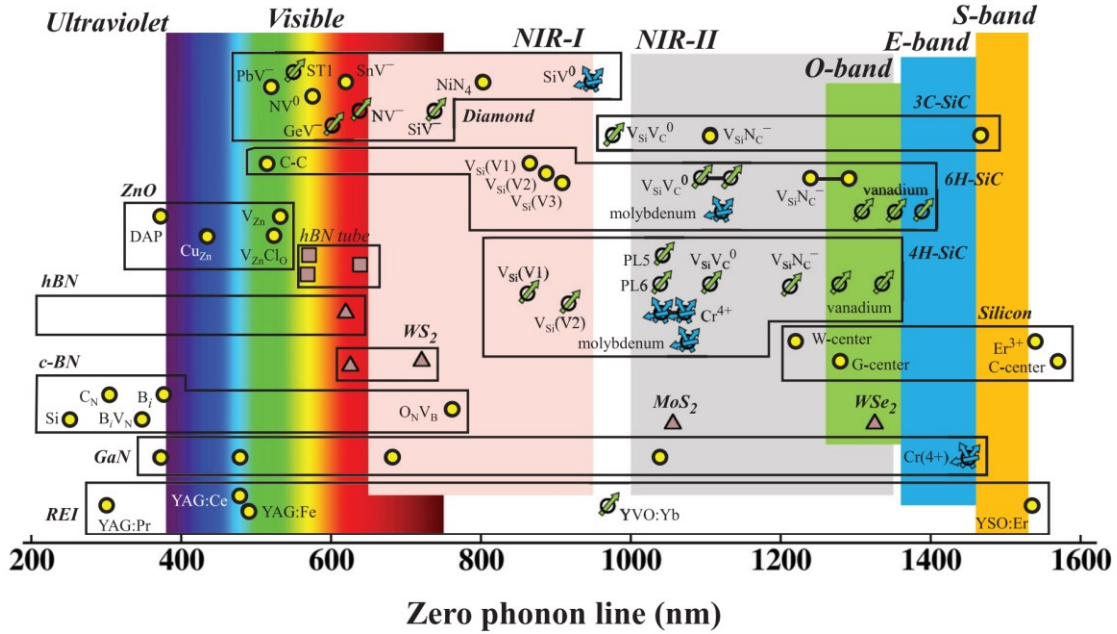
Figure 2.9. Solid-states single-photon source vs ZPL position. *Symbols are as follows: Purple squares-1D source; Purple triangle-2D source; Yellow circles-3D source. Reproduced from [63]*

2.3. Integration of SPEs to IQP devices

In addition to the generation and role of high-performance single-photon sources as quantum information in IQP, it is of equal importance to determine how to integrate these coherent sources into photonic devices in order to realize scalable quantum photonic systems. Recently, different approaches have been explored to integrate quantum emitters into IQP either through monolithic or hybrid design. The former involves generating SPE directly within functional devices fabricated from the same material (figure 2.10 a), whereas the latter relies on positioning the external quantum emitter source in close proximity to a device fabricated from different materials (figure 2.10 b).
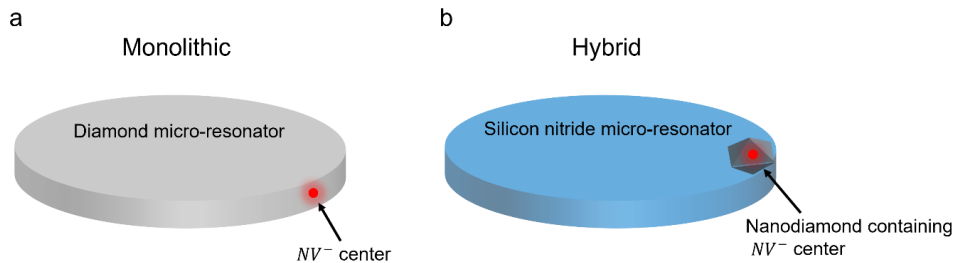
Figure 2.10. Schematic of two different SPE integration method. *(a) monolithic approach where the device material hosts the quantum emitter (b) hybrid approach; Photonic structure and quantum emitter are made up of different materials.*

15

Monolithic platforms are an ideal starting point for choosing components for an integrated quantum device since they have a very high integration potential. Several monolithic quantum photonic platforms are described in Table 2.1, as well as some of their properties and methods for generating SPEs. A key step in monolithic methods is the site-specific generation of quantum emitters. Several techniques have been developed in order to create emitters at particular locations inside the fabricated device, such as ion implantation via AFM tip, [92] focused ion beam system, [93, 94] electron beam irradiations [78] and bottom-up growth through patterned mask. [95]

Table 2.1. *Summary of the state of the art of monolithic photonic circuits as building blocks for IQPs.*

platform	Single-photon generation	bandgap	Refractive index	Operational temperature	References
Diamond	Implantation, epitaxially growth	5.5 eV	~ 2.5	Room temperature	[96, 97]
GaAs Qds	Epitaxially growth	1.42 eV	~ 3.5	Cryogenic temperature	[64]
SiC	Implantation	3.2 eV	~ 2.6	Room temperature	[98, 99]
hBN	Implantation, plasma, high Temperature	6 eV	~ 2 birefringence	Room temperature	[35, 100-103]
SiN	Probabilistic (non-linear method)	5 eV	~ 2	Room temperature	[104, 105]
Silicon	Probabilistic (non-linear method)	1.12 eV	~ 3.5	Room temperature	[106, 107]

Monolithic methods have been considered as advantageous since the emitter can be integrated specifically at the center of the device, allowing for high field overlaps.

However, materials that are suitable to host single-photon emitters may not be the best platforms for guiding and manipulating the generated photons. For example, despite the excellent capabilities of silicon photonics for guiding and manipulating photons due to large refractive index contrast, the generation of quantum emitters on this platform is limited to probabilistic methods because of its small bandgap. In contrast, TMDCs can host high-quality single-photon emitters even at room temperature, but photonic elements from these materials are not at the same maturity level as silicon photonics. Therefore, building a desired integrated quantum photonic device requires a trade-off between the ability to generate high-quality quantum emitters and achieving the best performance of photonic devices. This was the driving force for the integration of quantum emitters by

means of hybrid concept wherein each element is composed of the ideal candidate material. Figure 2.11 illustrates several common techniques to realize hybrid IQP devices.
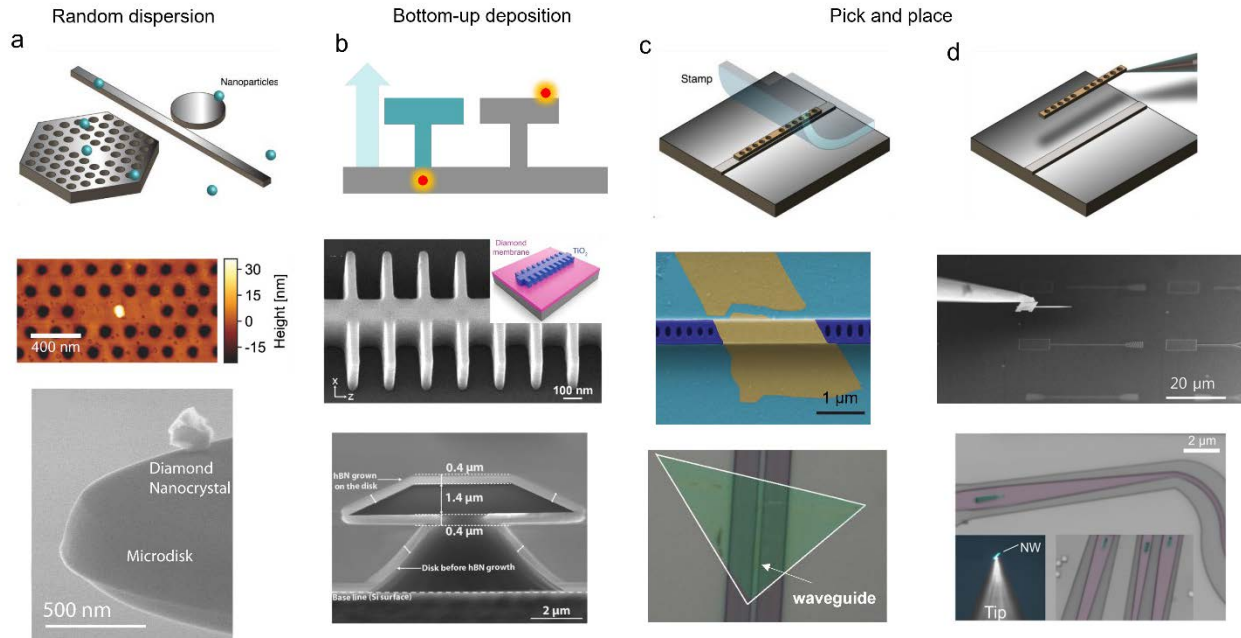
Figure 2.11. Hybrid integration of quantum emitter into IQP devices. *(a) Random dispersion of colloidal particles on photonic devices. (b) Bottom-up deposition of photonic devices onto a SPE-host material. Red shining circle represents SPE in a bulk material. (c) Align transfer method using stamp to precisely position SPE-host material onto photonic devices (d) pick and place method using a microscopic probe to place SPE materials onto photonic structures. Reproduced from [31, 108-114]*

Single-photon emitters in the colloidal nanoparticles such as nanodiamond, QDs can be readily integrated with photonic devices by drop-cast and/or spin-coating method (figure 2.11 a) [115-119]. Since quantum emitters in nanoparticles are surrounded by nanoscale material, which is smaller than the wavelength of light, thus they do not experience the problem of total internal reflection that is a major concern for those in bulk material. However, this method does not allow the emitters to be precisely positioned and instead they are randomly distributed throughout the photonic structures. As a result of such random positioning technique, there could be spatial mismatches between the quantum emitters and the field maxima of the photonic devices, and hence it might decrease coupling efficiency. Therefore, this method is not suitable for quantum photonics

applications, especially in cases where deterministic coupling of multiple quantum emitters is required. To maximize coupling efficiency, nanoparticles can be further fine-tuned by using AFM tips [120] or nanoparticles can be spread over apertures defined by the lithographic method [121].

An alternative approach is to build nanophotonic structures including dielectric or plasmonic resonators on top of SPE-host material such as diamond membrane or hBN as shown in figure 2.11 b. [122-125] As compared to dispersion, nanostructures can be deterministically built upon a predefined quantum emitter, which results in greater coupling efficiency. However, to this end, additional pre-fabrication processes are required to specify the location of the quantum emitter prior to the deposition step. Furthermore, since it was designed for bulk materials, this strategy still suffers from the TIR issue. One of the key features of this method is that it prevents micromachining and implantation, thereby preserving device and emitter quality in the final structures. A very high-quality TiO_2 cavity and waveguides have been fabricated on top on diamond membrane containing silicon vacancy defect (figure 2.11 b). [110] This strategy can also be achieved through direct writing via laser or electron beam lithography technique. [126-128]

Similarly, high-quality quantum emitters can be generated directly on a fabricated photonic platform. This hybrid structure can be achieved through epitaxially overgrown of the SPE-host material on top of the nanophotonic structure. There are several examples including overgrowth of diamond containing color-centers, hBN and QDs on photonic devices [114, 129-132]. Nevertheless, the growth of hybrid structure may have detrimental effects on the quality of the quantum emitter as the crystal quality of the host material is often compromised by the formation of antiphase boundaries, strain or dislocations caused by large mismatch between the lattice constants. Despite the challenges posed by such methods, several new approaches are being explored, such as selective area growth and defect trapping. [133, 134] As a result of the large-scale deposition of the photonic platform and growth of the quantum emitter materials, the above-mentioned integration techniques make it possible to do hybrid integration at wafer-scale.

A major advantage of the integration techniques is that it provides hybrid integration at wafer-scale due to the large-scale dispersion and deposition of the quantum emitter onto nanophotonic structures. Unfortunately, the main limitation of these methods arises from the random nature of localization of the quantum emitter to the photonic device, which reduces the coupling efficiency to a great extent. Since the spatial location of the emitter is of vital importance, numerous researchers have employed a pick-and-place method (figure 2.11 c and d) which transfers small-scale quantum emitters one by one but instead, to a very precise location. In this transfer method, the quantum emitters can be characterized prior to assembly and therefore it is possible to selectively pick the desired emitters and place them at a specific location of the photonic structure. Align transfer method (figure 2.11c) is a common example of the pick-and-place technique that uses a transparent rubber stamp coated with an adhesive layer of polymer. Since the aligned transfer method requires a high degree of accuracy, the use of transparent stamps together with a multi-axis stage enable the user to monitor the alignment process via an optical microscope in real-time. Using this method, a variety of quantum materials with different geometry including one-dimensional nanowire and 2D van der waals containing quantum emitters can be precisely transferred onto photonic nanostructures [100, 135-141]. However, aligned transfer using stamps may induce force over a large area, causing physical damages on the fragile photonic structures or may result in the detachment of other structures nearby. To achieve even higher transfer accuracy and controllability, a tip manipulator in the electron microscope system (figure 2.11 d) can be used to transfer quantum emitters onto photonic devices [113, 142-144]. With the probe tip, we can further fine-tune the position of the emitter in microscopic scale in order to maximize coupling efficiency.

2.4. SPE in a cavity

Another important component of the IQP devices, is the quantum memories, this module enables to store and retrieve quantum information which is a key requirement for quantum nodes. Moreover, some SPEs are inherently dim, as discussed before, one of the requirements for the high-performance SPE is the bright emission. These can be

achieved by placing a SPE inside a cavity. Therefore, in this chapter we will discuss how a two-level system (SPE) behaves inside a cavity.

2.4.1. Light-matter interaction

We previously explained how a two-level system absorb or emit quantum state of light in free space. In this section, we will first elaborate upon the light/matter interactions mechanism in different situations which leads us into the topic of weak and strong coupling regime. We then explore the process for a special case where a two-level system placed inside a resonant cavity.

As we know, a pure two-level system is composed of two district energy states including ground state (denoted as "$|1\rangle$") and the excited state (denoted as "$|2\rangle$") separated by $\hbar\omega$. The transition between these states (known as "$|\psi_{1,2}\rangle$") take place when it interacts with a field and can be solved by time-dependent Schrödinger equations: [145]

$$\widehat{H}|\psi\rangle = i\hbar \frac{\partial|\psi\rangle}{\partial t} \tag{2.4}$$

Where $\widehat{H}$ is the Hamiltonian of the system containing a time independent part when there is no optical field and a time-dependent potential energy:

$$\widehat{H} = \widehat{H}_0\,(\boldsymbol{r}) + \widehat{V}(t) \tag{2.5}$$

The perturbation potential can be expressed as $\widehat{V}(t) = e\boldsymbol{r}.E_0\cos(\omega t)$ when an oscillation electric field interact with the dipole and causes an energy shift in dipole. Where e is the charge of electron and E_0 is the electric field amplitude. The solution for the equation above result in a set of differential equations that shows the probability of the ground state and the excited state as a function of time:

$$\dot{C}_1(t) = \frac{i}{2}\,\Omega_R\big(e^{i(\omega-\omega_0)t} + e^{-i(\omega+\omega_0)t}\big)\,C_2(t) \tag{2.6}$$

$$\dot{C}_2(t) = \frac{i}{2}\,\Omega_R\big(e^{-i(\omega-\omega_0)t} + e^{i(\omega-\omega_0)t}\big)\,C_1(t) \tag{2.7}$$

Where Ω_R is the Rabi frequency:

$$\Omega_R = |\mu_{12}\,E_0/\hbar| \tag{2.8}$$

Here, μ_{12} is the dipole moment of the dynamic of the two states, $|1\rangle$ and $|2\rangle$. According to the equation above, the probability of the two distinct states can be then explained by their interactions with a weak or strong oscillating electric field.

When the field strength E_0 is weak, it confirms a situation that $C_1(t) \gg C_2(t)$. This shows that the two-level system is mostly in the ground state and the occupation time when the system is in the excited state is negligible (figure 2.12 a). This leads to the condition where the $C_2(t)$ decays exponentially over time. The spontaneous decay rate (γ) indicates an irreversible process wherein the probability of re-excitation of the two-level system vanishes over time as a result of interaction with a weak electric field. In contrast, when the two-level system interacts with a strong external electric field (figure 2.12 b), the decay dynamic of the system becomes completely different. In this case, the probability of the excited state $C_2(t)$ becomes comparable to the ground state $C_1(t)$ and can be defined as

$$|C_2(t)|^2 = \sin^2(\Omega_R t/2) \tag{2.9}$$

Due to the interaction with strong electric field, the transitions become reversible, and the system can be re-excited, and the decay process shows an oscillatory behavior. The sin function indicates how the probability of the excited state oscillates as a function of time and Rabi frequency. As shown in figure 2.12, the amplitude of the incident field defines the decay dynamic of the two-level system. The damping effect of the decay process in the coherent interaction (Rabi oscillation), results from dephasing processes including spontaneous decay of the excited state γ. The Rabi oscillation (coherent interaction with the field) becomes noticeable when field strength is much larger than the losses $\Omega_R \gg \gamma$. The probability of the excited state defines the final spectral shape. The interaction with a weak field exhibits a Lorentzian spectrum associated with the spontaneous decay of the excited state where the linewidth of the spectrum corresponds to the decay process rate γ. In contrast, when a two-level system interacts with a strong field and the oscillation frequency becomes greater than losses, the spectrum becomes broader and eventually displays two Lorentzian peaks. This is due to a phenomenon called hybridization, which will be discussed later in the section on SPE in a cavity.
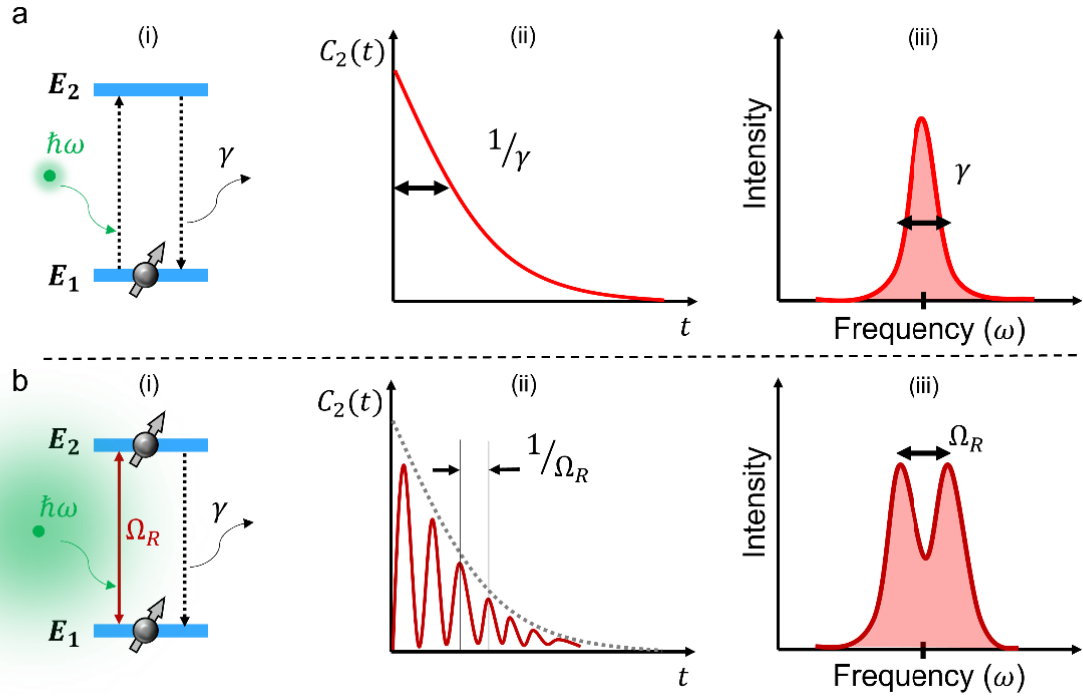
Figure 2.12. Schematic representation of light-matter interaction *(a) a two-level system is excited by a (i) weak oscillating field which is followed by a (ii) decay process at rate of γ. (iii)The probability of the excited state is decaying exponentially and results in a spectrum with Lorentzian shape. (b) interaction of a two-level system with a (i) strong field resulting in an (ii) oscillatory behavior of the decay dynamic of the excited state. (iii) Rabi splitting is observed in the spectrum arising from hybridization.*

2.4.2. Optical cavity

Before explaining the light-matter interaction behavior inside a cavity, we shall briefly introduce the basic properties of an optical cavity.

A well-known example of an optical cavity is a system in which multiple electromagnetic modes can be spatially confined or localized within a set of separated reflecting mirrors. Optical modes resulting from these systems can be identified by their resonance wavelength, spectral linewidth, or lifetime. The mechanism of localizing electromagnetic waves can be vastly different depending on the material and size of the optical resonator. The most common type is made up of two reflecting mirrors facing each other separated by a few microns.[146] Nanoscale type of optical cavities can be achieved by creating optical bandgap in photonic crystals in 1D, 2D or 3D configuration with a size comparable to the wavelength of confined electromagnetic field. [147] Finally, the sub-wavelength

optical resonator can be achieved by the concept of surface plasmon or Mie scattering. The former can be regarded as photons bound to an oscillating electric field on the surface of metal, while the latter is based on the scattering of the electromagnetic field when it interacts with a sub-wavelength object. Consider a planar cavity composed of two reflecting mirrors as M_1 and M_2, separated by a dielectric medium with a refractive index n at a distance of L_{cav} and reflectivity of R_1 and R_2, respectively as shown in figure 2.13 a. This type of cavity is also known as Fabry-Perot interferometer which is frequently used in high-resolution spectrometer. In order to analyze the properties of the cavity, we introduce an electromagnetic field with wavelength of λ from one side and we measure the transmission from the other side. If there is no absorption of scattering inside the cavity, the transmission can be defined by:

$$\mathcal{T} = \frac{1}{1+(4\mathcal{F}^2/\pi^2)\sin^2(\phi/2)} \tag{2.10}$$

Where $\phi = \frac{4\pi n L_{cav}}{\lambda}$, is the round-trip phase shift and $\mathcal{F} = \frac{\pi(R_1 R_2)^2}{1-\sqrt{R_1 R_2}}$, corresponds to the finesse of the cavity. The cavity is said to be on-resonance if $\phi = 2\pi m$ ($\mathcal{T} = 1$), where m is an integer number indicating the resonance modes (figure 2.13 b). From the phase shift definition, we can infer that the resonance condition takes place whenever the cavity length $L_{cav} = m\lambda/2n$ and thus the angular frequencies of the resonant modes can be introduced as

$$\omega_m = m\frac{\pi c}{n L_{cav}} \tag{2.11}$$

From the equation we can infer that the modes frequency can be tuned by changing the cavity size (L_{cav}) of the medium refractive index (n) which a key parameter in designing a cavity. The resonance condition occurs when the bouncing light is in phase during each round trip resulting in constructive interference. The linewidth of each mode can be calculated by considering the situation in which $\mathcal{T} = 0.5$. Therefore, the phase shift can be extracted from the equation 2.10 which is $\phi = 2\pi m \pm \pi/\mathcal{F}$ and the full width at half maximum (FWHM) is then equal to $\Delta\phi_{FWHM} = 2\pi/\mathcal{F}$. As the phase shift is proportional to the mode frequency ($\phi = \frac{4\pi n L_{cav}}{\lambda}$) , we can show the relationship between the spectral linewidth of the modes to the cavity characteristics:

$$\frac{\Delta\omega}{\omega_m - \omega_{m-1}} = \frac{\Delta\phi_{FWHM}}{2\pi} = \frac{1}{\mathcal{F}} \tag{2.12}$$

We can then combine equation 2.11 and 2.12 giving

$$\Delta\omega = \frac{\pi c}{n \mathcal{F} L_{cav}} \tag{2.13}$$

From the equation, it is evident that sharp resonance modes can be achieved by a high finesse cavity.
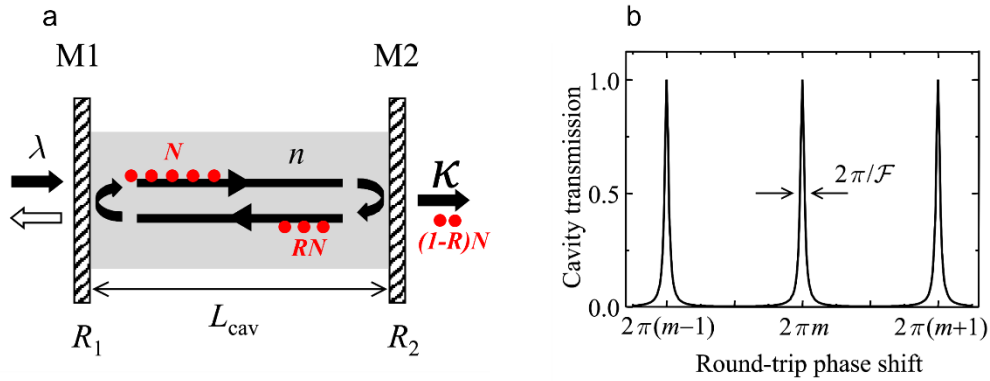
Figure 2.13. Optical cavity. *(a) mechanism of light confinement in a planar cavity. (b) transmission measurement of the cavity shown in (a). Reproduced from [148]*

Considering the reflectivity of the mirrors smaller than 1, the bouncing trip of the photons inside the cavity leads to a gradual loss over time. With an initial number of N photons occupying the cavity, the number of photons is reduced with each event of reflection by a factor of $(1 - R)$. Due to the non-perfect mirrors, we lose, on average, $\Delta N = (1 - R)N$ after a time $t = nL_{cav}/c$. Thus, the rate of loss can be written as

$$\frac{dN}{dt} = -\frac{\Delta N}{nL_{cav}/c} = -\frac{c(1-R)}{nL_{cav}} \tag{2.14}$$

The solution yields

$$N(t) = N_0 \exp(-t/\tau_{cav}) \tag{2.15}$$

Where, τ_{cav} is the photon lifetime inside the cavity and can be expressed as

$$\tau_{cav} = \frac{nL_{cav}}{c(1-R)} = \frac{1}{\kappa} \tag{2.16}$$

Here, κ is the average photon loss rate. From the definition for finesse with R~1 and equations 2.13 and 2.16, we can find:

$$\Delta\omega = (\tau_{cav})^{-1} \equiv \kappa \tag{2.17}$$

From the eq. 2.17, we can conclude that the photon loss rate can control the linewidth of the resonant modes and linewidth represents the quality of light confinement. The main

properties of a planar cavity are governed primarily the cavity finesse $\mathcal{F}$ which is able to control both linewidth and the loss rate. However, this parameter is helpful when dealing with a planar cavity. In order to be able to specify the properties of general cavities, a more versatile parameter can be introduced as the quality factor (Q) or Q-factor, defined by

$$Q = \omega/\Delta\omega \tag{2.18}$$

2.4.3. SPE-Cavity coupling

After reviewing the mechanism of light-matter interaction and the properties of an optical cavity, now we can elaborate upon how a two-level system behave inside a cavity. As shown in figure 2.14, we start with an assumption that a two-level system is located inside a cavity in a way that it can absorb photons from the cavity modes and emit radiatively into the cavity. As the cavity supports multi-modes, we will discuss a special case in which the transition frequency of the two-level system (denoted as "ω_p") is equal to one of the cavity modes (denoted as "ω_m"). In this case, the two-level system and the cavity can exchange energy resonantly and the transition of the two-level system is significantly affected by the interaction with the cavity light field. The cavity-coupling interactions are determined not only by the coincidence of frequencies but also by the spatial positioning of the two-level systems and the matching of polarizations. But for now, we assume that the only parameter that affect the coupling strength is the matching of the frequencies. The resonance condition can be achieved by tuning the cavity in a way that one of the cavity modes (ω_m) overlaps with the transition frequency (ω_p) which is a fixed parameter. In this case, the relative strength of the SPE-cavity coupling is defined by the following parameters: (a) the average photon loss rate (κ) (i.e., the amount of photon that escape from the cavity due to non-perfect light confinement), (b) the off-resonant transitions (γ) (i.e., the number of photons emitted to free-space), (c) the coupling parameter (g_0) (i.e., the coupling strength between the two-level system and confined light field). These are schematically illustrated in figure 2.14.
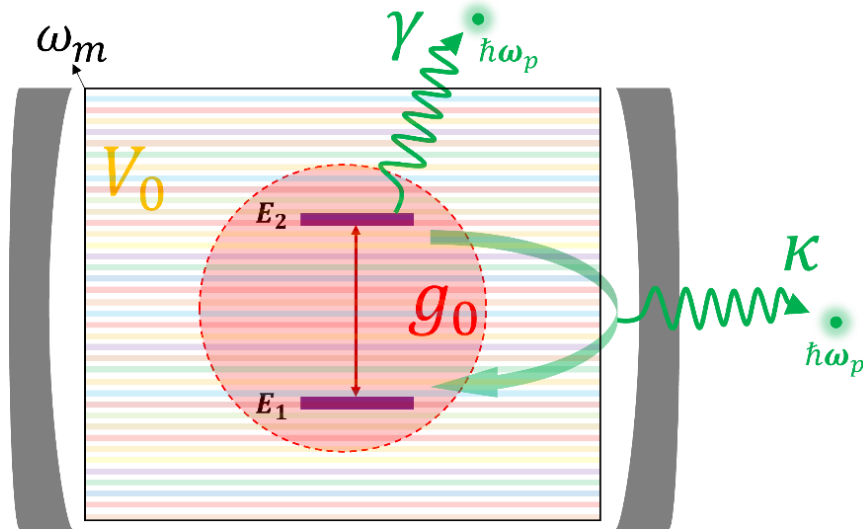
Figure 2.14. Schematic illustration of a two-level system inside a cavity. ω_m *is a set of modes supported by the cavity with modal volume V_0. the coupling strength is characterized by g_0, κ and γ which corresponds to the coupling parameter, photon loss rate and off-resonant transitions respectively. The two-level system emit photon with frequency ω_p that can be coupled to one of the cavity modes (in case of multi-mode cavity).*

As the dynamic of the coupled systems is characterized by the above-mentioned parameters, therefore, the interaction strength is in the "strong coupling" regime whenever $g_0 \gg (\kappa, \gamma)$ and the in contrast, the system is in "weak coupling" regime if $g_0 \ll (\kappa, \gamma)$. In general, in the weak coupling regime, the transition of the two-level system is an irreversible process, similar to that of spontaneous emission in the free space. However, the transition rate is influenced by the "photon density of state" as a result of being inside a cavity (supports few modes resulting in high density of state) rather than free-space (supports infinite number of modes resulting in lower density of state). In contrast, the transition process in the strong coupling regime is reversible because the interaction between cavity field and the two-level system is way faster that photon loss rate. Therefore, the emitted photon can be re-absorbed by the two-level system before it escapes from the cavity (this is indicated by a green and transparent arrow in figure 2.14). Before explaining the two regimes, it is necessary to quantify the parameters. The photon loss rate (κ), is related to the cavity properties as shown in eq. 2.17, and it can be rearranged from eq. 2.17 and 2.18 into:

$$\kappa = \omega/Q \qquad (2.19)$$

From eq. 2.19, we can conclude that the photon can be confined better (low loss rate) in a high-Q cavity.

The off-resonant transition (γ) can be explained by two scenarios. Firstly, the two-level system as a dipole can emit photons with same frequency as the cavity mode but not into the cavity and instead it emits, for example, into the free-space as shown in figure 2.14. Secondly, due to the deviation from an ideal two-level approximation (as we explained earlier in figure 2.4 c), the two-level system can decay to a different energy level emitting off-resonant photons or it scatters to other states and decay non-radiatively (heat). We consider the former as the dominant case and can be expressed as:

$$\gamma = \frac{A_{21}(1-\Delta\varrho/4\pi)}{2} \tag{2.20}$$

Here, A_{21} is Einstein A coefficient and is equal to $1/\tau_{exc}$, where τ_{exc} corresponds to the excited state lifetime. The factor $\Delta\varrho$ is related to the fraction of photons that are emitted from the dipole at angles and escaped from the cavity which is also known as cavity subtended angle.

Having reminded ourselves of the light-matter interaction (section 2.4.1), we can now quantify the final parameter known as coupling parameter (g_0). We earlier discussed about how a two-level system behave when it interacts with and external light field. Here, instead of light field, we are analyzing the interaction of the two-level system with the vacuum fluctuations (or zero-point fluctuations) of the of the electromagnetic field existing inside the cavity. The energy of the interaction can be defined as

$$\Delta E = |\mu_{12}\,\xi_{vac}| \tag{2.21}$$

Where, μ_{12} is the dipole moment of the two states ($|1\rangle$ and $|2\rangle$) and ξ_{vac} is the vacuum field magnitude and is expressed as

$$\xi_{vac} = \sqrt{\hbar\omega/2\epsilon_0 V_0} \tag{2.22}$$

Here, ϵ_0 is the electric permittivity. From this equation we can infer that the vacuum field is greatest for small cavities. By setting the interaction energy ΔE equal to $\hbar g_0$, then we have:

$$g_0 = \sqrt{\frac{\mu_{12}{}^2\omega}{2\epsilon_0 V_0\hbar}} \tag{2.23}$$

This equation tells us the coupling parameter can be controlled by dipole moment, frequency, and the cavity modal volume.

2.4.4. Weak coupling regime

Weak coupling regime take place whenever the coupling parameter is much smaller than loss rates. Photons are, therefore, lost from the cavity much faster than interaction time between the two-level system and the cavity mode. The transition of the two-level system is, therefore, irreversible exactly similar to that of emission into the free-space. In this condition, the dissipation dominates over the dynamic of the coupled system and the coupling between the two systems can be somehow ignored. As a result, they are nearly uncoupled, and from the quasi-classical point of view, the two-level system and the cavity can be considered as two unrelated harmonic oscillators and they retain their individual properties (figure 2.16 a). However, in the weak coupling regime, the main effect of the cavity is to change the photonic density of state and consequently, it enhances or suppresses the spontaneous emission rate of the two-level system. A two-level system in excited state cannot decay to a lower state unless it interacts with a radiation field. This leads us to the conclusion that the spontaneous emission rate is not an intrinsic property of the two-level system but rather it is governed by its environment. The spontaneous emission rate of a two-level system in free-space was first proposed by Weisskopf and Wigner [149] and defined as

$$\Gamma_0 = \frac{\omega_0^3 \mu_{12}^2}{3\pi\varepsilon_0\hbar c^3} \tag{2.24}$$

And the modified spontaneous emission rate for a two-level system that is not placed in free space was found to be

$$\Gamma_m = \frac{2\pi\mu_{12}^2 E_0^2}{\hbar^2} \rho(\omega_0) \tag{2.25}$$

Here, E_0 is the electric field formed by the emitted photon and $\rho(\omega_0)$ is the photon local density of states at frequency ω_0. The local density of state can be intuitively defined as the number of radiation modes, per unit frequency and volume which is available for the two-level system to decay into (figure 2.15).
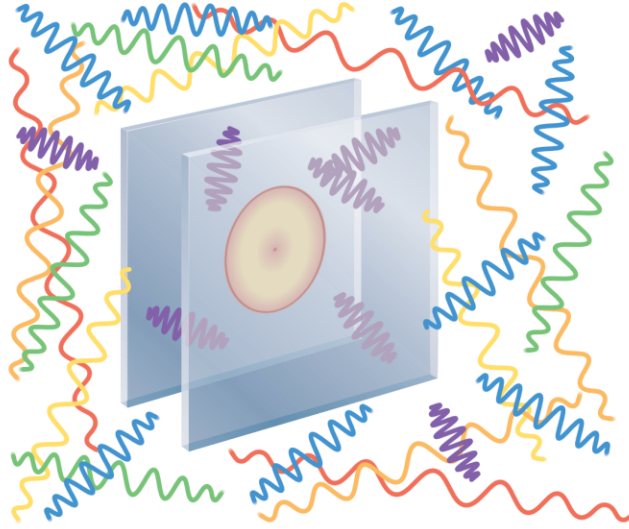
Figure 2.15. Schematic example of local density of states for a two-level system located in a parallel cavity. *The density of a photonic state inside a cavity is higher than surrounding free space leading to higher spontaneous emission rate. Reproduced from [150]*

In 1946, Purcell made the first proposal about modified spontaneous emission rate. He suggested that the rate of nuclear magnetic transition of an atom would be increased when it is placed inside a cavity. [151, 152] At resonant condition where the cavity mode coincide with the transition frequency, the ratio of the modified (eq. 2.25) over the free-space (2.24) spontaneous emission rate has become known as Purcell factor:

$$F_p = \frac{\Gamma_m}{\Gamma_0} = \frac{3Q\lambda^3}{4\pi^2 V_0} \tag{2.26}$$

The effect of a cavity of transition rate can be characterized by Purcell factor. If $F_p > 1$, the spontaneous emission is enhanced by the cavity confinement and $F_p < 1$ indicates the transition of the two-level system is inhibited by the cavity confinement. From the eq. 2.26, we can also conclude that a large Purcell factor can be achieved by a high-Q cavity with small mode volumes. In a nutshell, in weak coupling regime, where the two systems (cavity and dipole) are poorly coupled, we can consider them as two independent systems. However, a two-level system inside a cavity behaves differently even though the coupling is weak. The spontaneous emission rate could be enhanced due to the large density of states at the cavity modes or by contrast, it can be inhibited due to the absence of resonance photon modes inside the cavity wherein the two-level can decay.

2.4.5. Strong coupling regime

Strong coupling regime emerges if the coupling rate (g_0) is much larger than the photon loss rate (κ, γ). Consequently, the two-level system inside the cavity can re-absorb the photon that was just emitted as a result of the transition. In other words, the two systems are interrelated, and they exchange energy. This condition result in a coherent state where the two-level system is in the superposition of $|e, 0\rangle$ (excited sate and no photon) and $|g, 1\rangle$ (ground state and one photon). This level of interaction leads to a situation known as hybridization which is a central feature to our understanding the topic of cavity quantum electrodynamic.

The hybridization into a new state (also known as dressed state) was first proposed by Jaynes and Cummings in 1963. [153] The Jaynes-Cummings model theoretically describes strong light-matter interaction based on the consideration of the systems as a full quantum mechanical model. To have a better insight into this model and to have more intuitive understanding of the physics behind the strong coupling regime, it is also possible to consider the two interacting systems as two coupled harmonic oscillators. Each oscillator with equivalent masses $m_1 = m_2 = m$ and spring constant $k_1 \neq k_2$ has eigenfrequencies of $\omega_i = \sqrt{k_i/m}$ as shown in figure 2.16. If both oscillators interact by another spring (figure 2.16 b) with a constant of g_0, the system can be described as

$$m\ddot{x}_1 + k_1 x_1 + g_0(x_1 - x_2) = 0 \tag{2.27}$$
$$m\ddot{x}_2 + k_2 x_2 - g_0(x_1 - x_2) = 0 \tag{2.28}$$

The solution of these equations results in a set of eigenfrequencies as

$$\omega_\pm^2 = \frac{1}{2}\left[\omega_1^2 + \omega_2^2 \pm \sqrt{(\omega_1^2 - \omega_2^2) + 4\beta^2 \omega_1 \omega_2}\right] \tag{2.29}$$

Where $\omega_j = \sqrt{(k_j + g_0)/m}$ and $\beta = g_0/(m\sqrt{\omega_1\omega_2})$. In the case where $g_0 = 0$, the two eigenvalues are reduced to the initial frequencies ω_j. The two oscillators moving independently (figure 2.16 a-i) and therefore each system retain its properties (figure 2.16 a-ii) and the corresponding spectrum exhibits a single peak associated with either system (ω_j) as shown in figure 2.16 a-iii. This is exactly similar to that of weak coupling regime where the photon loss rate is much larger than coupling rate and we can assume $g_0 \sim 0$. On the other hand, if the coupling strength is much larger than the photon loss rate and if the two system are at resonance and oscillate with same frequencies ($\omega_1 = \omega_2 = \omega$), we

can consider that the two oscillators are connected with a strong spring (g_0), the eq. 2.29 reduces to

$$\omega_{\pm} = \omega \pm g_0 \tag{2.30}$$

This gives rise to two solutions for the coupled system. One with lower energy than the uncoupled frequency (ω) where the coupled systems oscillate in-phase (ω_-) and one with higher energy than ω, when oscillation is in out-of-phase as shown in figure 2.16 b-i. In the strong coupling regime, the systems are no longer independent and g_0 prevents a crossing of the two eigenfrequencies $\omega_{\pm}$ (figure 2.16 b-ii) and the resulting spectrum shows a double peak associated with the two eigenmodes (figure 2.16 b-iii) which is also known as "vacuum Rabi splitting". The anti-crossing behavior and the splitting in spectrum form a very persuasive body of evidence for the strong coupling regime. In other words, in this regime, systems are neither a two-level system nor a photon (light field), but instead they are in a hybridized coherent state which is also known as polariton. Polaritons therefore, give rise to a Rabi oscillation as they are in superposition of two states as explained earlier in the light-matter section (figure 2.12 b). Although, such phenomenon is purely quantum mechanical effect and there is no classical analogue, the classical explanation intuitively clarifies, for example, why we observe splitting or anti-crossing.
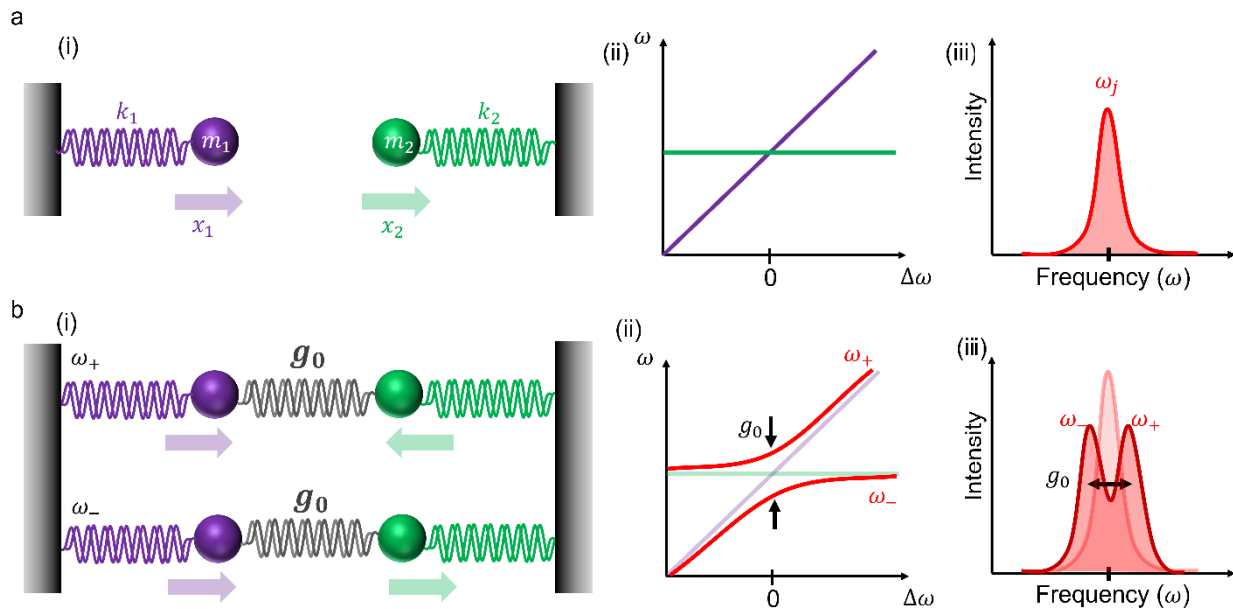

Figure 2.16. Classical description of weak and strong coupling regime by considering the two systems as two harmonic oscillators. *(a) uncoupled systems (weak coupling regime) where the two oscillators behave independently as a result of (ii) energy detuning between the two oscillators resulting in*

(iii) a single peak spectrum with oscillating frequency ω_j. (b) coupled system oscillating out-of-phase (top) and in-phase (bottom). The arrows indicate the oscillation directions. The coupled springs (i) prevents crossing in the (ii) energy detuning curve and resulting in a (iii) double-peak spectrum separated by the coupling strength (g_0). The stronger coupling leads to a further separation. Green and Purple solid lines in (ii) correspond to cavity and photon as two oscillators respectively.

2.5. Nanofabrication techniques

In the previous sections, we reviewed the quantum photonic devices and the necessity of single photon emitters in IQP as well as integration methods. In this section we review some of the well-known techniques employed in the fabrication of integrated quantum photonics and the main advantages and disadvantages will be explained. In addition to the integration technique, the realization of high quality nanophotonic devices through a reliable fabrication method is another critical step in the development of large-scale IQP circuits. To this end, a deterministic and scalable fabrication technique is necessary to realize fully isolated structures to confine light at nanoscale. These fabrication techniques can be generally categorized into bottom-up and top-down approach.

Through the bottom-up method, the nanophotonic structures can be built upon a foreign material or homoepitaxially overgrown through predefined patterns [154, 155]. Bottom-up approach have been utilized for the fabrication of a variety of nanophotonic structures with different geometry from silicon [156], GaAs [157], diamond [158] and so forth as shown in figure 2.17. Although this technique is a straightforward and powerful tool for the fabrication of high-performance devices, it is limited to few materials. The main advantages of such techniques are: (a) the ability to engineer complicated geometries that are somehow impossible to achieve through the top-down etching method. (b) a variety of SPEs can be integrated into the photonic devices simultaneously during the fabrication process. (c) the quality of the material can be retained (atomically smooth top and side walls) as the photonic structures do not experience ion milling or etching that introduce damages to the host crystal. However, such method still suffers from the lack of precise positioning of SPE emitters, as they are introduced during the growth. Moreover, the fabrication of fully suspended structure is still challenging, since this bottom-up method requires a supporting material whereon the structures are grown.
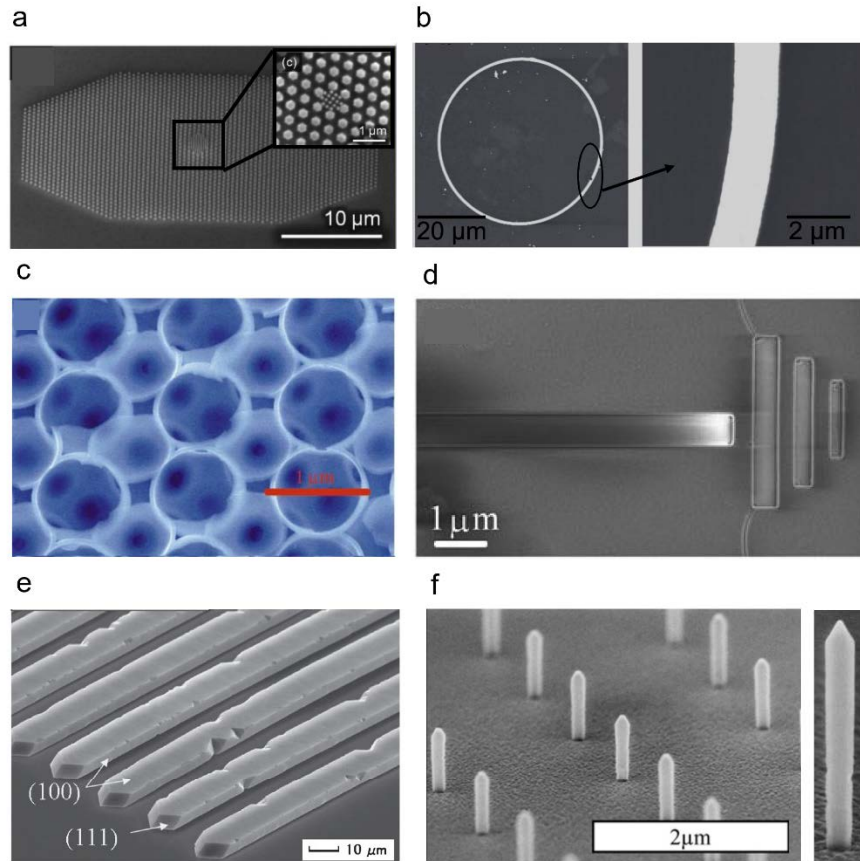
Figure 2.17. Photonic structures fabricated via bottom-up technique. *(a) GaAs photonic crystal cavity overgrown through SiNx mask. (b) diamond ring resonator containing SiV color centers hetero-epitaxially overgrown on Iridium substrate. (c) Silicon Inverse opal photonic crystal showing photonic bandgap at 2.5 μm. (d) diamond waveguide and coupler overgrown from diamond membrane through silica patterned mask. (e) single-crystal diamond waveguides hetero-epitaxially overgrown on Ir/MgO substrate. (f) Pillar microcavity grown through patterned silica substrate. Reproduced from [95, 134, 154, 159-162]*

The top-down approach, on the other hand, is more versatile and instead of building up the structures, it breaks down and sculpt the nanophotonic structure into a bulk material. The bulk material is etched away using reactive ions (or chemical etching) and/or by inert species which is also called physical milling. The former is mostly performed via a process called Reactive Ion Etching (RIE) and the latter is achieved by accelerated non-reactive species such as Ion beam etcher (IBE). These methods are a wafer-scale fabrication method, and they routinely require a hard mask to protect the patterned area from milling process. Thus, in this method the first thing to be achieved is the definition of a patterned mask. In the most cases, the patterns are introduced by means of lithography process

such as UV or electron-beam lithography (EBL) [163]. For both cases, a UV or electron sensitive material (mostly polymer) is exposed by the beam of light or electron and the pattern appeared after a process called development as shown in figure 2.18 a. Depending on the feature size and the chemical/physical selectivity of the bulk material, the polymer can be used as hard mask or alternatively a metal mask can be employed through a liftoff process. After defining the pattern, the material is subject to the reactive or non-reactive species to be non-isotropically etched away (figure 2.18 a) [164]. On the other hand, the nanophotonic structures can be sculpted using direct writing method such as Focused ion beam (FIB) milling. [165, 166] Unlike RIE etching method, FIB is utilizing a focused beam of non-reactive ions such as Ga or Xe, and this is useful for the fabrication of nanophotonic structure in some special place and not applicable for large-scale fabrications. Several examples of the top-down etching method have been illustrated in figure 2.18. The top-down etching method is vastly used for the fabrication of nanophotonics owing to its versatility and compatibility with other methods. For example, due to the commercial availability of multilayer wafers (SiN_x on silicon), it is possible to fabricate fully-suspended structures through selective etching with different reactive species resulting in better light confinement. However, the top-down method relies on long etching/milling steps that hinders the quality of photonics material. Although, crystal quality can be recovered by high temperature annealing, temperature history might also affect other physical or optical properties of the final device.

a

E-beam/light

Reactive/inert species

Sensitive polymer

Device material

b

1μm

200 nm

c

laser out

laser out

laser in

d

1μm

e

f

Resist

WS₂ nanodisk

500 nm

g

y

x

1 μm

a_x = 0.83 μm
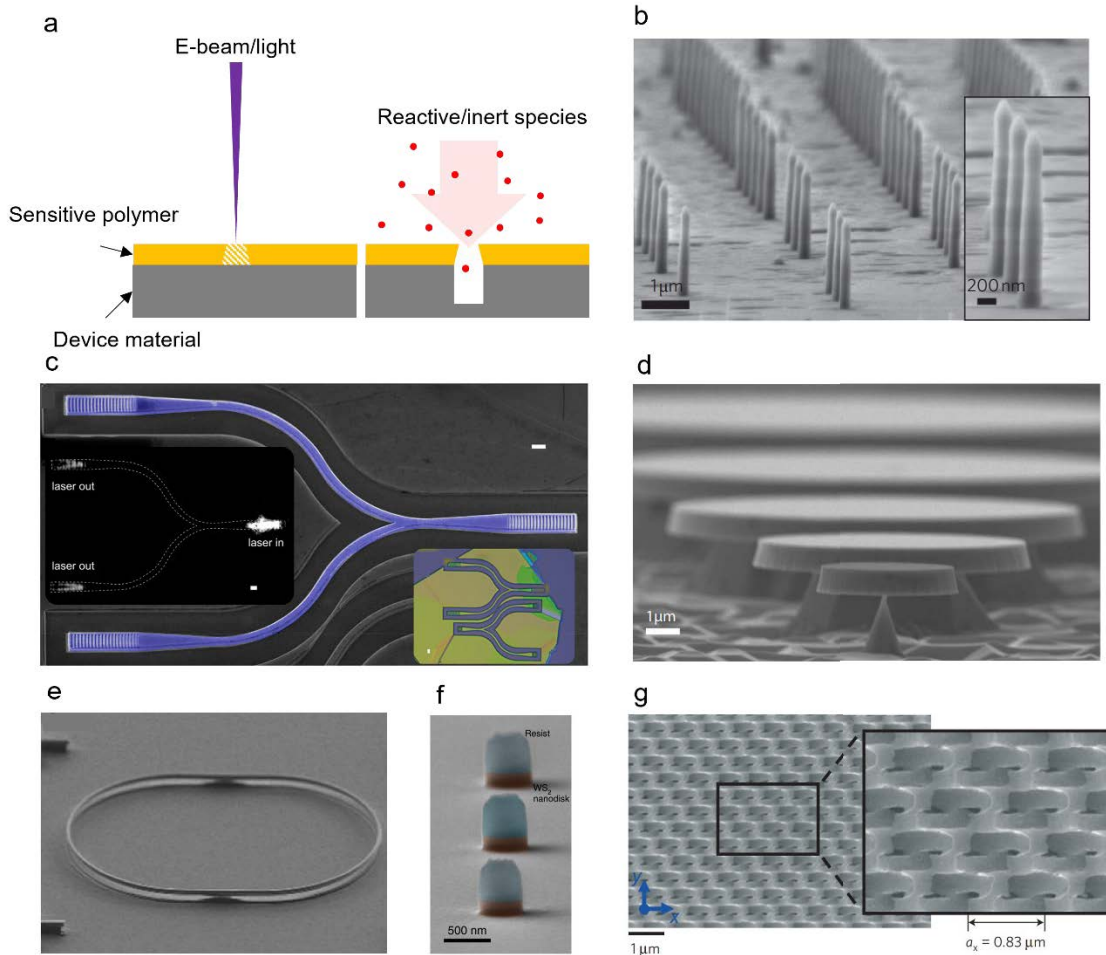
Figure 2.18. Photonic structures fabricated via top-down technique. *(a)Schematic illustration of top-down fabrication method. (b) diamond pillars with high aspect ratio containing single-photon emitter. (c) hBN beam splitter and grating couplers. (d) suspended 3C-SiC micro-disk resonator. (e) diamond racetrack resonator undercut using a faraday cap to be able to angularly etch the structure. (f) WS2 nano-disk Mie resonator etched through the polymer resist. (g) diamond 3D photonic crystal fabricated using angled ion etching method. Reproduced from [167-172]*

The first step in both fabrication schemes (bottom-up and top-down) is the definition of a mask by means of a lithography method such as electron beam lithography or photolithography method. Following the definition of the patterns, the sample is subjected to a series of steps by which the nanophotonic structure is formed by carving or growing from the predefined patterns. In this thesis EBL was carried out via a Zeiss Supra 55 VP SEM, equipped with a RAITH EBL system as shown in figure 2.19 a. A high-resolution

positive resist was used throughout this thesis. The patterning recipes, such as exposure and development parameters, were continually improved throughout the study and the exact parameters are given in the relevant sections. Nanophotonic structures are subsequently formed by either etching or growing the underlying patterned material. In this thesis, etching step was achieved through Induced Coupled Plasma Reactive Ion Etching (ICP-RIE) or Focused Ion Beam (FIB). Herein, Helios G4 PFIB UXe DualBeam microscope equipped with a different gas source was used for the ion implantation and FIB milling process (figure 2.19 b). The RIE is a gas phase dry etching process wherein reactive ion species are generated by a RF plasma (typically 13.56 MHz) at a low pressure and directed toward the sample by an applied stage biased providing highly anisotropic etching. The reactive species such as radicals interact with the sample via chemical and/or physical reactions. Chemical reactions with reactive ion species can produce volatile species and these volatile components will be removed using a turbo molecular pump. The RIE system used in this thesis was a Trion ICP plasma system (figure 2.19 c). For the bottom-up growth, microwave plasma chemical vapor deposition (MPCVD) was used to grow high quality diamond. During the synthesis of diamond, the substrate was exposed to reactive gases including methane and hydrogen and the growth was carried out via pyrolysis of carbonaceous gases including methane, carbon monoxide etc. In this thesis, we employed ASTeX AX 5010 MPCVD reactor for the synthesis of high-quality diamond (figure 2.19 d).
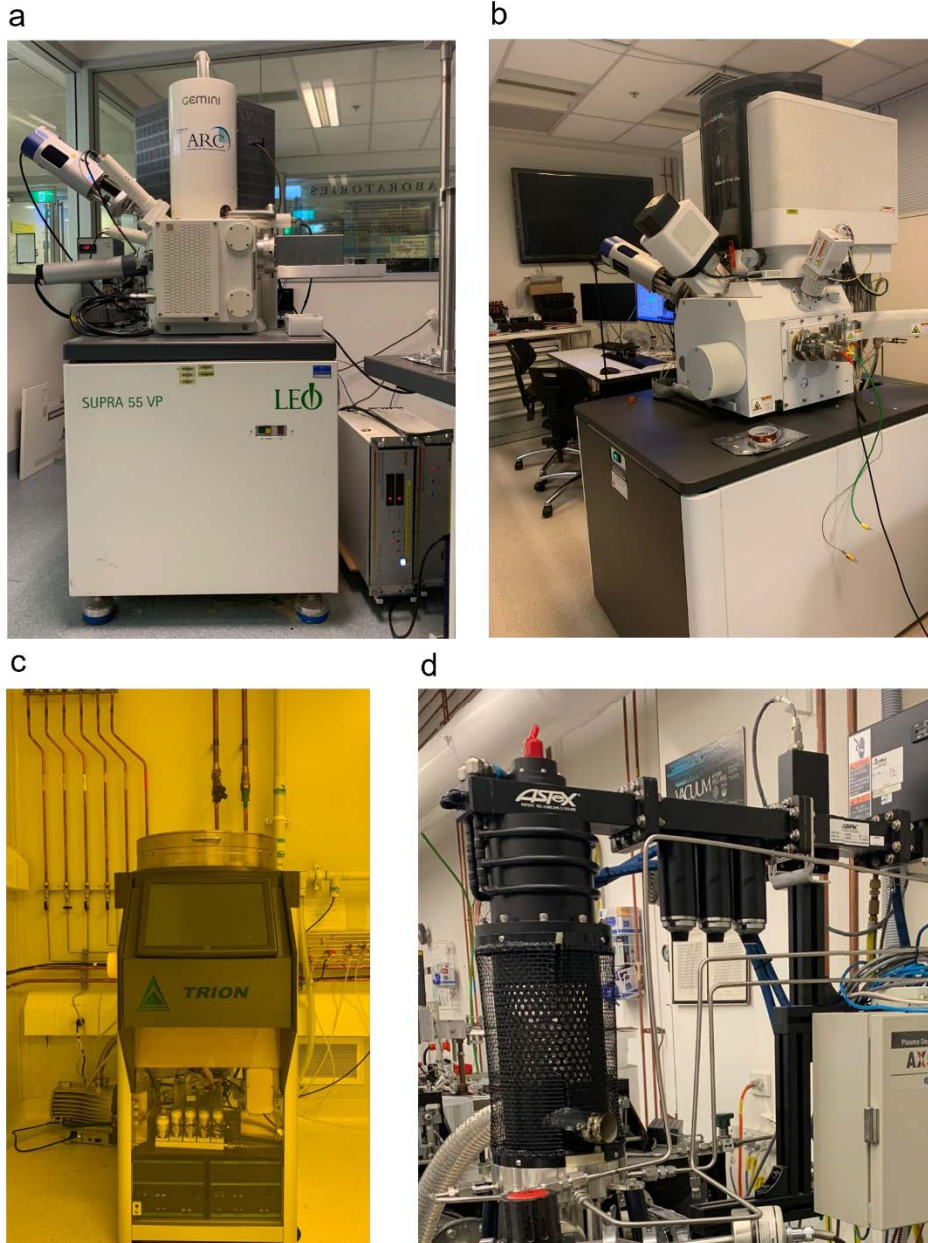
Figure 2.19. Nanofabrication facilities used in this thesis. *(a) Zeiss Supra 55 VP SEM equipped with pattering system. (b) Helios G4 PFIB UXe DualBeam microscope (c) Trion ICP-RIE plasma system (d) ASTeX AX 5010 MPCVD diamond reactor.*

Chapter 3: Bottom-Up Synthesis of Single Crystal Diamond Pyramids Containing Germanium Vacancy Centers

This chapter shows the possibility of bottom-up fabrication of single-crystal diamond photonic structure from a polycrystalline diamond substrate. We will discuss how to deterministically control growth conditions in restricted aperture in polycrystalline diamond in order to grow single-crystal photonic structures. The structures were subsequently overgrown in the presence of germanium solid precursors and to showcase the possibility of incorporating single Germanium vacancy centers, we have conducted confocal PL at room and cryogenic temperature .

3.1 Abstract

Diamond resonators containing color-centers are highly sought after for application in quantum technologies. Bottom-up approaches are promising for generation of single-crystal diamond structures with purposely introduced color centers. Here we demonstrate the possibility of using a polycrystalline diamond to grow single-crystal diamond structures by employing a pattern growth method. We first clarify the possible mechanism of growing a single-crystal structure with predefined shape and size from a polycrystalline substrate by controlling growth condition. Then, by introducing germanium impurities during the growth, we demonstrate localized and enhanced emission from fabricated pyramid shaped single-crystal diamonds containing germanium vacancy (GeV) color centers. Finally, we have measured linewidth of ~ 500 MHz at 4K from a single GeV center in the pyramid shaped diamonds. Our method is an important step toward fabrication of three-dimensional structures for integrated diamond photonics.

3.2 Introduction

Diamond color centers have been at the center of many studies on quantum science and engineering and light matter interactions [57, 69, 173-175]. To improve the optical

emission of color centers, a wide array of approaches has been developed to fabricate nanostructured resonators and cavities from diamond [170, 176-180]. These include top-down techniques using reactive ion etching (RIE), or bottom-up techniques such as chemical vapor deposition (CVD), both through a predefined pattern. While top-down techniques have been used to fabricate photonic resonators and waveguides with color centers often introduced via ion implantation, the bottom-up approach is promising for the incorporation of specific color-centers within the photonic structure during the diamond growth [95, 158, 181-183]. This feature eliminates the damage occurring during ion implantation process, which requires a recovery process to bring back the crystal quality. In addition, the bottom-up approach shows potential to be utilized in the future to facilitate the growth of three dimensional (3D) structures that are inherently challenging to fabricate using top-down techniques.

For majority of quantum photonic applications with diamond color centers, single crystal diamond is the preferred choice. The optical losses due to absorption and scattering within polycrystalline material can be avoided by using single crystal material, resulting in higher optical properties of the device. However, the lower cost of large-scale polycrystalline diamond and can be grown on various substrates, has motivated engineering of photonic structures from polycrystalline diamond [184-190]. In addition to the host crystal quality, various color centers in diamond have been proposed for application in quantum technologies. Among these, group IV color centers including the germanium vacancy (GeV), have attracted attention because of its desirable optical properties [175, 191, 192]. The emission of GeV center is consisting of a strong zero phonon line (ZPL) at 602 nm and a weak phonon side band (PSB) with larger spin and orbit splitting in both ground and excited states [69, 175, 193].

In the current work, we employ the bottom-up growth method to engineer arrays of single-crystal diamond structures from a polycrystalline substrate. Previously the overgrowth of polycrystalline parent material results in a polycrystalline diamond [194-198]. However, in this work, we show that under specific growth conditions, namely through apertures, single crystal diamond growth can be facilitated. Using this methodology, we demonstrate a patterned growth of an array of single-crystal diamond pyramids and explore their

growth mechanism. We then purposely introduce germanium vacancy (GeV) color centers and investigate the photoluminescence enhancement within the pyramid shaped diamond. Finally, we study the optical emission of incorporate GeV centers at cryogenic temperatures and demonstrate the emission linewidth of approximately 500 MHz from these centers.

3.3. Methods

Fabrication of pyramids. Figure 3.1 shows the schematics of the fabrication process of the single-crystal diamond pyramids. The fabrication process starts with a commercially available polycrystalline diamond (Element 6 Co.) as shown in figure 3.1 a. The wafer was first cleaned in boiling piranha solution (3:1 sulfuric acid: hydrogen peroxide) followed by 10 minutes UV-ozone exposure to remove surface contaminations. A thin film of 300 nm Silicon was deposited on the polycrystalline diamond wafer to act as a hard mask by means of RF magnetron sputtering in an Argon environment (figure 3.1 b). A dilution of positive electron resist CSAR 62 (AllResist CO.) with 9% solid content in Anisole, was then spin-coated on top of Silicon mask to form resist layer. Arrays of 1 um square were then patterned using a FEG-SEM (Zeiss Supra 55 VP) equipped with a RAITH electron beam writing system (figure 3.1 c). The parameters used for patterning were 40 pA at 20 kV and dosage of ~ 100 μCcm^{-2}. AR 600-546 (AllResist Co.) was used to develop the resist for ~20 s at room temperature to form the etch mask. The sample was then placed in an inductively coupled plasma (ICP) reactive-ion etching (RIE) system and etched for 1 min with 30 sccm of SF_6 gas, 150 W bias power at a chamber pressure of 10 mTorr in order to transfer patterns into Silicon hard mask (figure 3.1 d). To grow diamond through bottom-up approach, the polycrystalline diamond wafer with the restricted circular apertures (1 μm) (figure 3.1 d) is introduced to a microwave plasma chemical vapor deposition (MPCVD) chamber (figure 3.1 e) under the following conditions: microwave plasma 900W, pressure 60 Torr, 1% methane concentration with the temperature of ~ 900 °C. After the growth process, the silicon hard mask is removed from the diamond's surface by dissolving in a KOH solution (20 wt. %) at 70 C for 3 hours (figure 3.1 f). The growth was performed in the presence of 100 μL of 1 wt. % aqueous solution of GeO_2 drop-casted on a sapphire wafer placed next to the samples on the carbon puck.
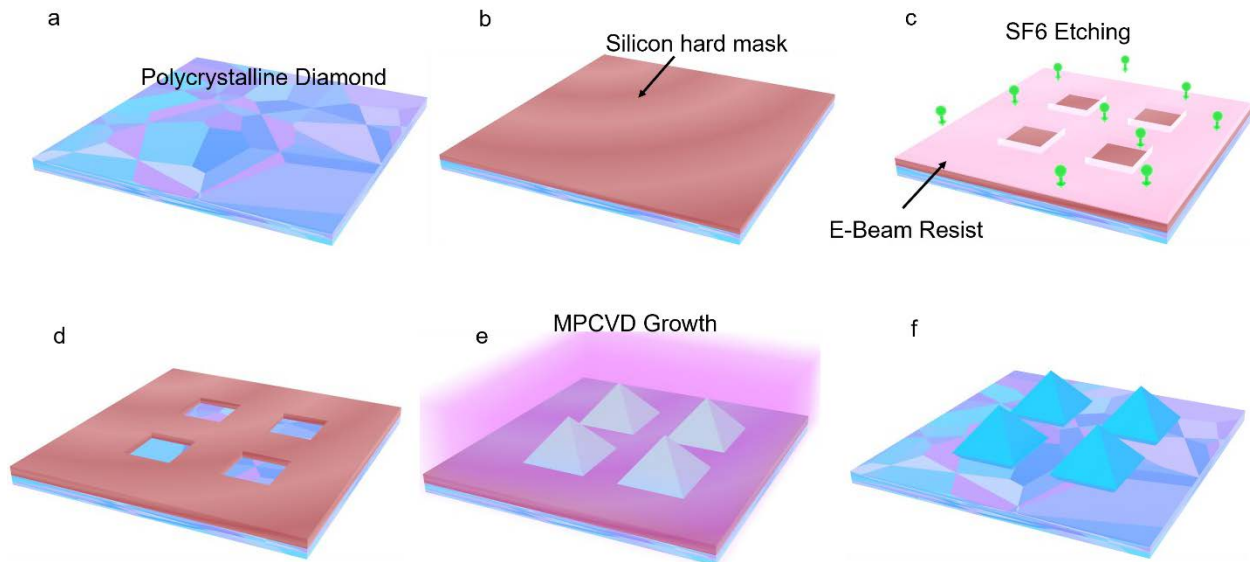
Figure 3.1. *Schematic representation of the single-crystal diamond pyramids fabrication process.* *(a) commercial polycrystalline diamond substrate, (b) deposition of silicon hard mask via magnetron sputtering, (c) transferring the patterns created by EBL onto the silicon hard mask using SF6 ions (green ions) within ICP-RIE, (d) the silicon hard mask with apertures on top of polycrystalline diamond, (e) MPCVD overgrowth of the diamond through the apertures (f) Silicon hard mask removal using KOH solution.*

Room temperature PL measurement. Room-temperature photonic characterizations were performed using a lab-built confocal system. In the system, a 532 nm CW laser (Gem 532TM, Laser Quantum Ltd.) was used for the excitation. The laser was then focused onto the sample by a 100x objective with 0.9 numerical aperture. Hence, a beam spot around 500nm was estimated in this experiment. Green dichroic mirror and a 568-nm long pass filter were placed before the signal went into the spectrometer (Princeton Instruments, Inc.). We use a flip mirror to guide the same signal to a single mode fiber and then split it into two avalanche photodiodes (APDs) by a 50/50 fiber splitter. The PL mapping was realized by a scanning mirror and the intensity, namely photon counts, is adopted from one of the two APDs. During all the PL measurements, laser power before the objective was fixed to 200 μW.

Cryogenic temperature PL measurement. For cryogenic PL studies, sample was loaded on a closed loop helium cryostat (Attocube 800) and cooled down to 4K. A tunable dye laser (Spectra physics Mattisse) with bandwidth of less than 100 KHz at 50nW was scanned around the ZPL emission of GeV. Using a long pass filter (Semrock-610nm long

pass filter) emission into photon side bad was collected during resonant excitation. For on resonant autocorrelation measurement the laser was tuned onto the emission energy of GeV and the emission from PSB was split into two collections in an HBT configuration. Using a time tagging device (Swabian time tagger 20) autocorrelation was measured using APDs.

EBSD Crystallography. EBSD studies were conducted using SEM microscope (Thermo Fisher Scientific Helios G4) with the acceleration voltage of 20 kV and acquisition speed of 39.5 Hz. The angel of incident between the primary electron beam and the specimen surface normal was set to 70°.

FDTD Simulations. Finite-difference time-domain simulation was conducted using commercial software (Lumerical Inc). The 3D pyramid diamond structure on planar diamond substrate having refractive index of 2.4 was implemented in the simulation. A pyramid used in numerical modelling was a quadrangular pyramid with a base square (1.5 μm ×1.5 μm) and its height (950 nm) drops directly to center of the base. The planar wave was injected from top toward the bottom and the intensity enhancement was observed. To acquire intensity enhancement, two simulations, with and without a pyramid, were conducted under the same excitation condition.

3.4. Result and discussion

The electron backscattered diffraction (EBSD) pattern of the as-received polycrystalline diamond substrate (before growth) is shown in figure 3.2 a. The results indicate the large distribution of crystal grain sizes with various crystal orientations which is also confirmed by the Kikuchi pattern (figure 3.2 b). As a reference, we performed identical growth without patterning the substrate, which results in a polycrystalline diamond with similar grain size distribution compared to the ones before growth (figure 3.2 c). In contrast, introducing the pattern structure during the same growth condition resulted in growing single crystal, pyramid shaped, diamond structures as shown in figure 3.2 d and 3.2 e. The arrays of single-crystal diamond pyramid with a homogenous distribution and aligned crystal facets can be generated from a polycrystalline wafer underneath as directly visible from a polycrystalline background (figure 3.2 d). Raman shift from the single-crystal diamond

pyramid is reported in figure 3.2 f. The first order diamond Raman shift (sharp peak at 1333 cm^{-1}) shows the high quality of the overgrown diamond pyramids.
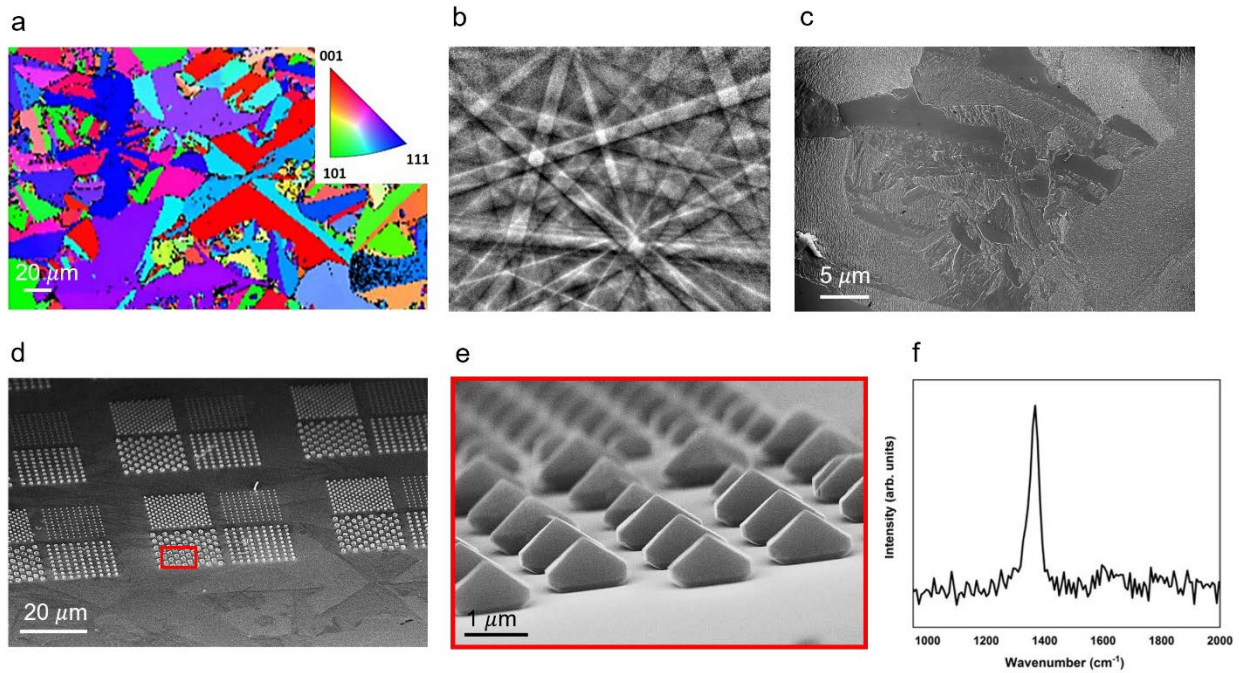
Figure 3.2. Characterization of single-crystal diamond pyramid. *(a) EBSD signals recorded from polycrystalline diamond wafer (before growth). (b) Kikuchi pattern of the sample shown in (a). (c) SEM image of MPCVD overgrowth of diamond substrate without using any hard mask. (d) SEM images of the overgrown polycrystalline diamond through apertures which resulted in the growth of single-crystal pyramid shaped diamond (e) Higher magnification SEM image of the highlighted area in (d) depicting single-crystal pyramid arrays with uniform size and orientation. (f) Raman peak recorded from a single-crystal pyramid using 532nm laser excitation.*

We now turn our attention to the pyramid shape structures after the growth. The formation of diamond crystals during MPCVD is governed by the original substrate and growth condition defined as α-parameter. This parameter is determined by the ratio of growth rate (V) along <100> and <111> planes ($\alpha = \sqrt{3} V_{100}/V_{111}$) which can be controlled by the growth condition (mainly temperature and methane concentration) [199, 200]. Therefore, for $\alpha = 1$, a cubic diamond made of <100> crystal facets will form, while for $\alpha > 3$, an octahedron with <111> facets will dominate the growth. In the condition of $1 < \alpha < 3$, a combination of the two shapes is expected. For example, a cube-octahedron will be

produced if α-parameter is set to 1.5 [201]. For the purpose of discussion of the growth mechanisms, the growth conditions remain the same through of this work.
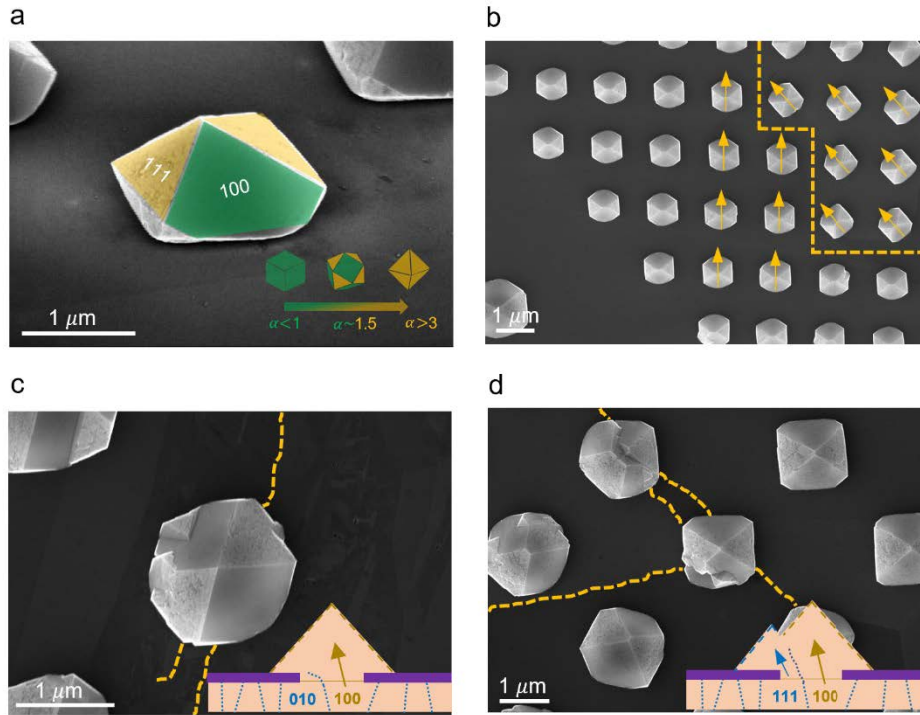
Figure 3.3. Growth mechanism of pyramid-shaped diamonds. *(a) False color SEM image of the crystal facets of an overgrown single-crystal diamond through the apertures. Inset, schematic illustration of variation in the final crystal shape depending on growth condition defined by α-parameter. (b) SEM image of pyramid arrays overgrown on two different crystal grains (yellow arrows indicate the orientations of pyramids and dash line separate two sections of arrays with different orientations). (c) SEM image of a single crystalline pyramid-shaped diamond overgrown over polycrystalline substrate. Inset, mechanism of competition growth of polycrystalline diamond resulting in a pyramid-shaped single crystal diamond. (d) SEM image of imperfect pyramid-shaped diamond (the middle pyramid) from overgrowth of a polycrystalline substrate. Inset, mechanism of competition growth that leads to imperfect pyramid-shaped diamond.*

Figure 3.3 a shows a halved cubo-octahedral diamond resulting from the overgrowth of a polycrystalline diamond through an aperture of 1 μm. Note that in this case, the lateral growth was limited by applying a hard mask on polycrystalline diamond during the growth. A false color image has been used to highlight the different crystal facets (111 and 100) of a cubo-octahedral diamond which coincide with α-parameter of ~1.5 (Figure 3.3 a. Inset). Moreover, we observed that an array of pyramid-shaped single crystal diamonds is always aligned if grown within the same grain. As the propagation of similar planes is

expected to happen with similar growth velocity, the uniform orientation of diamond pyramids within a single grain diamond is expected. As a result, the growth of single crystal arrays will follow the orientation the diamond grain underneath within the polycrystalline diamond as shown in figure 3.3 b.

Interestingly, a pyramid shaped diamond is formed in all the cases (i.e., regardless of the underlying crystal grain). These pyramid shaped diamonds are mostly perfect single crystals (as shown in figure 3.3 a). Although, pyramid shape can also be achieved by promoting 111 growth ($\alpha > 3$ – shown in Figure 2 a-Inset), this requires high methane concentration and lower temperature which results in non-diamond phase, more crystal defects and in turn low quality diamond. Therefore, to facilitate diamond growth with less twinning and dislocations, conditions of $\alpha \sim 1.5$ are preferred. In this case, <100> planes grow faster and a pyramid like diamond shape is anticipated. In our growth method, the presence of an aperture will terminate the slowly growing crystal and only the fastest growing grain orientation (<100> in the schematic) will be promoted. This growth is analogous to growing bottom-up diamond crystals from a single crystal diamond. The final structure in this case will be a single-crystal diamond pyramid, with two <100> and two <111> planes. In addition, in the event that an aperture covers a grain boundary (indicated by yellow dash line in figure 3.3 c), a secondary nucleation can occur. As a result, a defective pyramid structure will be formed, as shown in figure 3.3 c. In this case, in the competition between various crystal grains, the two fastest ones make their way out while the rest terminate by the aperture. The two single-crystal diamonds further merge and form an imperfect pyramid shaped diamond structure. This is analogous to the large area diamond mosaic growth that was recently developed [202, 203]. The illustration of the growth mechanism is shown in the inset of figure 3.3 c.

On the other hand, several grains can also start to grow simultaneously if the aperture is located at a grain boundary, as shown schematically in figure 3.3 d Inset. In this case the pyramid shape diamond is more defective. During the overgrowth, some planes will merge with the fastest growing plane, but the rest induce a secondary crystal that would resemble a secondary nucleation or defect in the pyramid. An example of such growth is shown in the SEM image of figure 3.3 d. Note, that even under these conditions, the final pyramid is still a single crystal diamond, with minor defects on its side. Due to large

distribution of crystal grain size, we have statistically measured the number of imperfections from different area of the substrate. In an area of 50x50 μm, out of 60 pyramids, on average 6 of them (~ 10%) are affected by crystal boundaries resulting in imperfect pyramid shape as shown in figure 3.4.

a   b   c
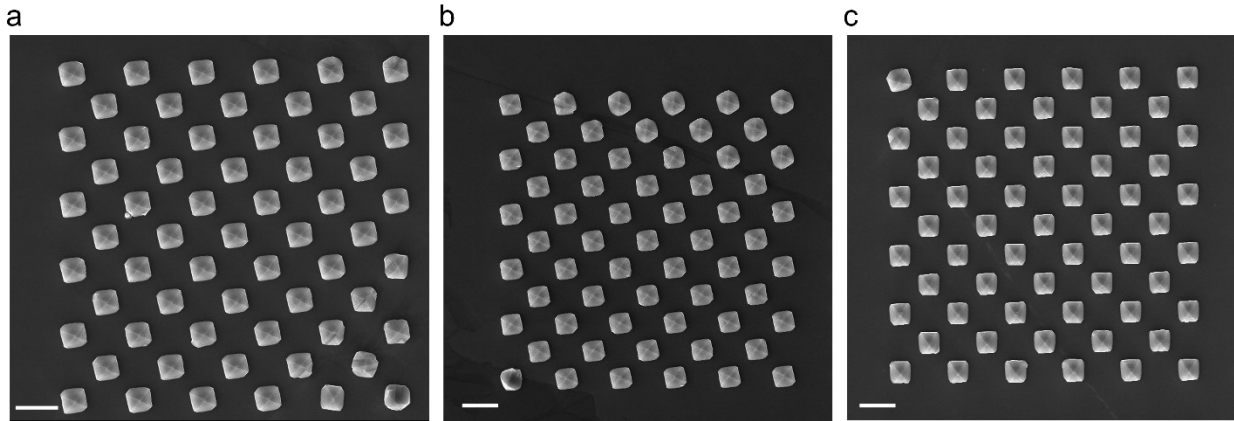
Figure 3.4. (a to c) top view SEM images of the single-crystal diamond pyramid arrays showing small fraction of the imperfections. Scale bars corresponds to 1 μm.

To show the utility of the grown pyramids, and the advantages of the bottom-up technique, we demonstrate an incorporation of the GeV color centers. We follow the procedure developed previously [204], and the GeV was introduced during the overgrowth using the same growth condition as mentioned in the Method section. A patterned diamond and an un-patterned diamond were overgrown at the same time, the latter was used as reference sample for comparison.
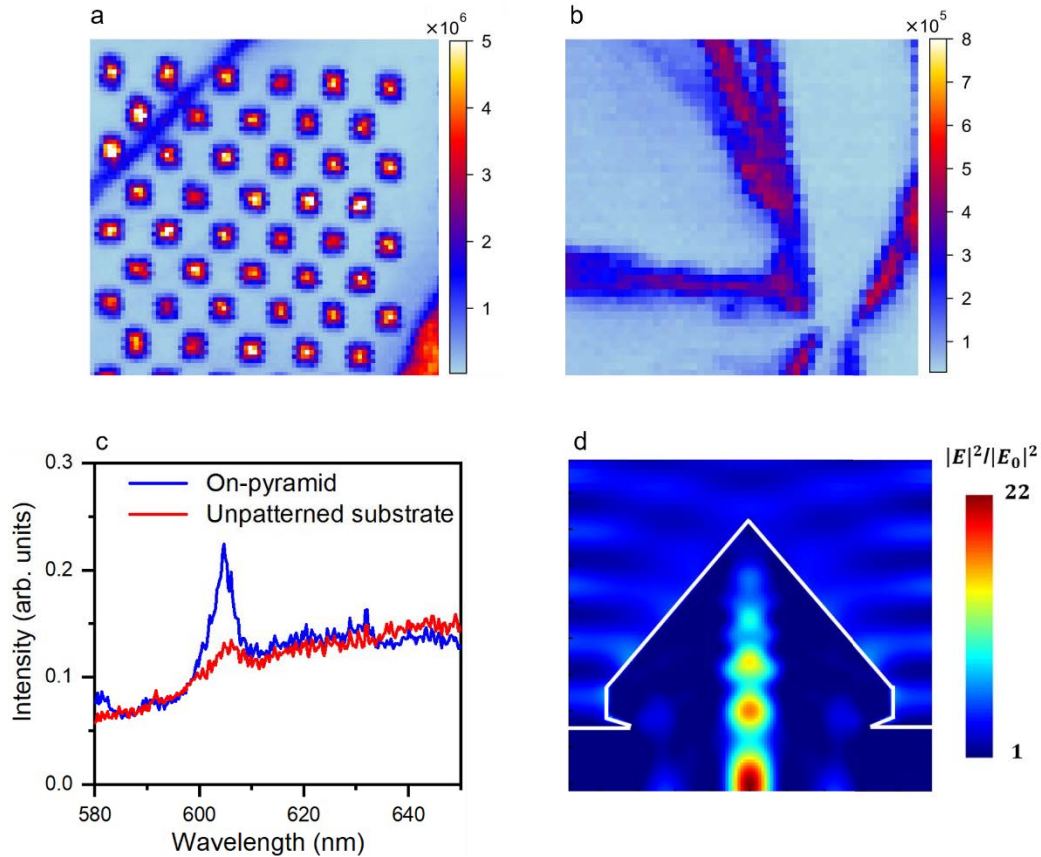
Figure 3.5. Incorporation of GeV centers during the growth. *Confocal map of (a) arrays of pyramid-shaped diamond and (b) overgrown polycrystalline unpatterned substrate. The emission at 600 ± 15nm was only collected during the PL map. Both samples were overgrown for 15 minutes simultaneously. (c) Representative PL spectra of GeV obtained from a pyramid (blue) and overgrown polycrystalline unpatterned substrate (red). PL spectra are normalized to SiV peak (d) Electric field intensity at pyramid cross-section when incident light wavelength is 600 nm.*

Figure 3.5 a and 3.5 b show a 2D confocal map of the array of diamond pyramids and an unpatterned overgrown sample, respectively. A green laser (532 nm) was used as an excitation source and the emission is collected through a bandpass filter of 600 ± 15nm to selectively map the emission from GeV centers (zero phonon line at ~ 602 nm). The background emission in overgrown diamond was dominated by the presence of NV and SiV centers incorporated during the growth. By accurate control of the growth condition, one would be able to avoid incorporation of unwanted defects and eliminate the background emission. The GeV showed enhance emission within the pyramid diamond compared to the one embedded in the unpatterned sample. Figure 3.5 c compares the

PL spectra collected from a pyramid and an unpatterned diamond. On average we observed approximately 3 times higher intensity of GeV in pyramids compared to the unpatterned samples. Additional data is plotted in the figure 3.6. Note that, different GeV emission intensity might be affected by the variation in incorporation and the location of GeV centers inside the diamond as well as optical loss from imperfect shape pyramid. We noticed the GeV ZPL in the pyramids shifted by 7 meV Which might be related to the residual stress in the pyramid after the growth.
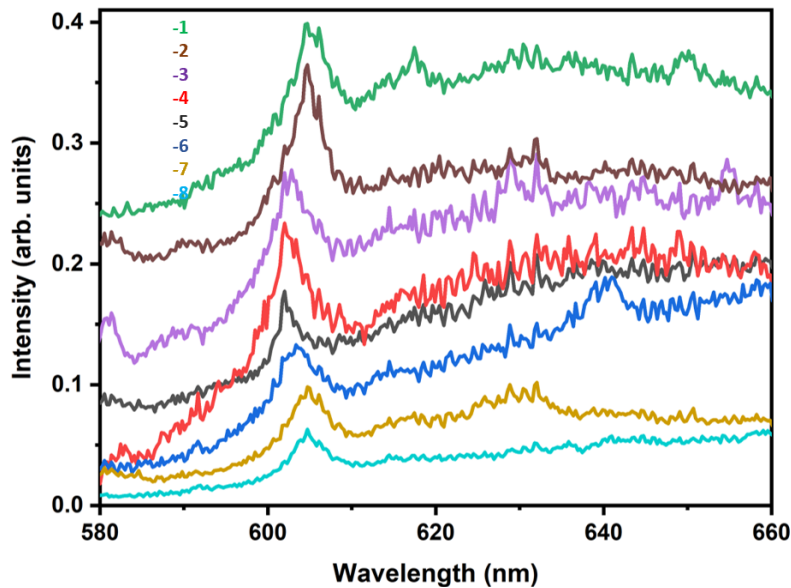
Figure 3.6. *Photoluminescence spectra collected from random pyramids.*

To support our enhancement results, we perform finite-difference time-domain (FDTD) calculation. The pyramid shape enables light confinement for both the excitation laser and the emitter. Figure 3.5 d shows the electric field intensity distribution of incident light in the pyramid for λ=600 nm. The pyramid shape enhances the excitation light by a factor of 22 at maximum.

Finally, we investigate the cryogenic PL properties of incorporated GeV centers in the pyramid shaped diamonds. The typical molecular structure of the germanium divacancy with an inversion symmetry is shown in figure 3.7 a. Like all other group IV impurities in

diamond [69], germanium atom occupies an interstitial position with two vacancies along with <111> direction in diamond crystal lattice. Figure 3.7 b shows energy level structure of the defect (GeV) with a spin doublet (S = ½) in ground state. Both ground and excited state can be split by spin-orbit coupling resulting in double orbital degeneracy as shown in figure 3.7 b. The four transitions were observed in our experiments at cryogenic temperature (4K) with a main transition ~603 (figure 3.7 c) under off resonant excitation. The four peaks confirm the optical transition predicted by germanium vacancy energy level structure as indicated by A, B, C and D.
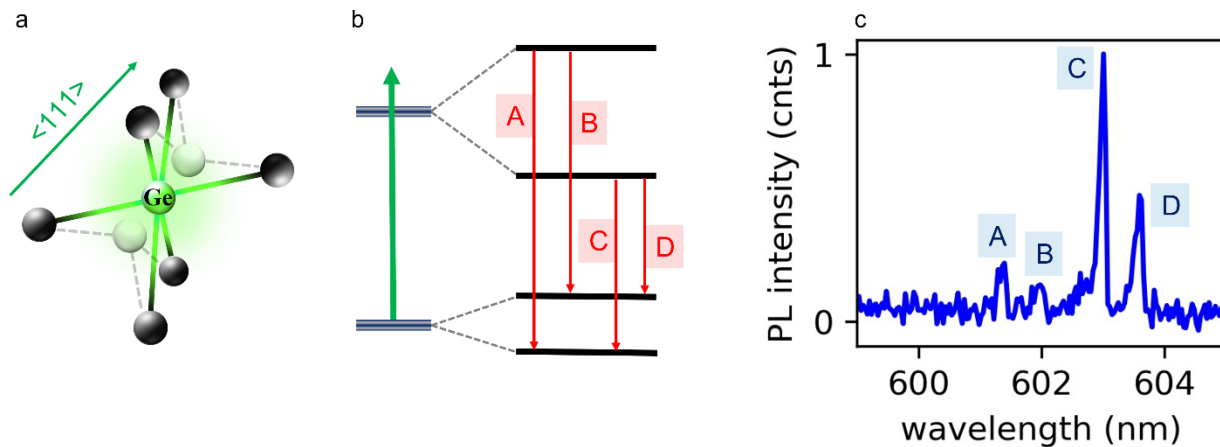
Figure 3.7. Cryogenic spectroscopy measurement of GeV centers. *(a) germanium vacancy molecular structure aligned with the 111-crystal orientation (b) energy level structure of the germanium vacancy defect shown in (a). (c) normalized PL spectrum of the GeV defect at cryogenic temperature (4K) from the pyramid shaped diamond. A-D shows the corresponding transition as discussed in (b)*

To study coherent properties of the single GeV center, we used a narrow band dye laser to drive the transition highlighted as C in figure 3.7 c. The transition (denoted as "C") was scanned with the frequency of the laser and the resonant PL of the GeV emitter was collected using the phonon side band and is shown in figure 3.8 a. A linewidth of around 500 MHz obtained with Gaussian fit to the data. The emission linewidth is broader compared to the reported values for a single GeV center, and the Gaussian fit indicates the inhomogeneous broadening of GeV in the CVD grown samples. To prove the same line is attributed to a single defect, we recorded the second order autocorrelation function, while exciting the center resonantly. Figure 3.8 b shows the antibunching of the ZPL

photons and fitted data (solid line) confirming single-photon nature of these defects ($g^2(\tau)$ < 0.5).
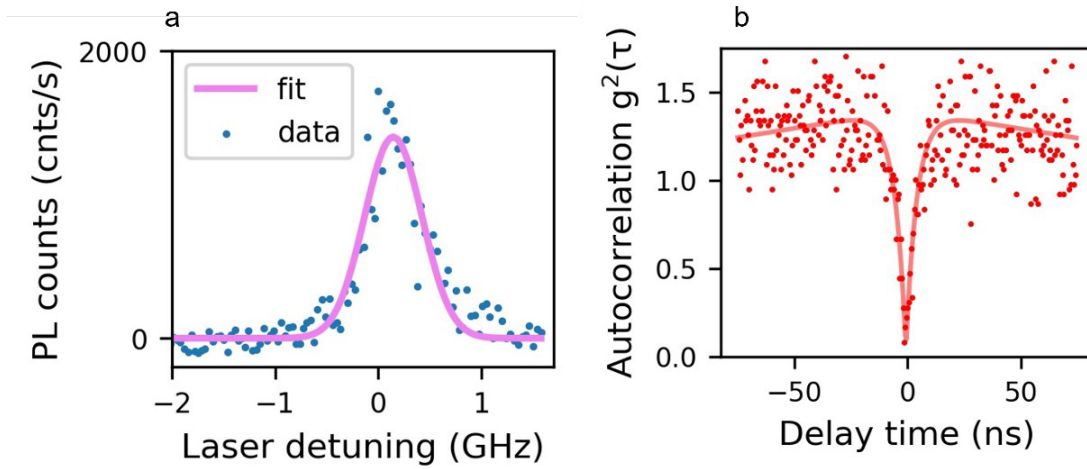
Figure 3.8. Resonant excitation of the main transition in the GeV center. *(a) Resonant photoluminescence excitation of the transition. The solid line is a Gaussian fit with FHWM of 500 MHz. (b) Autocorrelation measurement of resonantly driven GeV under 50 nW laser power.*

3.5. Conclusion

In summary, we demonstrated bottom-up engineering of single crystal diamond pyramids from a polycrystalline diamond material. We have discussed the mechanism for such growth using restricting apertures and demonstrated controlled incorporation and enhancement of the GeV color centers in these structures. Furthermore, we have measured the photoluminescence emission of incorporated GeV centers at cryogenic temperature and identified narrowband emitters with ~ 500 MHz linewidths. Our results highlight the potential use of polycrystalline materials for selected applications. For instance, where only emission enhancement is needed, employing polycrystalline material with an overgrowth is a cost-effective method to achieve the goal. Overall, our results are a promising avenue for generation of photonic structures for diamond photonics.

Chapter 4: Coupling Spin Defect in Hexagonal Boron Nitride to Titanium Dioxide Ring Resonators

This chapter presents the fabrication of suspended ring resonator and the integration of spin defect in a thin hexagonal boron nitride flake to the whispering gallery modes of the resonator. The main goal of this project was to improve a method for the hybrid integration of spin defect into a high-Q cavity. The coupling of the spin defect into the ring resonator was confirmed by ODMR via non-local excitation scheme.

4.1. Abstract

Spin-dependent optical transitions are attractive for a plethora of applications in quantum technologies. Here we report on utilization of high-quality ring resonators fabricated from TiO_2 to enhance the emission from negatively charged boron vacancies (V_B^-) in hexagonal Boron Nitride. We show that the emission from these defects can efficiently couple into the whispering gallery modes of the ring resonators. Optically coupled V_B^- showed photoluminescence contrast in optically detected magnetic resonance signals from the hybrid coupled devices. Our results demonstrate a practical method for integration of spin defects in 2D materials with dielectric resonators which is a promising platform for quantum technologies.

4.2. Introduction

Defects in hexagonal boron nitride (hBN) provide a test bed for the study of light-matter interactions and nanophotonics with two-dimensional materials at room temperature.[74, 139, 205-207] Among them, optically addressable spin defects have recently gained momentum due to their relevant application in quantum sensing and quantum information technologies. [55, 57, 77, 208, 209] Particularly, negatively charged boron vacancies (V_B^-) is a spin 1 system which can be mapped out through optically detected magnetic

resonance (ODMR) spectroscopy at room temperature [210-214]. At zero field, the transitions between two spin states ($m_s = 0$ and $m_s = \pm 1$) in the ground state result in two resonances at ~3.4 and ~3.5 GHz in the ODMR signal [210]. Spin coherence of V_B^- has been exploited for high temporal and spatial resolution quantum sensing of temperature, strain, electric and magnetic fields. [215-219] However, the photoluminescence emission from V_B^- spans in the NIR has no clear indication of zero phonon line (ZPL) even at cryogenic temperature, and the exact electronic level structure and emission dipole of V_B^- are yet to be understood. Just recently, coupling of the defects into high-quality cavities suggests the ZPL spectral location to be around 770 nm [220] and excited state spectroscopy of the defects revealed the spin states in the excited state. [221-223] Moreover, the defect suffers from low intrinsic brightness and quantum efficiency. This limitation can be overcome by coupling the V_B^- to micro-resonators that enables efficient control over the emission properties as such presents an attractive platform for enhanced understanding and utilization of spin defects in van der Waals materials. Recent attempts have been made to couple V_B^- into bullseye [101] or plasmonic [224] structures which results in the enhancement of the emission. Dielectric resonators such as ring resonators supporting whispering gallery modes (WGMs), provide high-quality factors in low mode volume structures and hence are attractive alternatives.[114, 225-227]

Here we realize a hybrid approach based on hBN flake as V_B^--hosting material on top of TiO_2 as a cavity platform. Since a high-quality cavity requires relatively large refractive index of ~2.5 and low optical loss in the wide wavelength range in the visible and IR, TiO_2 is an attractive material for the fabrication of waveguides and photonic resonators [110, 228-230]. The resonator is designed to support multimode WGMs with small free spectral range (FSR) in an attempt to enhance the broad emission of V_B^-. Finally, the ODMR collected from the ring confirms the efficient coupling of spin defects in hBN into WGM modes of the TiO_2 ring resonator.

4.3. Fabrication of suspended ring resonator

We developed a fabrication process to realize hBN/TiO$_2$ hybrid resonator and to demonstrate emission enhancement of spin defect by coupling to the WGMs. The fabrication steps are schematically demonstrated in figure 4.1a c. Given the layered nature, hBN could be readily integrated with other systems by the stacking strategy [231]. However, transferring hBN on cavity structures inevitably damages these fragile structures. Thus, to avoid this, a heterostructure consisting of hBN (defect-hosting material) and TiO$_2$ (cavity material) was prepared prior to the fabrication process (figure 4.1 a).
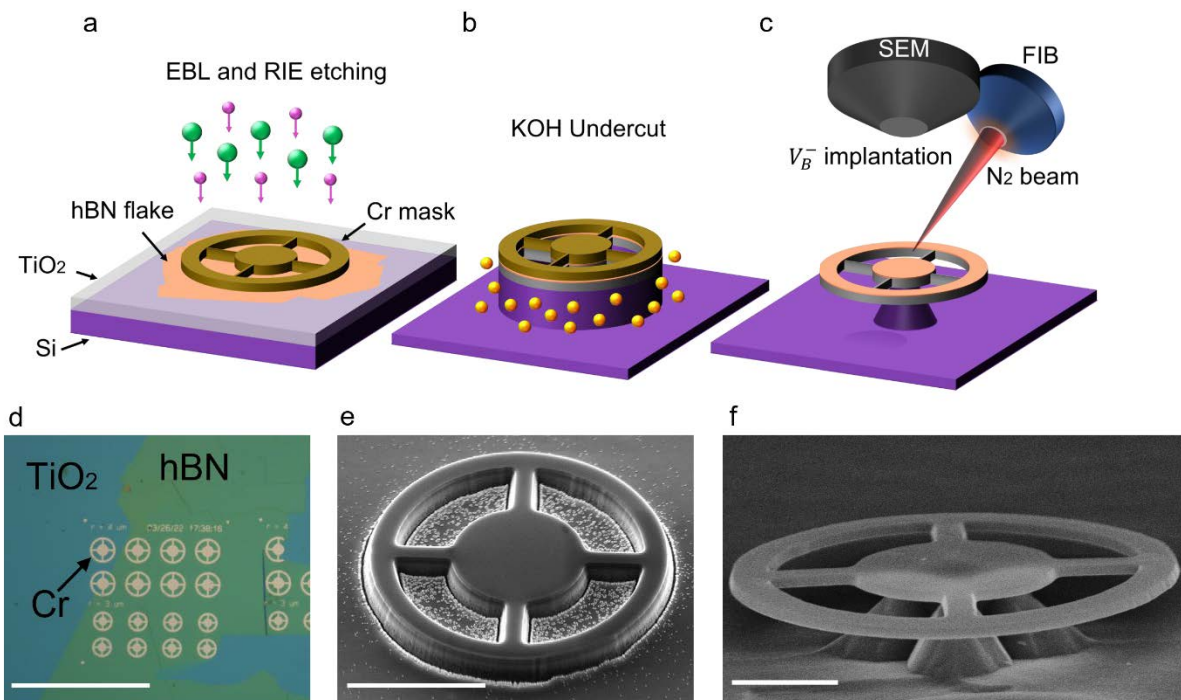
Figure 4.1. Schematic representation of the fabrication process. *(a) Lithography step to pattern a Cr metal mask (Brown steering-wheels) on hBN/TiO$_2$ heterostructure followed by transferring the mask into the heterostructure using ICP/RIE. Green and pink balls represent SF6, and Hydrogen species used in the latter step, respectively. (b) Undercut step of hBN/TiO$_2$ hybrid resonator using 10% KOH aqueous solution. (c) Generation of spin defects in hBN using angled Nitrogen focused ion beam (FIB). (d) optical image of the lithography step. Scale bar is 50 µm (e) SEM image of the hybrid structure prior to undercut step. Scale bar: 4 µm (f) tilted SEM image of the final structure. The scale bar is 2 µm.*

Firstly, A 200-nm of TiO$_2$ film as the cavity material was sputtered onto a silicon wafer through ion-assisted deposition (IAD) technique. Since the cavity platform requires high

refractive index and smooth surface, we first characterized the sputtered TiO_2 material. The Ion-assisted deposition (IAD) film morphology and optical properties were characterized by atomic force microscope and ellipsometer, respectively. As shown in figure 4.2 a, the derived mean surface variation, less than 4 nm and an RMS roughness of 0.9 nm, fall well below the wavelength of light we investigated in this work. Additionally, the TiO_2 film produced from IAD method exhibits a high refractive index of 2.3-2.5 in the visible to near infrared range (figure 4.2 b) resulting in high refractive index contrast. To minimize optical loss and improve light confinement in a high-quality cavity, it is necessary to have a high refractive index contrast and a smooth surface.
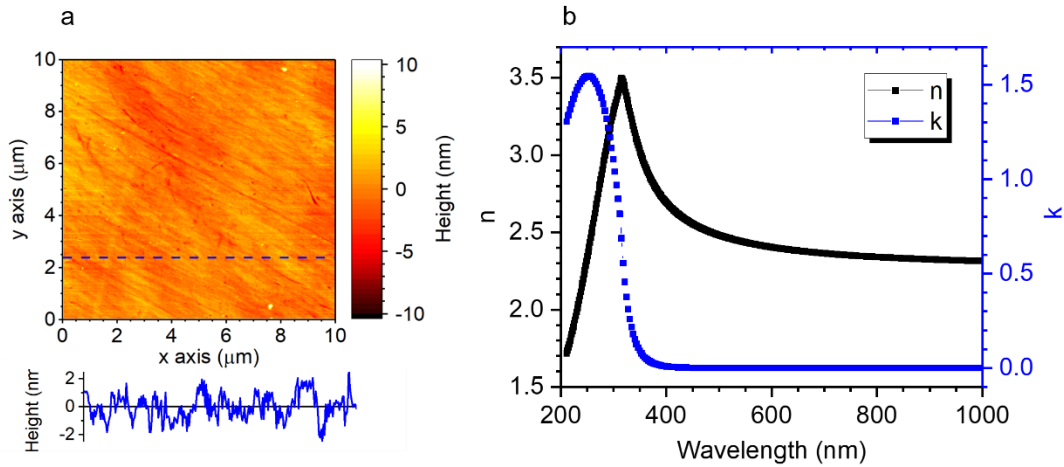
Figure 4.2. Characterization of deposited TiO_2 film. *(a) AFM tomography image of the deposited TiO_2 with the mean roughness of 0.9 nm. (b) Ellipsometry analysis of the deposited TiO_2 showing refractive index of 2.3-2.5 in the visible to NIR range.*

Afterwards, hBN flakes were mechanically transferred from high quality bulk crystal onto the TiO_2 surface via scotch tape method (figure 4.1 a and d). The sample was then annealed at 300 °C to remove the tape residual and to maximize surface adhesion to form a stable heterostructure. At this temperature, TiO_2 phase transition and the associated change in the refractive index can be avoided to retain the low optical loss of the TiO_2 [232]. Since the cavity integration requires minimum spatial distance between emitter and the cavity modes, to increase accessibility of the defect to the cavity, a thin flake (~ 20

nm) was picked for the subsequent fabrication process. The thin flake was first identified by optical contrast and further confirmed by AFM (figure 4.3).
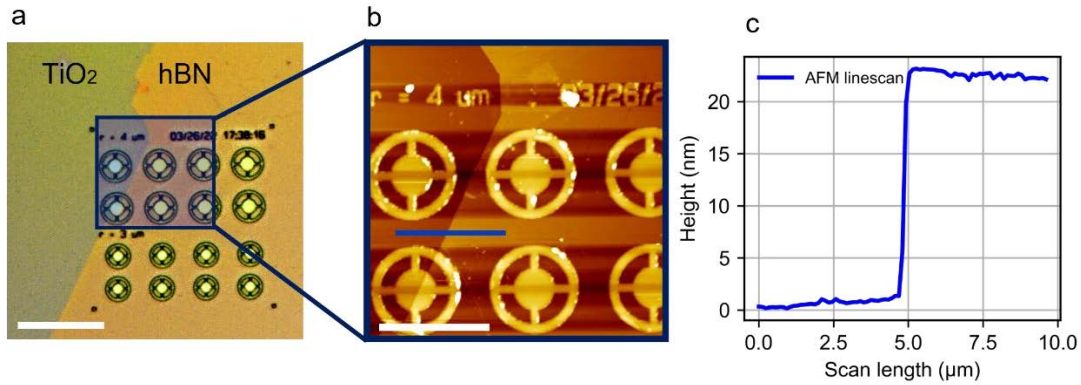
Figure 4.3. Characterization of the patterned thin hBN flake. *(a) Optical image of aligned EBL pattern on the hBN/TiO₂ heterostructure. Scale bar: 25 µm. (b) AFM image of the patterned area after Cr deposition. scale bar: 10 µm. (c) AFM profile of the scanned area indicated by the blue line in (b).*

Figure 4.3-a shows an optical microscope image of the patterned sample (as schematically depicted in figure 4.1 a) prior to etching steps. The spatially precise lithography on the flake is directly visible by optical contrast showing boundaries between hBN flake and the TiO₂ substrate. An Atomic Force Microscopy (AFM) image was scanned over the patterned area to confirm the thickness of patterned hBN as shown in figure 4.3 b and c. By picking a thin flake, the defect could be spatially closer to the cavity resulting in improved coupling efficiency since it minimizes optical loss in the hBN material. After the preparation of heterostructure, a thin layer of e-beam polymer resist (CSAR, AllResist GmBH) was spin-coated onto the sample for 60s at 5000 rpm followed by baking on a hotplate at 170 °C for 2 minutes. An array of wheel-like structures was subsequently patterned on the heterostructure using EBL technique. EBL was performed in SEM (Zeiss Supra 55 VP) with electron energy of 30 KeV, 20 pA current and a base dose of 100 µC/cm2. After the development step, 50 nm Cr was deposited on the substrate using a magnetron sputtering machine. Afterwards, the residual polymer was removed in hot CSAR remover (AR600-71, AllResist GmBH) and the remaining Cr (brown

wheel-like structure) was acting as a hard mask for the following step. The patterns were transferred from the metal mask into the underlying hBN/TiO$_2$/Si sample using ICP/RIE technique (figure 4.1 a). In order to reach the silicon substrate, the sample was continually etched for 15 minutes with gas ration of 1:7 for SF$_6$:H$_2$ and 100W bias power at a chamber pressure of 5 mTorr. Figure 4.1 e shows the SEM image of the device after the dry etching step and before undercut. Vertical and smooth etching profile can be directly observed from the sidewall morphology of the fabricated device. For the undercut step, the sample was immersed into a 10% potassium hydroxide (KOH) aqueous solution for continually 5 minutes and then placed into a beaker of DI water to stop basic reactions. During the undercut step, KOH solution can selectively etch underlying silicon resulting in suspended structure as shown in figure 4.1 f. Figure 4.4. shows an array of suspended ring resonators supported by the remaining Silicon substrate underneath the center of structure. The central disk acting as a post is directly visible from the image contrast and indicated by a yellow arrow as an aid to the eye.
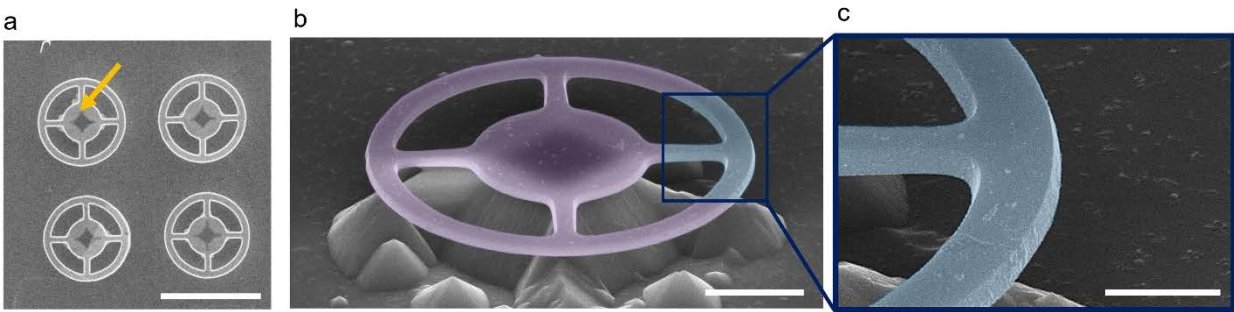
Figure 4.4. SEM image of the post-fabricated suspended ring resonator. *(a) top view of the arrays of suspended ring resonator. Scale bar is 10 µm. (b) 52° tilted SEM image of the suspended hybrid resonator after 5 minutes undercut. the scale bar is 2µm (c) magnified image of the sidewall of ring resonator. the scale bar is 1 µm.*

After the undercut step, the Cr metal mask was stripped away using Cr etchant. The sample was then rinsed with IPA and water followed by annealing at 300 °C to clean the etchant and increase adhesion. As shown in figure 4.4 b and c, one can see that the structures are unaffected by the basic solvent during the undercut step. Moreover, the vertical sidewall shows perfect anisotropic RIE etching, which is very important for any device fabrication, because this minimizes the optical loss and maximize quality factor of

the cavity. Finally, an angled ion beam was used to efficiently create V_B^- in the thin hBN flake onto the suspended structure as shown in figure 4.1 c.

4.4. Ion Implantation

This method shows the possibility of the deterministically defect generation, which enables to localize the dipole emitter in the electric field maxima of the cavity. We emphasize that the implantation condition is of critical importance as the creation of boron vacancy in a thin flake requires special conditions as previously reported. [213] TRIM calculation was performed to obtain the optimal condition for generation of defects within 20 nm of hBN using a nitrogen beam. Here we simulated a 5 kV, N+ beam into amorphous BN (density= 2.1 g/cm3) at 60° incidence angle. Boron vacancies were almost entirely located within the 20 nm with a distribution maximum at 5 nm (Figure 4.5).
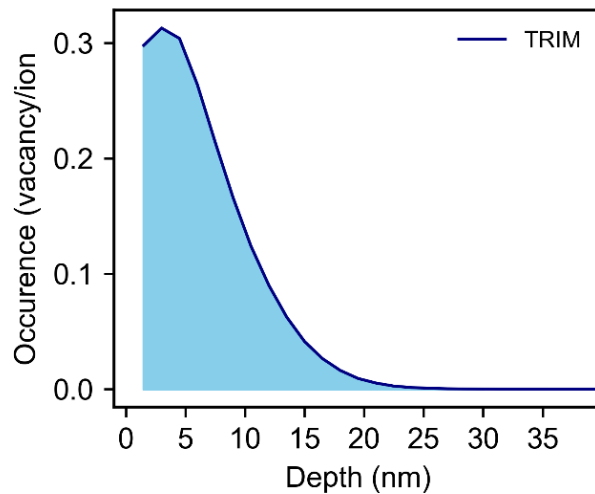
Figure 4.5. *TRIM simulations of boron vacancy distribution generated by 5 KeV ion energy and 60-degree angle of incident.*

The creation of boron vacancy defects was achieved by focused ion beam irradiation in a Helios G4 PFIB UXe DualBeam microscope. Ion irradiation was performed at 60° incidence angle with respect to the surface normal to maximize the number of defects in a thin flake. A N_2 source was used, the beam energy and current were 5 kV and 75 pA respectively. A square irradiation pattern was defined over the resonator structure

containing the hBN flake. The irradiation area and time were set to achieve an ion fluence of 1×10^{14}. After the fabrication steps, Energy-dispersive X-ray spectroscopy (EDS) analysis and PL spectrum was conducted to verify the presence of hBN flake on top of TiO_2 resonator. Figure 4.6 a-e shows the SEM image and EDS mapping of the fabricated structure. A uniform elemental distribution of Boron, Nitrogen, Oxygen and Titanium confirm the successful fabrication of hBN/TiO_2 hybrid ring structure. Moreover, the hBN layer was confirmed by the PL measurement (figure 4.6 f). The PL spectrum from the center part of the structure (red dash circle in figure 4.6 a) shows two apparent peaks. The 573-nm sharp peak indicates the hBN E_{2g} (1365 cm^{-1}) Raman shift under a 532 nm laser excitation. Moreover, a broad V_B^- signal around 800 nm was also observed confirming the hybrid nature of these structures. We note that the spectral range was limited by our lowest spectrometer grating to show both peaks at the same time.
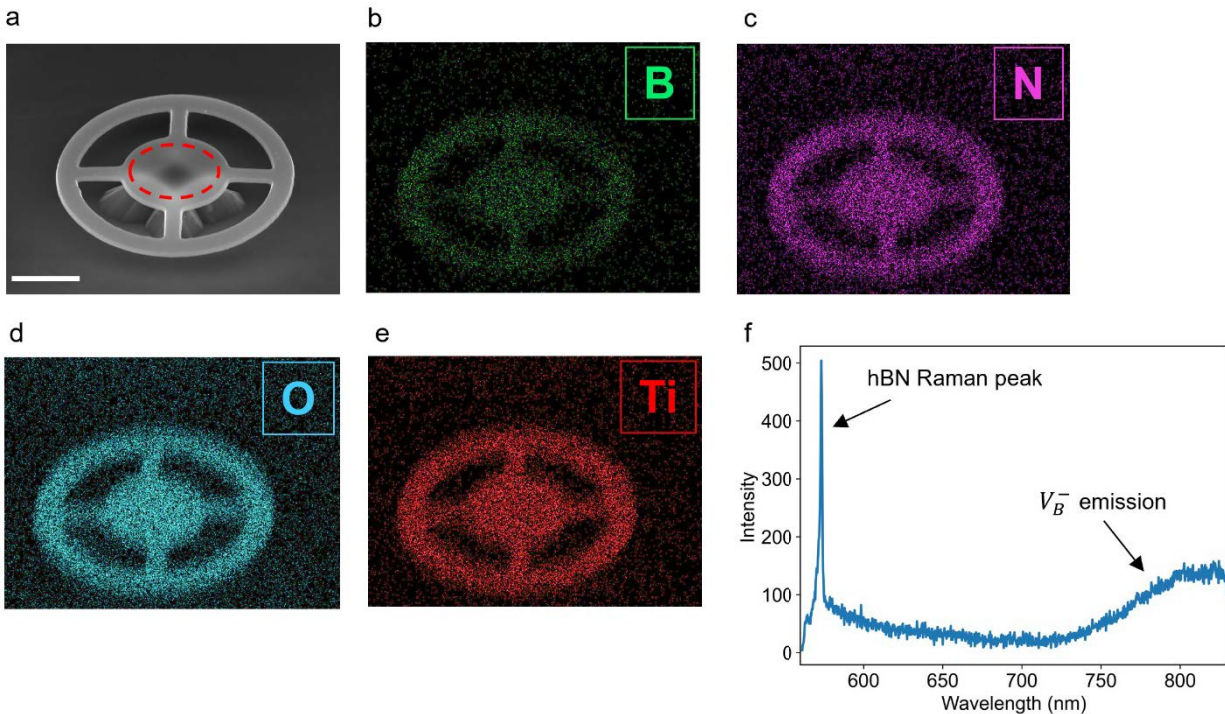
Figure 4.6. Elemental analysis of hBN/TiO₂ hybrid structure. *(a) Tilted SEM image of the suspended ring resonator and the corresponding EDS mapping of (b) Boron (c) Nitrogen (d) Oxygen (e) Titanium element distribution. The scale bar is 2 μm. (f) PL spectrum recorded from center of the structure as indicated by a red circle.*

4.5. FDTD simulations

The FDTD was used to calculate the WGMs of a TiO_2 ring resonator using commercial software (figure 4.7). The TiO_2 ring resonator with four arms clamping on the central disk was embedded in vacuum. All dimension parameters of the whole structure and the refractive index of TiO_2 were taken from the experiment. TE/TM WGMs are excited with an in-plane electric/magnetic dipole lying on the ring avoiding the clamping points, respectively. The dipole orientation was perpendicular to the curvature of the ring. Perfectly Matched Layers (PML) were applied in all three directions. A time monitor was used to capture the decay of the field and convert the spectrum in frequency domain. The cut off wavelength of TM modes was around 1050 nm which was mainly controlled by the thickness of the ring resonator.
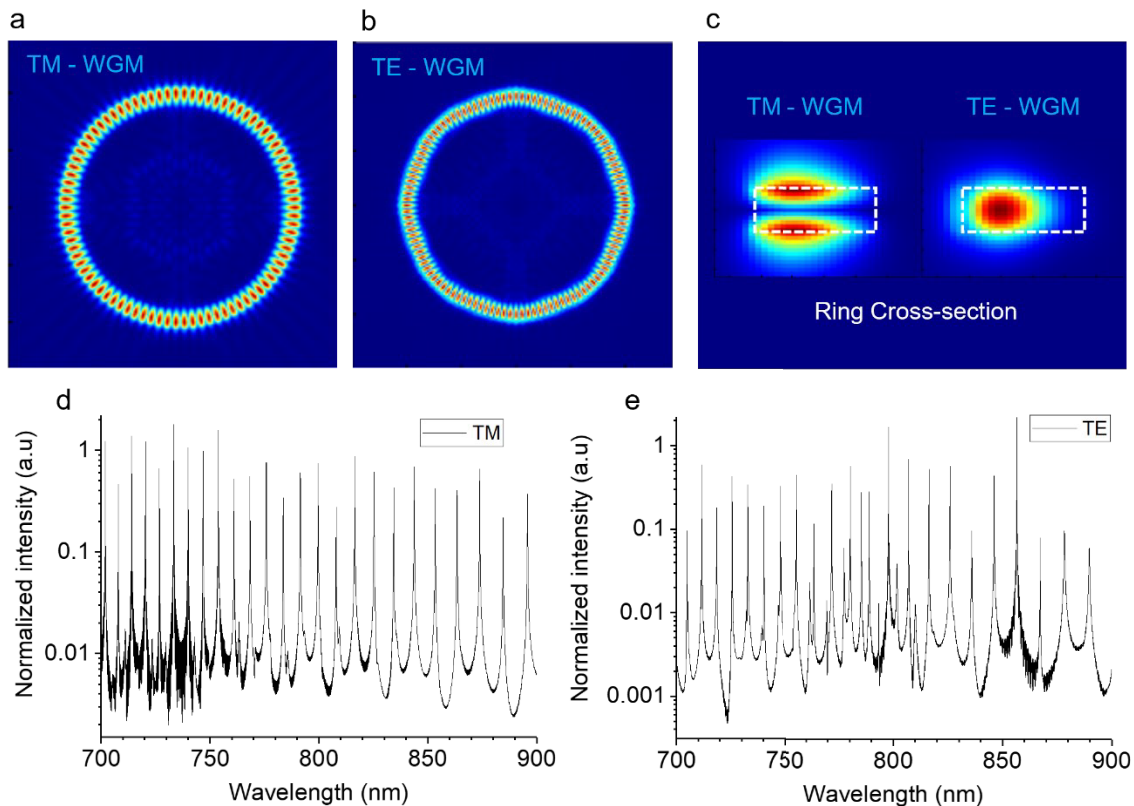
Figure 4.7. FDTD simulation of the suspended ring resonator. *(a) top view of the fundamental TM modes (b) top view of the fundamental TE modes (c) cross-sectional view of the TM and TE modes showing magnetic and electric field distribution of the fundamental modes inside the resonator. spectra of the fundamental (d) TM and (e) TE modes.*

Figure 4.7a and b show the top view of $|E|^2$ field intensity of the fundamental TM and TE modes, respectively. It is clearly visible that the WGMs are well confined inside the ring resonator, whilst a small amount of loss is seen in the supporting rods (four junctions) as seen by light coupling to the junctions. As shown in the cross-sectional view for the TM and TE modes (figure 4.7c), one can observe that the Electric field profile of the WGMs concentrated around the middle of the device whilst the magnetic field maxima confined at the top and bottom surface of the resonator. This is of crucial important because it is expected that V_B^- matches with the Magnetic field of the WGMs which localized to the surface of the device. The spectra of the fundamental modes as shown in the figure 4.7 d and e, confirms the FSR of about 7 nm for the 8 µm ring resonators.

## 4.6. PL Characterization of the Ring resonators

PL spectra were recorded using a lab-built confocal setup. The devices were excited with a 532 nm continuous wave laser collimated and directed using several mirrors and lenses. The laser was focused onto the sample by a 100x and 0.9 NA objective forming around 500 nm spot through a 4f scanning system. The laser was scanned over the sample by a scanning mirror and the signals were collected by the same objective and transmitted back to the detectors. The signals were filtered by a 568 nm long pass filter and sent to a spectrometer (Princeton Instruments) or an avalanche photodiode APD (Excelitas) by a flip mirror. We characterized the coupling of V_B^- to the TiO$_2$ resonator using the confocal photoluminescence setup. Figure 4.8 a shows the confocal image of the hybrid resonator. The resonance modes were predominantly observed from the bright spots as indicated by the red circle while we collected the signals from the center of the disk as the off-resonance region (blue circle). The photoluminescence spectrum collected from the center of the ring (denoted as "off-ring") is shown in figure 4.8 b (blue spectra) and a relatively broad emission spectrum of V_B^- spanning from 750 to 850 nm was observed. In contrast, when V_B^- was excited on the ring (denoted as "on-ring", red spectra), superimposed peaks resulting from the coupling of V_B^- emission to WGM of the rings were observed. Since the WGMs of the resonator cover entire V_B^- emission range with short FSR of ~7 nm, overall V_B^- signals were significantly enhanced compared to those of from uncoupled region. The coupled signals were collected from the scattering point (the bright

spot) where the photons partially outcoupled into the objective. The analysis of the individual peak from high resolution spectra is shown in figure 4.8 c. A quality factor ($Q = \lambda/\Delta\lambda$) of 2137 was obtained after fitting the peak with Lorentzian function. To further investigate the enhancement of the coupled signals, PL intensity was measured for both on-ring and off-ring emissions as a function of excitation power shown in figure 4.8 d. The intensities for both cases, were integrated over the whole range of V_B^- emission, and the resulting data were fitted with the equation $I = (I_{sat}P)/(P + P_{sat})$, where I_{sat} is the saturation intensity, and P_{sat} is the saturation power. We determined saturation intensity of 0.405 MHz and 0.152 MHz for the on-ring and off-ring, respectively, and we observed the enhancement by a factor of about 3 and 7 in the saturated and unsaturated regimes.
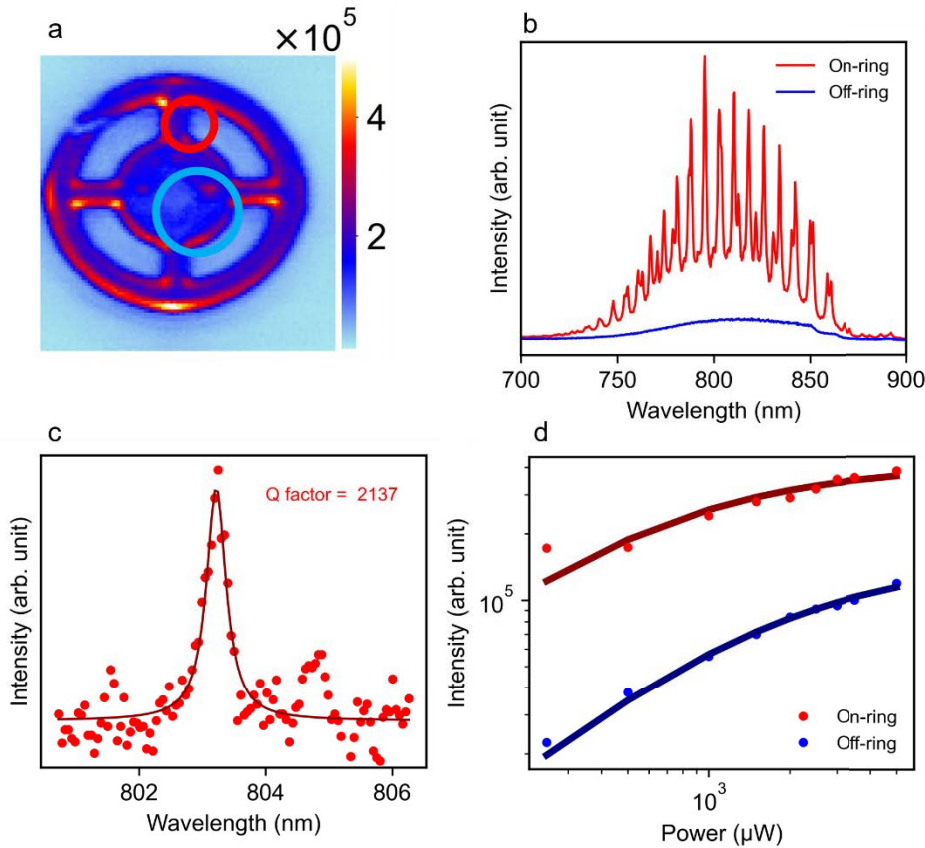
Figure 4.8. Optical characterization of the micro-ring resonator. *(a) confocal scanning image of the hybrid resonator. Red and blue circles indicate collection spots corresponding to On and Off the ring, respectively. Scale bar: 4 µm. (b) PL spectrum collected on (red) and off (blue) the ring (c) High-resolution spectra of the WGMs fitted by Lorentzian function yielding a quality factor of ~2100 for the fabricated ring resonator (d) Integrated PL intensity of the signals collected on (red) and off (blue) the ring at increasing excitation power.*

A pristine ring resonator without hBN was characterized as a reference. Background photoluminescent from polymer/contamination residuals was excited by a 6-mW green laser and signals were collected either by an APD or a spectrometer as shown in figure 4.9 a and b, respectively. The fundamental modes were observed when background photons coupled to the ring resonator and scattered out to the objective. The spectrum was recorded from the scattering point indicated by a black arrow in the PL map. The Q-factor of an array of ring resonators was measured via a similar method as described figure 4.8 c. Statistical analysis of the Q-factor (figure 4.9 c) shows an average of 1800 for the devices fabricated in our method.
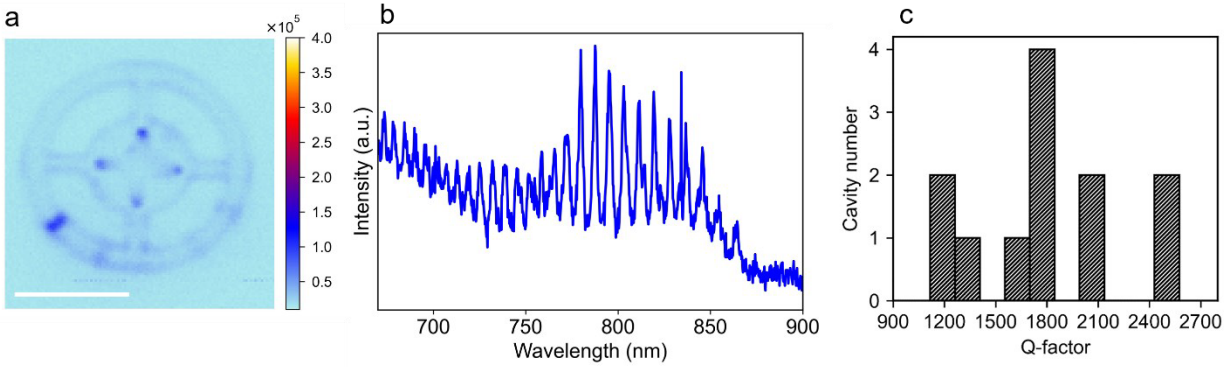
Figure 4.9. Optical characterization of a micro-ring resonator in the absence of hBN. *(a) PL map of the suspended ring resonator without hBN. The scale bar corresponds to 4 µm (b) PL spectrum collected from a scattering point as indicated by the arrow in the map. (c) statistical analysis of an array of suspended ring resonators*

4.7. ODMR Characterization

To further characterize the hybrid devices, we employed ODMR spectroscopy to map spin transitions of the coupled V_B^- in local and non-local excitation configurations. To this end, samples were placed on a chip holder in the vicinity (~ 50 um) a wire antenna. To generate microwave signals, the current was passed through the antenna by a RF generator (AnaPico APSIN) and amplified (minicircuits, ZHL-16W-43-S+). Microwave was swept over 3.2 to 3.8 GHz and PL signals were collected for 10 ms while the microwave field was on and off. The ODMR contrast was measured from the difference between the recorded signals in each frequency value. The ODMR signals were then fitted with a double Cauchy-Lorentz distribution function as outlined below:

62

$$f(x; A, \mu, \sigma) = \frac{A_1}{\pi}\left[\frac{\sigma_1}{(x-\mu_1)^2+\sigma_1^2}\right] + \frac{A_2}{\pi}\left[\frac{\sigma_2}{(x-\mu_2)^2+\sigma_2^2}\right] \qquad\qquad (4.1)$$
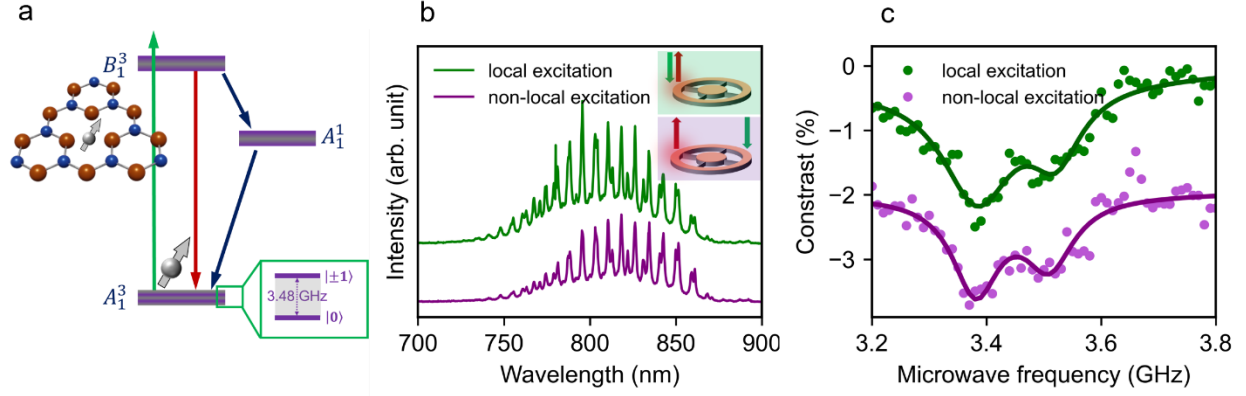
Figure 4.10. ODMR measurement of a coupled V_B^-. *(a) Schematic of the V_B^- defect and an energy diagram showing the main optical pumping cycle and the alternate cycle though the metastable state. (b) PL spectrum from coupled V_B^- in local and non-local configurations. The inset schematically shows these configurations. (c) ODMR measurement from coupled V_B^- in local and non-local configurations. ODMR data (dots) were fitted with a double Cauchy-Lorentz function (solid lines) as discussed previously.*

The spin defect in hBN and its simplified electronic level structure is schematically depicted in figure 4.10 a. The defect shows a triplet ground state (A_1^3) with as zero field splitting of 3.48 GHz between the two spin states. We evaluate spin transitions from V_B^- that coupled to WGM in the local and non-local configurations. In the local configuration, the optical collection and excitation spots were overlapped, while at the non-local configuration, the excitation of the microscope was offset 180° on the ring away from the collection spot. The results and the schematic configuration of both scenarios are shown in figure 4.10 b-inset. The spectra recorded from non-local configuration is shown in figure 4.10 b (purple) with similar features as the local excitation (green) indicating the efficient coupling of V_B^- into the TiO₂ ring resonator. Figure 4.10 c shows the corresponding ODMR signals for both excitation schemes. By sweeping a microwave from 3.2 to 3.8 GHz, a reduction in the photoluminescence of the V_B^- was detected at 3.4 and 3.5 GHz. These contrasts are the result of transitions from $m_s = 0$ to $m_s = \pm 1$ in the ground state which are driven by the microwave field (figure 4.10 a). This verifies that V_B^- emits photons carrying spin information into the resonator and effectively coupled to the

WGMs. Both excitation scheme showed similar ODMR contrast with slight differences stemming from lower collection efficiency through non-local excitation.

Ultimately, to showcase the sensitivity of the spin defect to the field strength, we measured the microwave power dependence of the ODMR contrast in the non-local excitation scheme (figure 4.11).
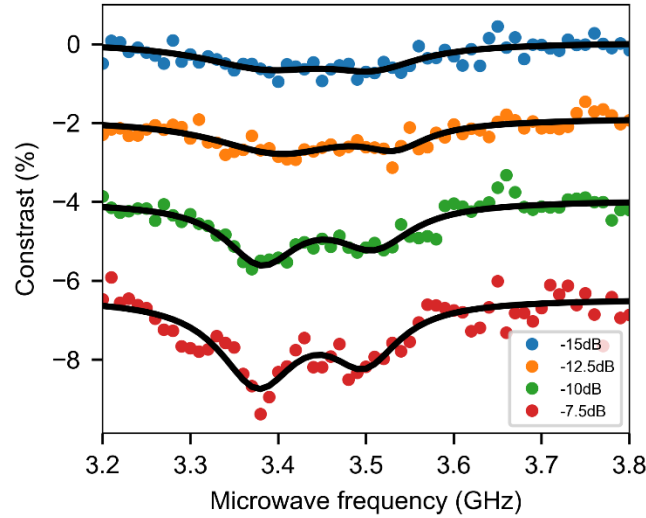
Figure 4.11. ODMR contrast as a function of microwave frequency collected for different microwave power from -15 dB* to 7.5 dB.

* Decibels (dB) indicates an increases or decreases of power level in microwave system. It is a convenient logarithmic ratio of two radiofrequency (RF) power and unlike other SI units, dB is relative. Here, a negative number of dB indicates loss or reduction in signal strength.

4.8. Conclusion

In summary, we have developed a method for fabrication of a hBN/ TiO$_2$ resonators with high Quality factors exceeding ~ 2000. Coupling of V$_B^-$ to the WGM results in the increase of photoluminescence of about 7 and 3 in the unsaturated and saturated regimes, respectively. Finally, we demonstrated the coupling of V$_B^-$ via two excitation configurations. Importantly, in a non-local configuration, the PL intensity and the ODMR signal collected from guided photons, indicating efficient coupling of V$_B^-$ to TiO$_2$ ring

resonators. Our results are promising for scaling up integration of layered materials with nanophotonic resonators.

Chapter 5: Coupling of single-photon emitter in hexagonal boron nitride to the bound state in continuum (BIC) mode of TiO$_2$ nanopillars

This chapter demonstrates the hybrid integration of native quantum emitters in hBN to the BIC mode of TiO$_2$ nanopillar arrays. We first detailed the mechanism of the formation of dark state in these structures which results in an extremely high-quality factor and then we demonstrate the possibility of strong coupling between the two systems. we experimentally observed anti-crossing behavior and Rabi splitting which are persuasive evidence of strong coupling regime.

5.1. Abstract

Cavity quantum electrodynamics describes coupled systems comprising of optically active emitters with atom-like transitions, such as single-photon emitters (SPEs), and optical cavities that enable fundamental light matter interactions. In the strong coupling regime, SPEs and cavity photons coherently exchange energy leading to two new hybrid states that significantly modify the optical responses of the originally uncoupled or weakly coupled states. Despite considerable efforts, the strong SPE-cavity coupling has only been observed at cryogenic temperatures due to the lack of stable, coherent single-photon sources to satisfy strong coupling conditions. Here, we introduce a new approach using point-defects purposely created in a two-dimensional few-layer-thick hexagonal boron nitride (hBN) film as SPEs and a robust photonic cavity with arbitrarily high quality-factor based on bound-state-in-the-continuum (BIC) concept. We observe, a strong coupling between SPEs and BIC photons characterized by a Rabi splitting of ~7 meV at room temperature under ambient conditions. The coupling strength can be tuned by varying detuning energy that is strongly supported by theoretical calculation. Our findings unveil new opportunities for exploiting the BIC cavity to realize the long-sought strong coupling with SPEs, ultimately for the development of quantum-based devices operating at ambient conditions.

5.2. Introduction

Coherent interaction between single-photon emitters and photons trapped in a cavity lie at the heart of quantum optics. This can be achieved by establishing strong coupling regime within the two systems. As we discussed in chapter 2, this leads to a reversible process in which the quantum information can be exchanged coherently between the two systems, leading to the formation of two new eigenfrequencies ($\omega_{\pm}$) often referred to as vacuum Rabi splitting. A true strong coupling is highly desirable in quantum technology such as nonlinear quantum optics, quantum entanglement, quantum communication and quantum sensing.

To achieve strong coupling between SPEs and photonic cavities, several criteria need to be satisfied. Firstly, the SPE transition energies must coincide with cavity modes to satisfy a term known as spectral matching ($\omega_p = \omega_m$). Secondly, the SPEs must be precisely positioned at the electric field antinode to meet spatial matching and finally, the systems require further refinement to match the dipole orientation with the polarization of the cavity mode. As we discussed earlier, the coupling strength (g_0) increases in photonic cavities with high quality-factor (Q) and small mode volume (V_0) as g_0 scales with $Q/\sqrt{V_0}$ that imposes severe challenges for cavity fabrication processes. Moreover, another major issue arises when there is only a fixed small volume to host SPEs, while by current technology, the SPE positioning, emission wavelength and dipole orientation are not yet precisely controllable. Strong coupling has been reported in many coupled systems including single semiconducting quantum-dots in photonic crystal cavities (high Q, small V_0) [233, 234], single molecules in plasmonic cavities (low Q, small V_0) [235, 236] and for colloidal quantum-dots in Fabry-Perot cavities (low Q, large V_0) [237]. However, progress towards practical large-scale quantum devices has been restricted by the scalability and versatility of these cavity nanostructures and a proper single-photon emitter.

Recently, the bound state in the continuum (BIC) has become an intriguing concept to design optical cavities. As previously discussed, in the conventional cavities, photons can be trapped in a closed system (Hermitian Hamiltonian system) formed by breaking the symmetry in their photonic bandgap. Photons, therefore, are not allowed to exist in the

bandgap and their access to the radiation channel is forbidden. In BIC concept, by contrast, photons are completely confined within the structures even though their frequency lies in the radiation continuum (figure 5.1).
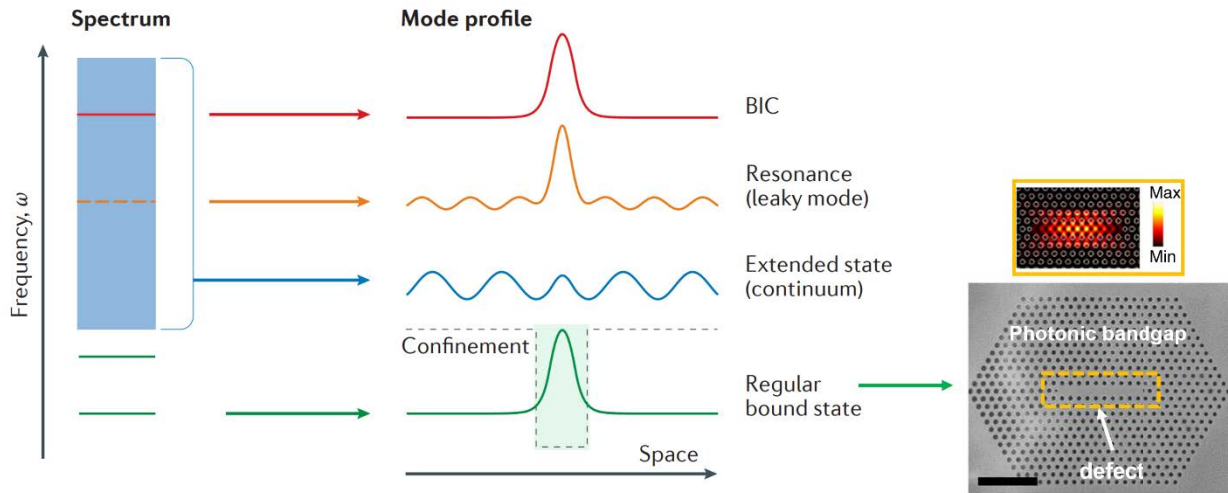
Figure 5.1. Schematic illustration of BIC concept. *The blue shaded area in the frequency spectrum represents the continuum of extended states and green lines show the discrete energy level. The regular light confinement can be observed, for example, by creating a defect in photonic bandgap (SEM image). Photons only exist in the defect as indicated by the white arrow. Electric field profile of the defect area is shown in the orange box. Some state can couple to the extended wave and radiate away (orange) showing leaky mode of the system. BIC (red) is a bound state that lies within the continuum and remains localized with radiation lifetime extended to the infinity (dark state).*

BIC concept was first proposed by Neumann and Wigner in 1929 for the electronic bound states saying that solution for Schrödinger can result in isolated eigenvalues reside in the continuum of energy state. [238, 239] Although this proposal was never experimentally verified, BIC formation has been observed for other wave phenomena such as light. [240-244] BICs, theoretically, can generate a dark state with infinite radiative lifetime arises from the destructive interference in periodic nanostructures with at least one dimension extending to infinity. [245, 246] Due to the peculiar non-decaying nature ($\tau_{BIC} \to \infty$) of the trapped photons, BIC cavity can have arbitrarily high quality-factor that is advantageous for recent important progress on nonlinear optics [247, 248], functional metasurface [249, 250], lasing [251, 252], and most recently on Bose-Einstein condensation. [253]

Herein, by exploiting the extraordinary advantages from the infinite Q-factor of a BIC cavity and native SPEs in few-layer hBN, we realize strong coupling in a true quantum-optical systems at room temperature. Figure 5.2 illustrates the concept of coupling between a SPE with a horizontal transition dipole (yellow sphere with green arrow) and BIC formed by an array of sub-diffractive vertical magnetic dipoles generated by scattering of the incident electric field when interacts with high refractive index objects. Strong coupling regime is reached when the coupling strength g_0 exceeds the mean of cavity loss rate κ and the emitter decay rate γ, i.e. $g_0 \gg (\kappa + \gamma)/2$. In the case of BIC, this condition reduces to $g_0 \gg \gamma/2$, since, according to equations 2.17 and 2.18, $\kappa = \tau_{BIC}^{-1}$ equals 0 and the Q-factor extend to infinity. Furthermore, BIC modes are not spatially restricted to the defect point, and unlike photonic bandgap cavities, they can support cavity modes throughout their entire structure. Hence, for BIC cavities, the strong coupling is no longer restricted by the cavity loss that eases the existing challenge for SPE integration and facilitate the fabrication of optical cavities sustaining both high-Q and small-V simultaneously.
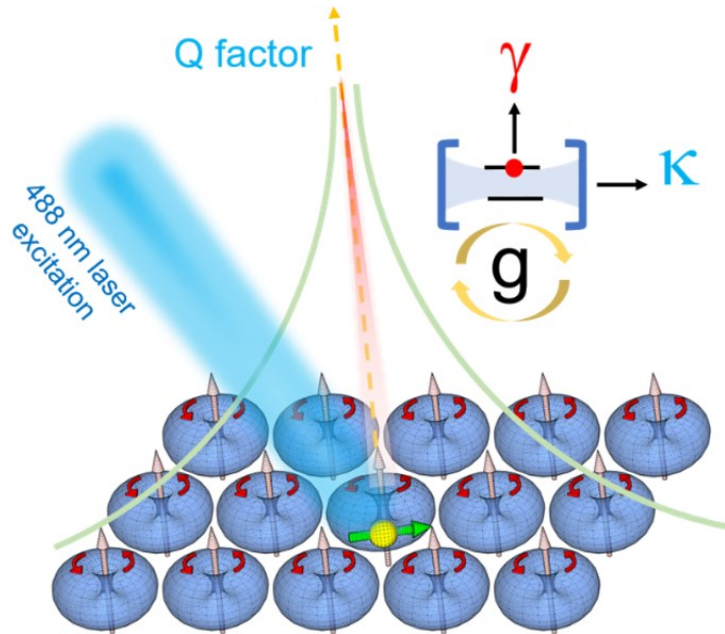
Figure 5.2. Schematic illustration of a single-photon emitter located in a BIC cavity. *BIC mode is supported by vertical magnetic dipole resonance (gray arrows), associated with an electric-field distribution represented by blue doughnuts and direction circulating in x-y plane (red arrows). An SPE (yellow sphere), which has optical dipole (green arrow) lying in x-y plane and spatially overlaps with the electric-field, can couples with BIC mode when condition $g > (\kappa + \gamma)/2$ is satisfied.*

5.3. Fabrication method

To experimentally demonstrate this concept, we employ defect-induced single-photon emitters from hexagonal boron nitride (hBN) to couple with symmetry protected BIC in a two-dimensional nanopillars array made of titanium dioxide (TiO$_2$). In this work, we chose native SPEs that exhibit narrow emission (i.e., ~ 3nm) at visible wavelengths (i.e., 500 – 600 nm). The narrow linewidth emission of the hBN SPEs is critical to achieving strong coupling regime. Since the mechanism of BIC relies on Mie scattering [171, 254, 255], TiO$_2$ was again chosen due to a relatively high refractive index (n ~ 2.5) at optical frequencies which maximizes scattering efficiency in this mechanism and therefore, they are favorable to create high-Q BIC cavity. Since, the underlying SPEs have a horizontal transition dipole orientation, we design TiO$_2$ nanopillar arrays that supports BIC originated from vertical magnetic dipoles, which has an electric field with in-plane Poynting vectors. This will assure the strong mode coupling between the SPE fluorescence and the BIC mode. In the following, we first describe the fabrication method and characterization of the hybrid device, and then we analyze the coupling behavior of the two systems.

Nanopillar fabrication. In order for the cavity to be able to support BIC modes at the emission wavelength of the SPEs (500-600 nm), arrays of nanopillars with 260 nm diameter separated by 40 nm, were fabricated through top-down lithography method. To this end, A 150-nm thick film of TiO$_2$ was deposited onto a quartz substrate by ion-assisted deposition method (same method as explained in detail in Chapter 4, figure 4.2), and a 30-nm-thick film Cr film was then deposited onto the sample by electron-beam evaporation as a sacrificial layer. A negative electron-beam resist, hydrogen silsesquioxane (HSQ) was spin-coated on Cr/ TiO2/quartz at 5000 rpm for 60s, followed by baking at 120°C for 2 minutes and at 180°C for another 2 minutes. The sample was then subjected to an electron beam lithography system where the sample was pattern using 100 KeV electron beam. Afterwards, the pattern was developed for 4 mins by salty developer containing 1 wt. % NaOH and 4 wt.% NaCl aqueous solution and rinsed by DI water. The pattern was first transferred to the Cr layer via inductively coupled plasma reactive ion etching (ICP/RIE) system with a gas mixture of Cl$_2$ (15 sccm) and O$_2$ (2 sccm) at the chamber pressure of 10 mTorr. In the following step, Cr pattern was used as hard mask to transfer the pattern into the underlying TiO$_2$ film using CHF$_3$ gas at the chamber

pressure of 32 mTorr. Finally, the Cr metal mask was stripped away by immersing in a Chromium etchant solution for 15 minutes. Figure 5.3 a shows the optical image of the BIC arrays and figure 5.3 b and c is the magnified optical and SEM image of the structure that supports 590 nm mode, respectively.
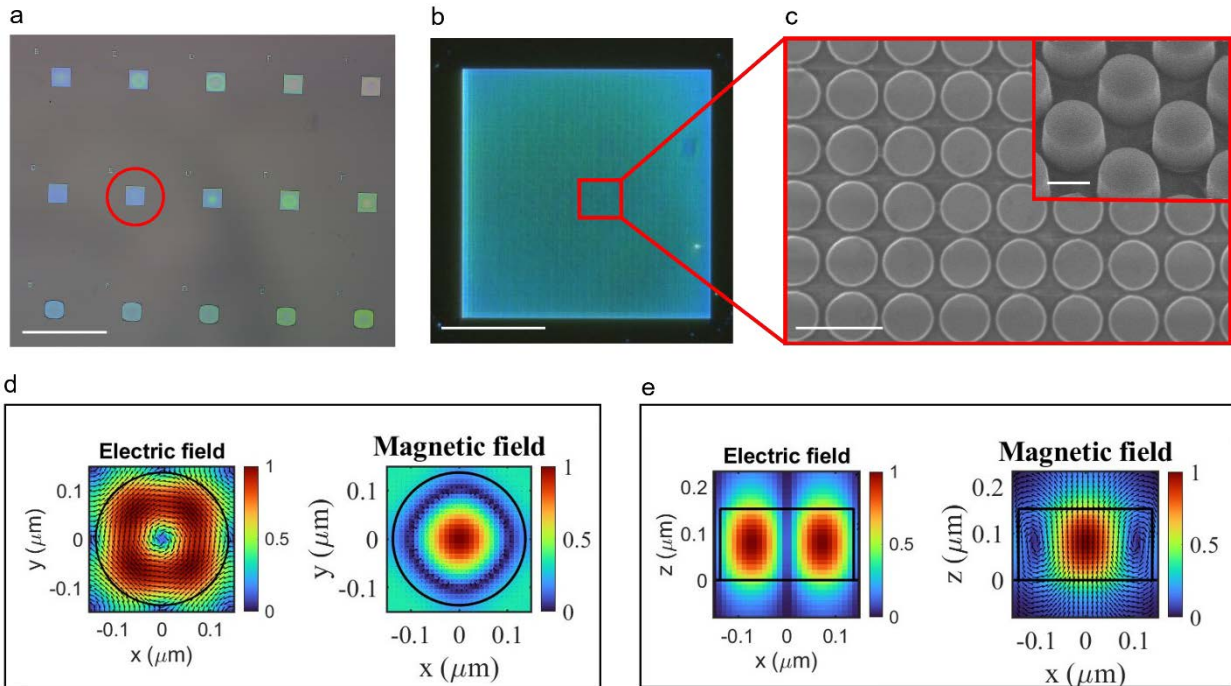
Figure 5.3. BIC nanopillar arrays. *(a) optical image of the fabricated BIC structures with various size. Scale bar is 200 μm. (b) magnified optical image of the nanopillar arrays (indicated by the red circle) that supports that supports BIC modes at 590nm. Scale bar corresponds to 20 μm. (c) top-view SEM image of the nanopillar arrays and inset is the tilted image of the structure. The scale bars correspond to 500nm and 200nm, respectively. Electric and magnetic field distribution simulated by FDTD method for the vertical magnetic dipole from d) top view (x-y plane) and e) side view (x-z plane) of the arrays.*

Figure 5.3 d and e illustrate electric field distribution for the magnetic dipole created by scattering from top and side view of the arrays. The distribution of electric field associated with the vertical magnetic dipole is concentrated within the nanopillars' peripheries in the x-y plane with the highest concentration at ~ 50 nm away from the centerand drops dramatically around the center (figure 5.3 e – left). Therefore, such circulating electric field enables the coupling with any optical dipole lying in the x-y plane. Furthermore, the field extends up to ~70 nm outside the cylinder along z-direction as shown in figure 5.3 e. This

results in high field overlap with the native emitters in a thin hBN film as we will discuss later in section 5.5.

hBN growth. A few-layer of hBN film was overgrown on a sapphire substrate by metalorganic vapor-phase epitaxy (MOVPE) following the method as reported previously. [256] More specifically, triethyl boron (TEB) and ammonia served as boron and nitrogen precursors respectively. The Sapphire substrate was initially functionalized with ammonia prior to hBN growth at a temperature of about 1000°C. The chamber temperature was subsequently elevated to 1350°C and the precursors were introduced into the chamber once the temperature was stabilized. To minimize parasitic reactions, the precursors were intentionally injected into the reactor with short pulses lasting 1 to 3 seconds. The thickness of the overgrown hBN was measured using AFM showing about 3 nm thick hBN film (figure 5.4 a-c).

hBN transfer. Milimeter-sized hBN film was transferred from Sapphire onto BIC structures using the wet transfer method (figure 5.4 d). Approximately a 300-nm PMMA (A4, Mircochem.) layer was spin-coated onto hBN/Sapphire substrate and baked at 120°C for 3 mins to evaporate the polymer solvent. The sample was then floated onto a 1M KOH aqueous solution to etch Sapphire interfacial layer and to detach from the hBN/PMMA film. After picking the floating film with a clean silicon substrate, the film was washed three times with DI water to remove the remaining base. Similarly, the floating hBN/PMMA film was picked up by the target substrate in such a way to cover the entire arrays of the BIC structure. To gently remove water residue without the formation of wrinkles and bubbles, the substrate was placed in a vacuum desiccator for 30 minutes, followed by heating on a hotplate for another 30 minutes. This step is critical since some wrinkles are thick enough to interfere with the BIC modes. Thereafter, PMMA film was removed in a warm acetone bath overnight and then the sample was cleaned by a UV ozone cleaner for 10 minutes to remove remaining polymer. Finally, to enhance adhesion between the film and substrate, the hBN/BIC sample was annealed on a hotplate at 500°C for 2 hours before measurements.
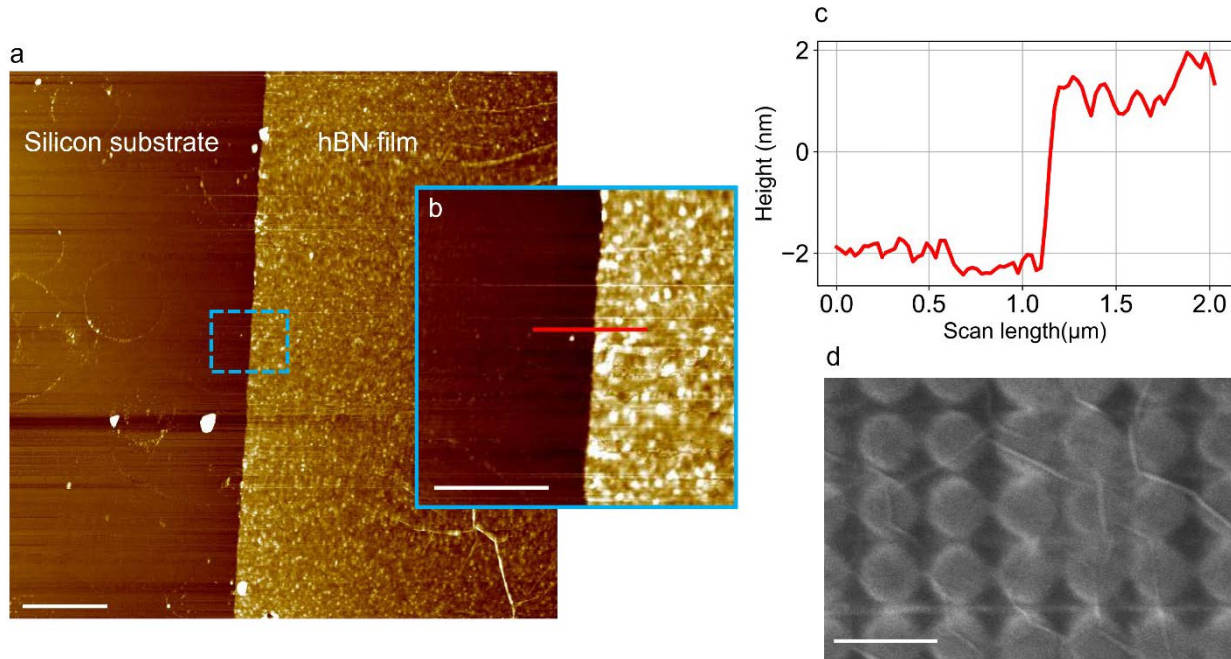
Figure 5.4. CVD hBN film transferred of BIC structure. *(a) AFM scanning image of the hBN film transferred on a silicon substrate. Scale bar is 5 µm. (b) magnified AFM image of the outlined section in (a). Scale bar corresponds to 2 µm. (c) AFM line-scan profile of the hBN film. The line scan is indicated by the red line in (b). (d) SEM image of the hBN/BIC structure via wet transfer method. Scale bar corresponds to 500 nm.*

5.4. Characterization of the BIC cavity

To analyze our cavity mode, we first characterized the BIC cavity by means of angle-resolved optical characterization. This was performed using a home-built back focal plane micro spectroscopy setup as shown in figure 5.5 a. To this end, an inverted optical microscope with a spectrometer equipped with a charged-coupled detector (CCD) camera was used for angle-resolved optical measurements. Light from a halogen lamp was focused on the sample surface via a 50X objective (Nikon, NA = 0.55) forming a 4µm spot. The signal was then collected by the other objective with the same characteristics and passed through a series of lenses. The back focal plane was then imaged onto the slit of the spectrometer and the wavelengths were dispersed by a single grating groove density of 150 g/mm, giving spectral resolution of 0.34 nm/pixel. This measurement provided an angular-resolved spectrum of the sample in a single image as shown in figure 5.5 b.

Figure 5.5 b illustrates the angle-dependent nature of multipolar radiation generated by field scattering due to interaction with the nanopillars. The transmission signal tapers down as it approaches 0° angle and exhibits a dark state where the field vanishes at exactly $\theta = 0°$. This behaviour indicates the formation of symmetry-protected BIC mode which is coinciding with 589.3 nm as indicated by a white arrow in figure 5.5 b. The multipolar analysis reveals that the BIC mode originates from the vertical magnetic dipole as shown in figure 5.2. [257] It is worth noting that the electric field maxima exist on every nanopillar and persists over almost entire nanostructure arrays. This ensures the coupling between the randomly distributed defects in 2D hBN and the electric field hotspot. Hence, observing strong coupling regimes becomes more versatile and scalable as compared to conventional cavities where the electric field hotspot located within a specific area (as shown by the electric field distribution in figure 5.1)
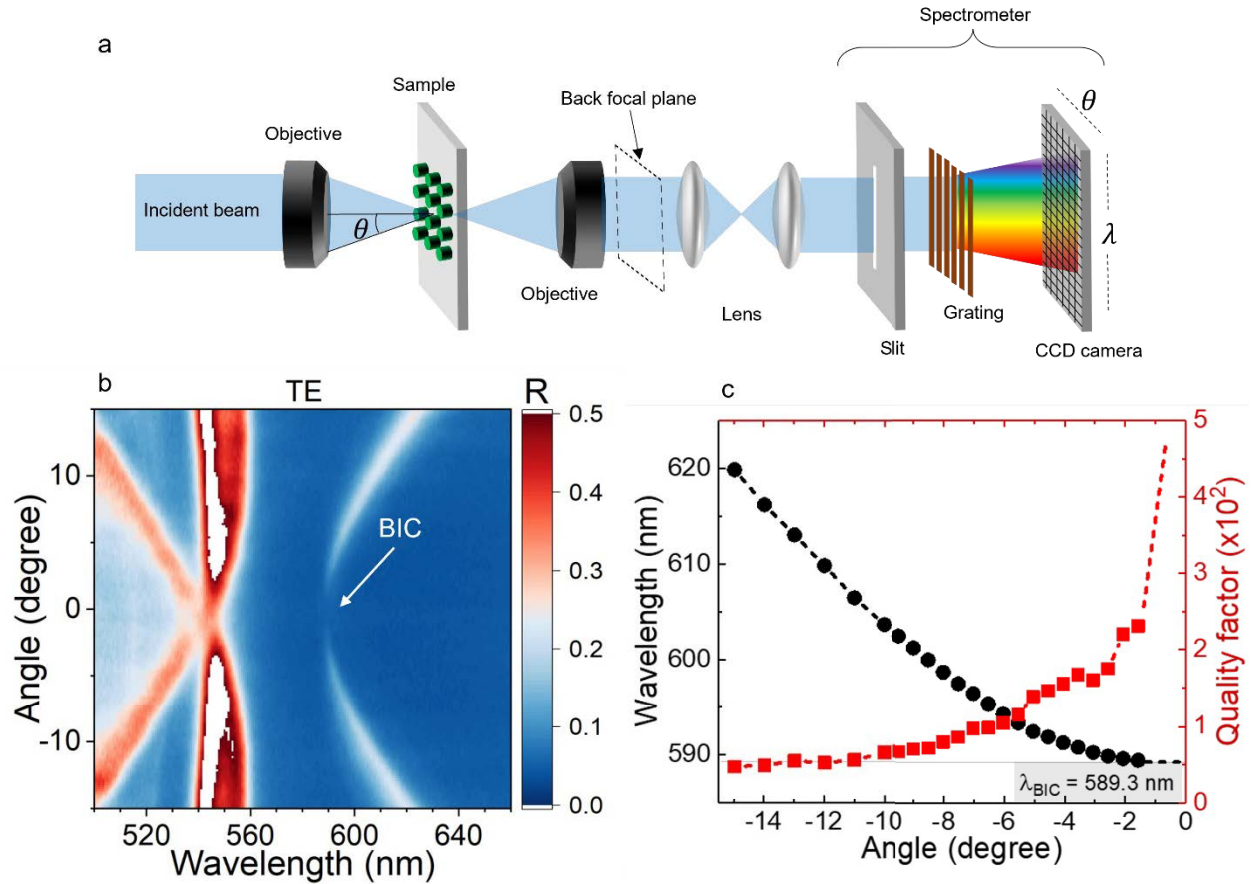
Figure 5.5. Optical characterization of a BIC cavity. *(a) schematic illustration of spectrally angle-resolved back focal imaging setup. (b) angle-resolved spectra of the TiO₂ nanopillars taken in transverse electric (TE) configuration showing vertical magnetic dipole BIC resonance at λ_{BIC} = 589.3 nm. (c) Experimental resonance wavelengths along BIC band (black circles) and Q-factors (red squares), and calculated resonance wavelengths (black curve) and Q-factor (red curve).*

The quality factor of a resonance is defined by $Q(\theta) = \frac{\lambda(\theta)}{\Delta\lambda(\theta)}$, where $\lambda(\theta)$ is the resonance wavelength and $\Delta\lambda(\theta)$ is the spectral full width at half-maxima (FWHM) at a specific collection angle θ. The angle-dependent resonance of the BIC band $\lambda(\theta)$ is represented by black circles in figure 5.5 c and the corresponding Q-factor (red squares) increases dramatically as a result of reducing linewidth when it approaches zero angle. The highest Q-factor measured is 230 at the near normal incidence θ = -1.5°, which is limited by our setup resolution. Theoretically, the Q-factor of the BIC resonance in symmetric nanostructure arrays could reach infinite at absolute zero angle where the field vanishes (red dash-line).

It is worth mentioning that the TiO$_2$ must remain amorphous to be able to support Mie scattering and in turn the BIC modes. In our fabrication process, to increase adhesion between the hBN film and BIC structures, the sample experienced temperature history which has huge impact on the final optical properties. We have observed that the BIC mode disappeared if the sample was annealed above 500°C as shown in figure 5.6. Figure 5.6 a shows the angle-resolved spectra of the BIC structure annealed at 500 °C and the BIC band remained at zero angle of incident. However, when the same sample was annealed at 700°C (figure 5.6 b), the BIC mode disappeared as a result of recrystallization of TiO$_2$ (figure 5.6 c and d).
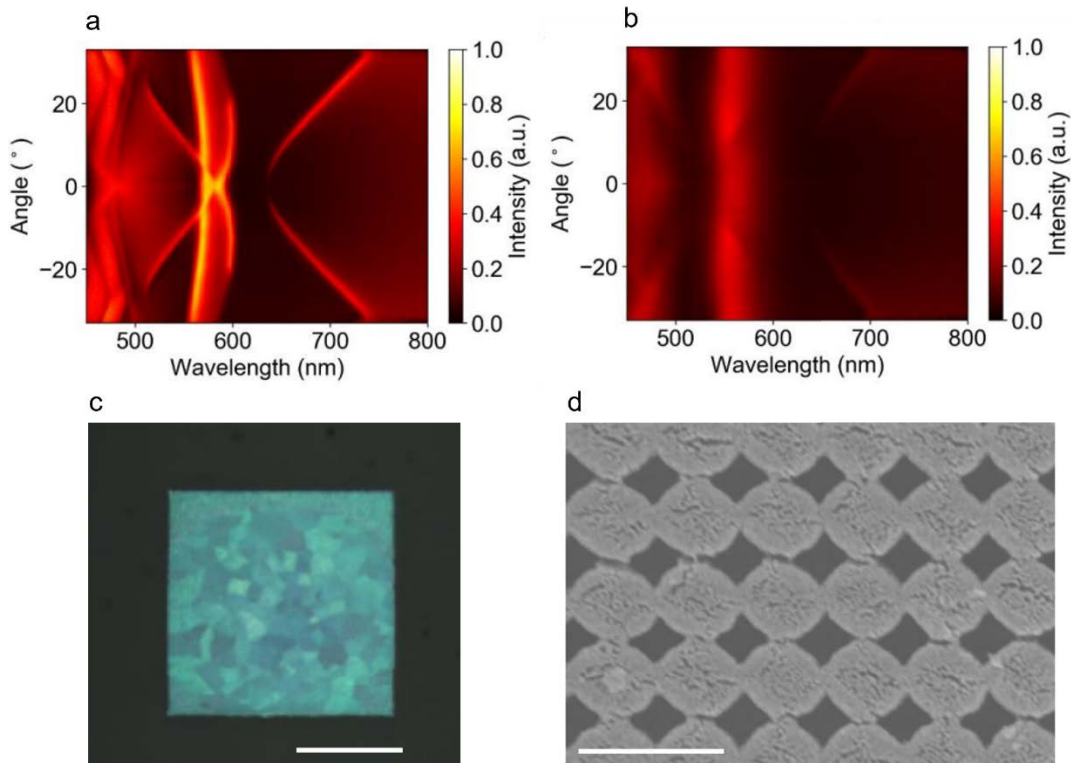
Figure 5.6.The effect of high temperature annealing on optical properties of TiO$_2$ nanopillars. *Angle-resolved spectra and BIC structure annealed at (a) 500 °C and (b) 700 °C. (c) optical image of the BIC arrays annealed at 700 °C. Scale bar is 20 μm. (d) magnified SEM image of the sample shown in (c). Scale bar corresponds to 500 nm.*

5.5. Characterization of native SPEs in the hBN film

The optical measurements of the native SPEs were carried out on a lab-built confocal microscope. We used a 532 nm continuous-wave laser for the excitation and the laser was scanned over the sample by a X-Y piezo scanning mirror (FSM300TM, Newport Crop.). A 100x objective (Nikon, 0.9 NA) was used to focus the laser onto the substrate forming a spot of about 500 nm. The PL signals were collected by the same objective and transmitted back through a dichroic mirror towards the detectors. A long-pass filter was used to filter the laser leakage and an additional bandpass filter centered at 587 nm with 15 nm bandwidth was used to predominantly collect the emission from SPEs near resonance with BIC mode. The signals were then guided to a spectrometer (Princeton Instruments, Inc.) or fiber based HBT setup connected to two APDs (Excelitas) by a flip mirror. For the photon antibunching characterization, the timing and correlation between two APDs were done by a correlator module (PicoHarp300TM). We recorded the coincidence count histogram with a 64-ps bin width resolution. Figure 5.7 a shows the confocal PL map of a 50x50 μm^2 area on the hBN film revealing the bright fluorescence of 31 optically active emitters in the range of 587$\pm$7 nm, wherein 22 of them showing antibunching characteristics.
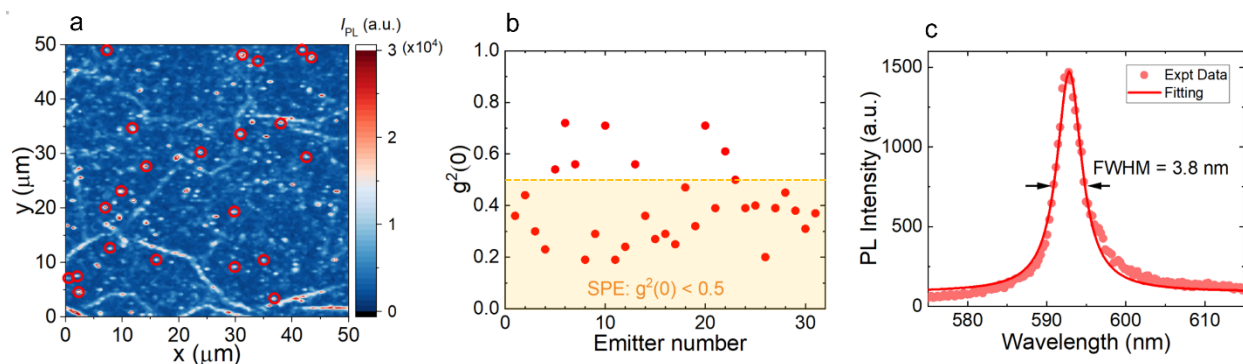
Figure 5.7. Optical characterization of native SPEs in hBN film. *(a) confocal PL image recorded from a region of 50x50 μm² hBN film grown on SiO2 substrate. 22 SPEs (with g2(0) < 0.5) emitting at (587 ± 7) nm were identified (red circles). (b) Statistics of g2(0) for all emitters showing high probability of SPE generation. (c) Representative PL spectrum of an SPE centered at ~592.9 nm with a FWHM of ~3.8 nm.*

As we explained earlier in the Chapter 2, a single-photon emitter is defined for two-photon correlation function at zero delay ($g^2(\tau = 0)$) smaller than 0.5. Figure 5.7 b illustrates the

statistical analysis of the native SPEs in the hBN film. The high density of SPEs created by our method increases the possibility of finding SPEs which fulfills all strong coupling conditions. A representative PL spectrum of an SPE is shown in figure 5.7 c, where the PL shows a peak at 592.9 nm and the FWHM is as narrow as 3.8 nm (~13 meV). These native SPEs exhibits one of the narrowest linewidths at room temperature and are hosted by layered material that offers unique opportunities for coupling to the cavity. Such especially narrow linewidth of SPEs in hBN, together with the vanishing linewidth of BIC resonance are key advantages to significantly lower the threshold for coupling strength in strong coupling regime, since $\kappa = 0$ and therefore, $g \geq (\gamma + \kappa)/2 = 6.5$ meV.

5.6. Coupling of SPE to the BIC modes of the nanopillars

We study the coupling of SPE and BIC modes by performing angle-resolved PL measurements using non-resonance excitation ($\lambda_{exc} = 488$ nm) by means of the same setup as explained in figure 5.5 a. Note that in addition to the emission from SPEs, the full PL spectrum of hBN consists of a weak broadband emission from the residual polymer after sample processing. When strong coupling conditions are not satisfied, the whole PL spectrum weakly couples with all the cavity modes leading to the brightening of the whole BIC band dispersion as shown in figure 5.8 a. on the other hand, figure 5.8 b, shows the angle-resolved PL spectra taken when the SPE strongly couples to the BIC mode. We observe a spectral splitting of the PL bands into upper (SPE-like) and lower (BIC-like) polariton branches with resonance wavelengths near zero angle located at ~586.7 nm and ~588.3 nm, respectively. Both bands show no signal at normal incidence clearly indicating the coupling between SPE and BIC modes. The photons emitted from the coupled SPE-BIC system at resonance is strongly antibunched (figure 5.8 c) that confirm the single-photon emission nature of the coupled emitter. Figure 5.8 d, displays the PL spectra extracted from the cavity mode (figure 5.8 a) and strong coupling cases (figure 5.8 b) at angle 3.8° (near normal incidence). In weak coupling regime (blue curve), the PL spectrum is a single peak centered at 590 nm with the FWHM of ~4 nm. When strong coupling regime is reached, the PL spectrum splits into two peaks located at 588 nm (SPE band) and 592 nm (BIC band) with spectral width of ~1.5 nm and ~1.4 nm, respectively, which are significantly narrower than those in the uncoupled case as discussed in figure

5.7 c. Such narrowing of PL linewidth is a typical result from strong coupling. The strong coupling between BIC cavity and an atomic-like two-level system can be explained by coupled-resonance model [258], taking into consideration the dispersion of photonic BIC band (figure 5.8 a) and SPE component (figure 5.7 c).
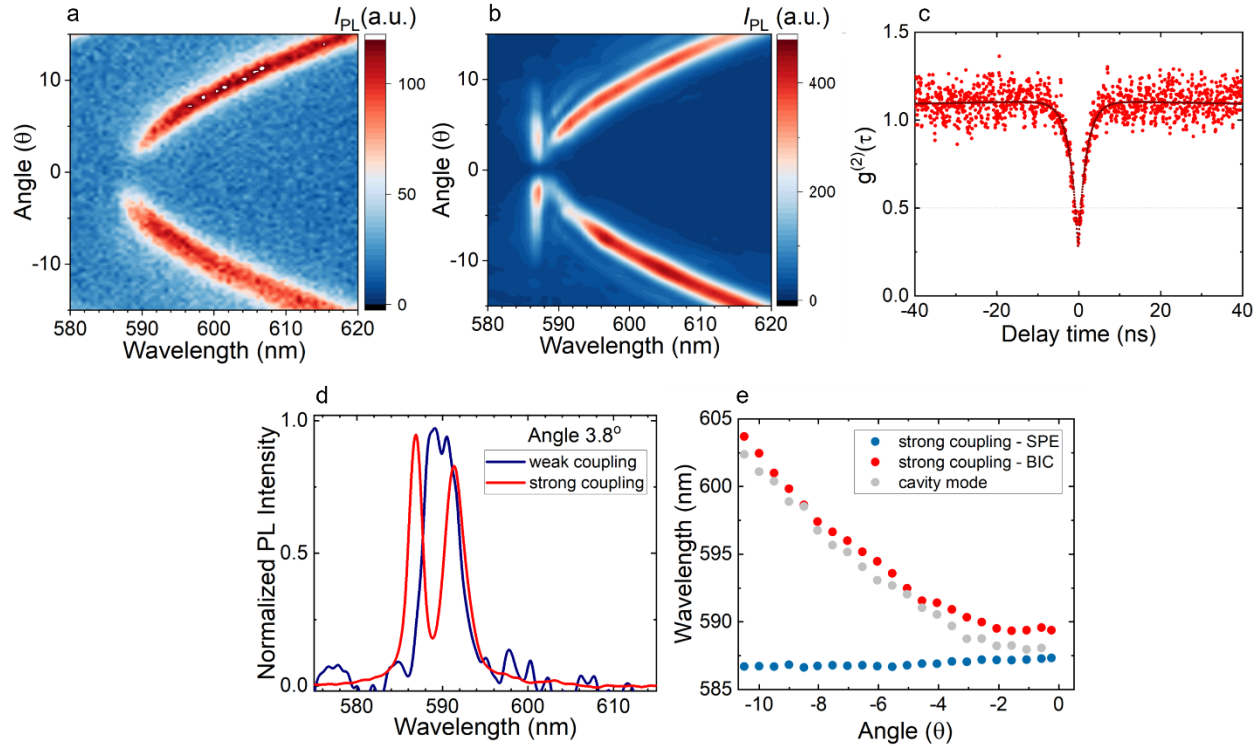
Figure 5.8. Coupling behavior of the native SPE and BIC cavity. *(a) Angle-resolved PL spectra resulted from weak coupling between the cavity and the hBN background emission. (b) Angle-resolved PL spectra in a strong coupling regime, showing a clear spectral splitting and vanishing emission at zero angle. (c) Antibunching dip g2(0) = 0.28 confirming the single-photon emission nature at the strong coupling spot shown in (b). (d) Normalized PL spectra extracted at 3.8° for the strong coupling case (red) and the weak coupling (blue). (e) Resonance wavelengths of SPE band (blue dots), BIC band (red dots) in a strong coupling regime and in a weak coupling with background emission (gray dots).*

By fitting the PL spectra to bi-Lorentzian and a single-Lorentzian function for strong and weak coupling cases, respectively, we extract the resonance energies of each band as a function of angle and plotted in Figure 5.8 e for SPE-band (blue dots), BIC-band (red dots) in strong coupling case and BIC mode (gray dots) for cavity mode. At small angles ($|\theta| <$ 4°), we observed a clear energy separation between the SPE and BIC bands, while the cavity mode in weak coupling case lies in between the split bands. At larger angles ($|\theta| >$

4°), the cavity modes in strong and weak coupling cases merge. This anti-crossing behavior is the clear indication of strong coupling between SPE and BIC, which only occurs near normal incidence at BIC position. Further away from BIC mode, only weak coupling with the continuum mode could be resolved. The characteristic Rabi splitting, defined as the energy splitting of two polariton bands at zero angle, is 7 meV in our case, which is more than an order of magnitude larger than that reported for coupled systems of single-dots and photonic crystals at cryogenic temperatures. [233, 234]

5.7. Conclusion

In conclusion, we have realized strong coupling between the native single-photon emitter in hBN film and photons by using bound-state-in-the-continuum concept. The strong coupling is proved by the absence of emission at normal incidence, the anti-crossing of the hybrid modes and the characteristic Rabi splitting of 7 meV. We expect that our findings will open a rich vein of research on manipulation of emission properties from single-photon emitters. Future work on the precise positioning of large-scale single-photon sources and the BIC cavity will allow for the study coherent light/matter interaction and the entanglement of two distinct sources that have important implications in quantum technologies such as quantum computing, quantum sensing and quantum information processing.

Chapter 6: IQP components fabricated from hexagonal boron nitride (hBN)

We previously demonstrate the possibility of integration of SPEs in hBN to the photonic devices in hybrid approach where the nanophotonics fabricated from a foreign material. In this chapter we attempt to fabricate hBN nanophotonics via monolithic approach through a high-resolution lithography and direct-writing techniques.

6.1. Introduction

Due to the advantages of using 2D van der Waals materials in hybrid integrated devices, these materials have been extensively studied for their peculiar optical and physical characteristics. Among 2D materials, hBN has emerged as a promising platform in the field of quantum nanophotonics due to its unique optical and physical properties including its hyperbolic nature with an anisotropic dielectric permittivity (birefringent). Moreover, band structure in hBN exhibits a wide direct band gap of about 6 eV which provides UV to IR transparency window allowing them to host a number of atomic point defects acting as quantum emitters even at room temperature. Integration of the quantum light source as the first and most basic element of IQPs with other components such as waveguides and cavities is a crucial step toward realizing integrated quantum photonic circuits. Initial results on integration of SPEs from hBN have been achieved via hybrid approach as we already explained in chapter 2. However, in such a hybrid approach, the quantum emitter cannot be localized into the electric field hotspot of the cavity and therefore spatial matching between the two systems is not satisfied. In this case, coupling efficiency is limited as the quantum emitter can only couple to the evanescent field of the cavity mode and as a result scattering loss is increased. In order to mitigate this issue which has a huge impact on the coupling efficiency, a monolithic system where the devices are fabricated from the parent material that hosts SPEs, is required for ideal on-chip devices. Since the optical properties of hBN meet the requirements for photonic devices, therefore, hBN nanophotonics can be fabricated through an entirely monolithic approach.[35, 100, 168] The advantage of such methods is that the quantum emitters can be positioned

within the electric field hotspot (high-energy field) of the photonic devices. Therefore, monolithic technique facilitates the spatial matching between the two systems and thus enables to achieve maximum coupling efficiency. However, in order for hBN to be used effectively as a monolithic platform for integrated circuits, robust fabrication techniques must be developed in order to realize high-quality nanophotonics components such as waveguides and cavities. This chapter shows fabrication processes for IQP components made from hexagonal boron nitride. In particular, we demonstrate fabrication processes of hBN waveguide as the main components of IQP. We then generate quantum emitters randomly via plasma method into waveguides, to demonstrate the possibility of using tapered waveguides to study emitter properties by photoluminescence excitation (PLE). Next, we demonstrate monolithic fabrication of BIC and 1D photonic crystal cavity (PCC) through the same method. This chapter describes a nanofabrication process that can be applied to the large-scale on chip nanophotonics with atomically thin hBN film.

6.2. Fabrication process

To realize monolithic IQP structures, we first focus on two different fabrication processes including lithography and direct-writing processes as shown in figure 6.1. To prepare the sample for the subsequent fabrication processes, hBN flakes were exfoliated from a bulk high quality hBN crystals using scotch tape method. Since the thickness of the flake plays a crucial role in the light confinement within the waveguide, flakes of ~ 200 nm were identified by optical contrast (further confirmed by AFM measurement) for the fabrication step. Next, the flake with suitable thickness were transferred on the edge of a precleaned thermal oxide (300 nm) SiO2 substrate via the pick-and-place method for the subsequent fabrication steps.
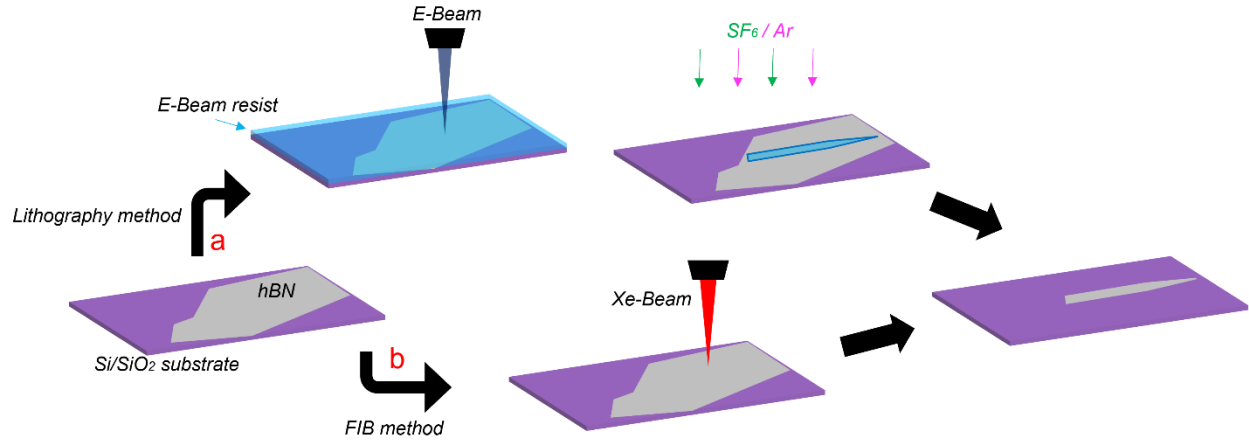
Figure 6.1. Schematic illustration of fabrication process. (a) lithography method and the subsequent RIE non-isotropic dry etching (b) direct-writing method using focused ion beam milling.

For the direct-writing method, we directly milled (physical etching) the waveguide patterns into the hBN flake. To achieve a high-resolution structure, we used Xe^+ beam of 30 KeV and 100 pA with 300 ns dwell time at each point. A major problem in any FIB process is the presence of ion beam tail [259] which give rise to a substantial etching around the site of interest as shown in figure 6.2. This arises from a Gaussian profile with a non-negligible ion current in the beam tail causing damages around the structure.
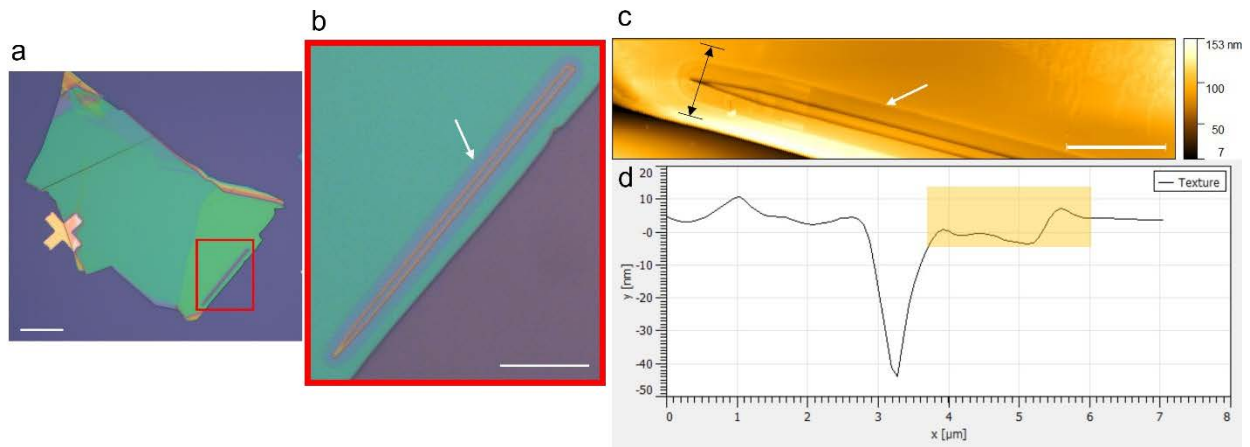
Figure 6.2. Illustration of Ion beam tail effect. (a) optical microscope of the fabricated hBN flake. Scale bar is 20 µm. (b) Magnified optical image outlined by the red square in (a). Scale bar is 10 µm. (c) AFM image of the fabricated tapered waveguide tapered waveguide. Scale bar corresponds to 10 µm (d) AFM profile of the fabricated hBN waveguide outlined by a black arrow in (c). The highlighted area shows the etched flake by the beam tail. The beam tail effect is indicated by a white arrow in (b) and (c).

To avoid the beam tailing effect and in turn blunt edges which has a huge impact of scattering loss, we deposit 100nm Cr onto the entire sample prior to milling process. Since the sputtering yield of the hBN is much higher compared to Cr, the metal mask was used to protect the underlying hBN flake from being affected by beam tail effect. Figure 6.3 a shows an array of tapered waveguides fabricated at the edge of substrate via FIB milling method. The same area was imaged by SEM as shown in figure 6.3 b. To study the effect of fabrication parameters on the final structure, the ion beam current was set to increase from the top to bottom waveguide. As the current changes the beam profile, the beam tail effect become more significant with higher current. This is directly visible by the shadow appeared around the waveguide for the bottom waveguide (highest current). Figure 6.3 c shows a magnified SEM image of the waveguide indicated by a green square in figure 6.3 b. The waveguide fabricated via FIB milling exhibits extremely smooth sidewall which minimizes optical loss caused by scattering. However, even at a low current, the beam tail effect still occurs, which severely damages the final structure. While using a low beam current can improve the resolution of the fabricated structures, it also prolongs the FIB milling process since huge amounts of material must be milled around the structures. The guiding properties of the fabricated waveguide can be visualized by focusing the laser onto the tapered part of the waveguide (532nm CW) from the side and monitoring by a CCD camera on top. Such an image captured by a CCD camera is shown in figure 6.3 d.
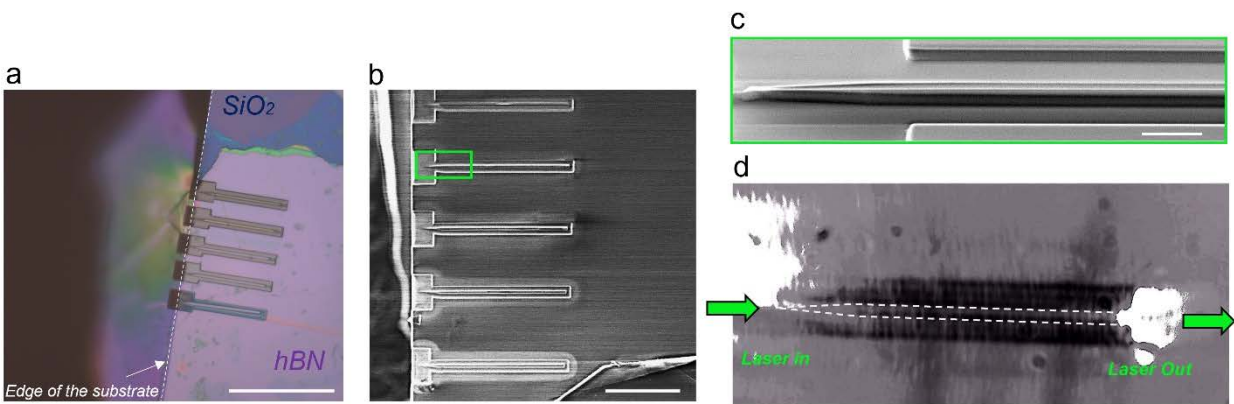
*Figure 6.3. Direct writing fabrication of tapered waveguides. (a) optical image of an array of tapered waveguides. Scale bar is 50 µm. (b) SEM image of the arrays shown in (a). scale bar corresponds to 20 µm. (c) magnified image of an individual waveguide outlined by a green rectangle in (b). (d) Wide-field image of laser coupled and guided by the tapered waveguide. The waveguide is outlined by dash line for clarity.*

The direct writing method can produce high resolution nanostructures with atomically smooth top and sidewall. However, this method requires further modification to avoid beam tail effect and to achieve better resolution. For example, using different source of ions such as Ga or other species or using different mask such as polymer can improve the resolution and minimize the detrimental effect caused by ion beam tail. As an alternative to FIB milling, we have also tried fabricating the same structures using lithography method, which is a scalable technique.

To this end, after the sample preparation step, a high-resolution e-beam resist was first spin coated onto the sample at 5000 rpm to form a 350 nm film followed by baking on a hotplate at 170°C for 2 minutes. Tapered waveguides were patterned onto the hBN flake via EBL technique with an electron energy and current of 30 keV and 20 pA, respectively. After the development step, a thin film of Cr was deposited on the substrate using a magnetron sputtering machine. Afterwards, the residual polymer was removed in hot resist remover and the remaining Cr was acting as a hard mask for the following step. The patterns were transferred into the underlying hBN flake using ICP/RIE technique with an SF6 and Ar mixed gas plasma at the chamber pressure of 10 mTorr. After etching, the Cr mask was removed by Cr etchant for 10 minutes at ~40 °C.

Figure 6.4 a and b illustrate the optical image of the patterned hBN flake prior to RIE step and post fabricated structures (after Cr removal step), respectively. The sample was etched for 40 seconds in a SF_6/Ar environment with the ratio of 1:2. Argon was deliberately added into the chamber to stabilize the plasma and to dilute SF_6 concentration. Figure 6.4 c shows a magnified SEM image of the waveguide arrays after fabrication processes. Due to extremely high etch selectivity of hBN (etch rate ~ 5 nm/s) in comparison to the Cr, a very thin Cr (~20 nm) was sufficient to act as a hard mask to etch over 200nm of hBN (figure 6.4 c -inset). However, the liftoff process leads to fabrication imperfections (indicated by yellow arrows in figure 6.4 c) as the sputtered metal appears on the sidewalls of the polymer, which is difficult to remove. In the case of nanoscale structures, this issue is more evident and might be addressed by a short sonication during the liftoff process. Magnified images of the post-fabricated structures indicate detailed structures of the tip and end of the waveguide as shown in figure 6.4 d

and e. To demonstrate the functionality, a green laser was coupled and guided by the waveguide as shown by the wide-field image in figure 6.4 f.
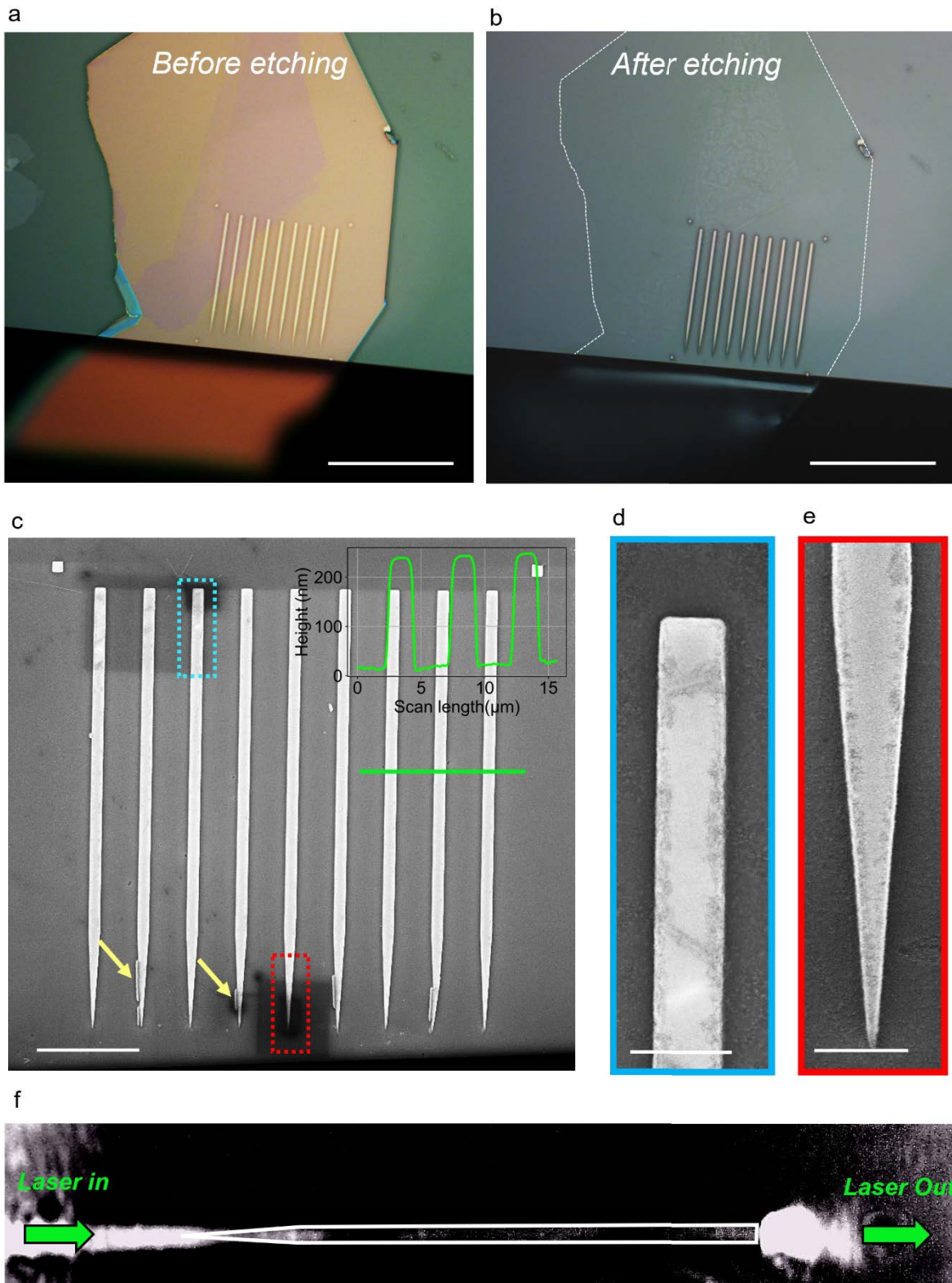
Figure 6.4. Fabrication of tapered waveguide at the edge of SiO₂ substrate via lithography method.
Optical image of the (a) prefabricated and (b) post fabricated structures. Scale bar corresponds to 50 µm.
(c) SEM image of the arrays of tapered waveguide. Inset- AFM line-scan profile of the waveguides indicated

by a green line. (d) and (e) are magnified image of the outlined section in (c). scale bar corresponds to 1 μm. (f) wide-field image of the laser coupled into the waveguide. The waveguide is outlined for clarity.

In the following, we created emitters through plasma method and then we characterize the emitter in room and cryogenic temperature by side excitation and top collection technique as shown in figure 6.5 a. The emitters were generated by a plasma post-treatment and annealing steps. [260] Specifically, the sample was placed into a plasma CVD reactor (microwave plasma CVD chamber, Seki-ASTeX AX5010) and a high microwave power (900W) was applied to ignite plasma at 60 Torr of hydrogen atmosphere for a short amount of time (3mins). Following the plasma treatment, the sample was annealed at 850°C in a tube furnace for 30 minutes. The short H_2 plasma treatment in combination with annealing was used to etch and clean the surface of hBN which reduces the background emission as well. Figure 6.5 b depicts the optical image of the waveguide arrays after plasma treatment. It is evident that the hBN waveguides were unaffected by the short hydrogen plasma. To identify the emitters created in the waveguide, we used a standard confocal PL mapping by top excitation and top collection configuration as shown in figure 6.5 c. A few emitters (as indicated by E1 to E8) were found on the waveguides in the confocal image for the subsequent PLE step. We attempt to carry out PLE measurement using the side excitation and top collection configuration to filter the excitation laser (shown in figure 6.5 a).
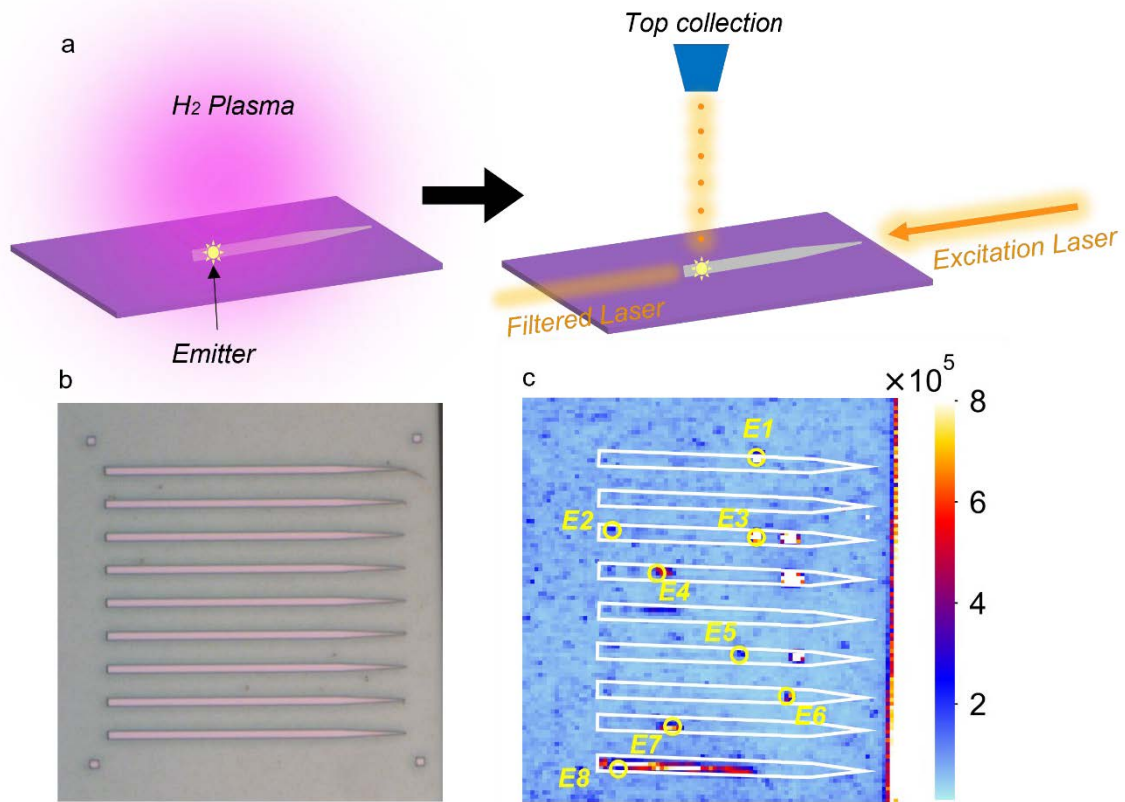
Figure 6.5. Generation and characterization method of the monolithically integrated emitters into the waveguides. *(a) schematic illustration of generation and characterization of the emitters. (b) optical image of the waveguide after plasma treatment. (c) confocal map of the waveguide array excited and collected from top. Different random emitters (E1-E8) were indicated by yellow circle in the pl map.*

Next, we characterized the emitters at room and cryogenic temperature for the PLE measurement. Figure 6.6 shows the PL spectra of the identified emitters (E1-E8) at room and cryogenic temperature. Although a few narrow emitters (shaded by pink rectangles) appeared after cooling down the sample but none of which was stable which is a key to proceed PLE measurement. We note that here, we presented the preliminary data as the measurement has not finalized yet and it requires more optimization in the fabrication, integration, and characterization step.
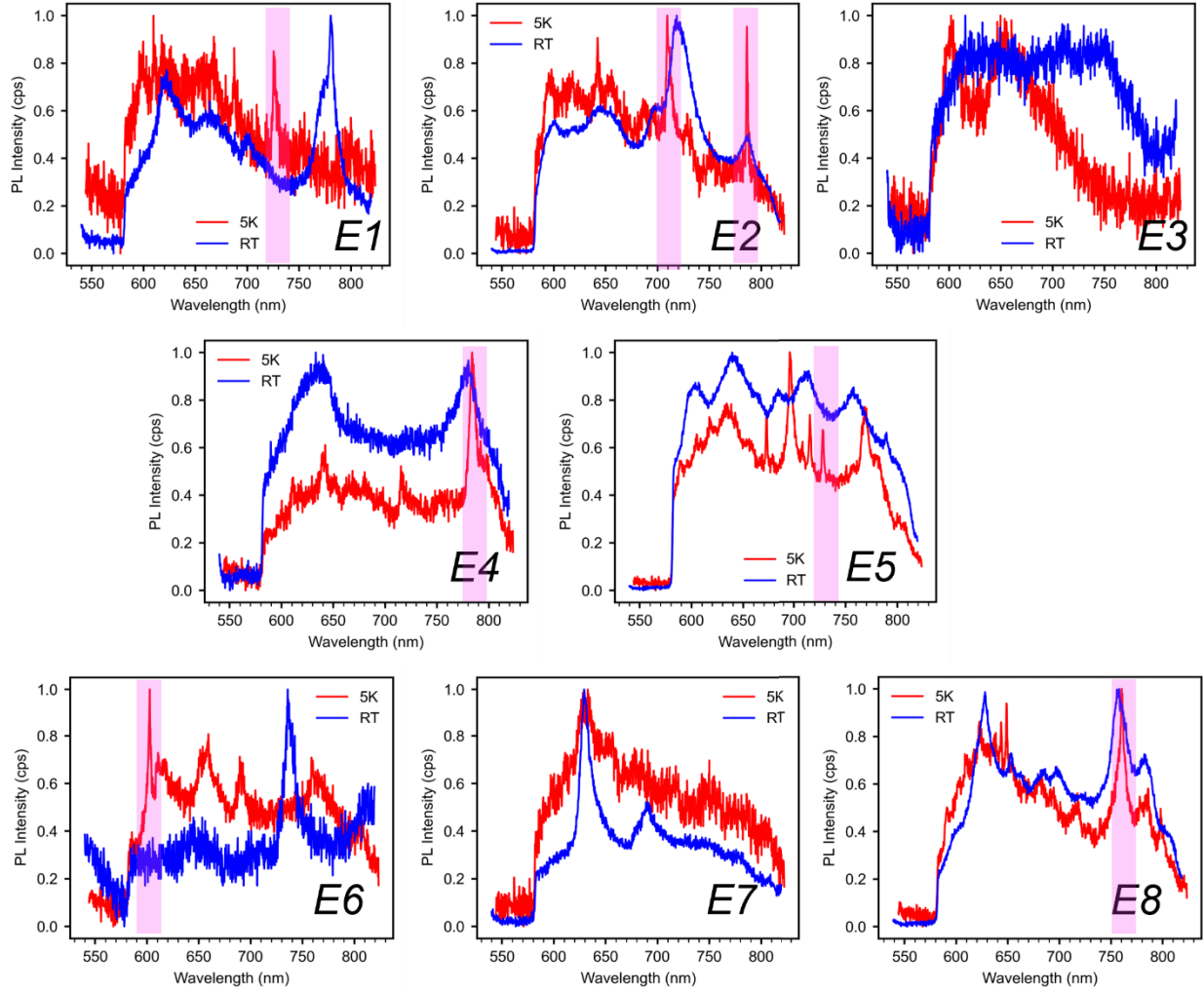
Figure 6.6. *PL spectra collected from the E1 to E8 at room (blue) and cryogenic temperature (red) using excitation laser power of 150 μW and collected for 10s.*

In this section, to showcase the capabilities of our fabrication method, we demonstrate further IQP components such as cavities fabricated through this approach. In order to achieve maximum resolution of the fabricated device, we skipped the liftoff process, and we employed a high-resolution resist as hard mask for the subsequent etching step. In this case, to maximize the resolution, we used a diluted e-beam resist which forms a very thin layer (~200 nm) of polymer on the flakes along with maximum e-beam energy (30KeV). We note that using a thin polymer resist, high e-beam energy, and low beam current result in a high-resolution pattern as they minimize the interaction volume of the electron beam. The interaction volume prevents vertical sidewall of the structure and is

less severe for high energy and thin polymer. Moreover, in a well-aligned SEM column, employing a low beam current results in a small spot which maximize the pattering resolution. Figure 6.7 illustrates high resolution lithography of various cavities with the above-mentioned recipe. The first column (figure 6.7 a, d and g) shows 2D photonic crystal cavity, BIC grids and 1D photonic crystal cavity, respectively.
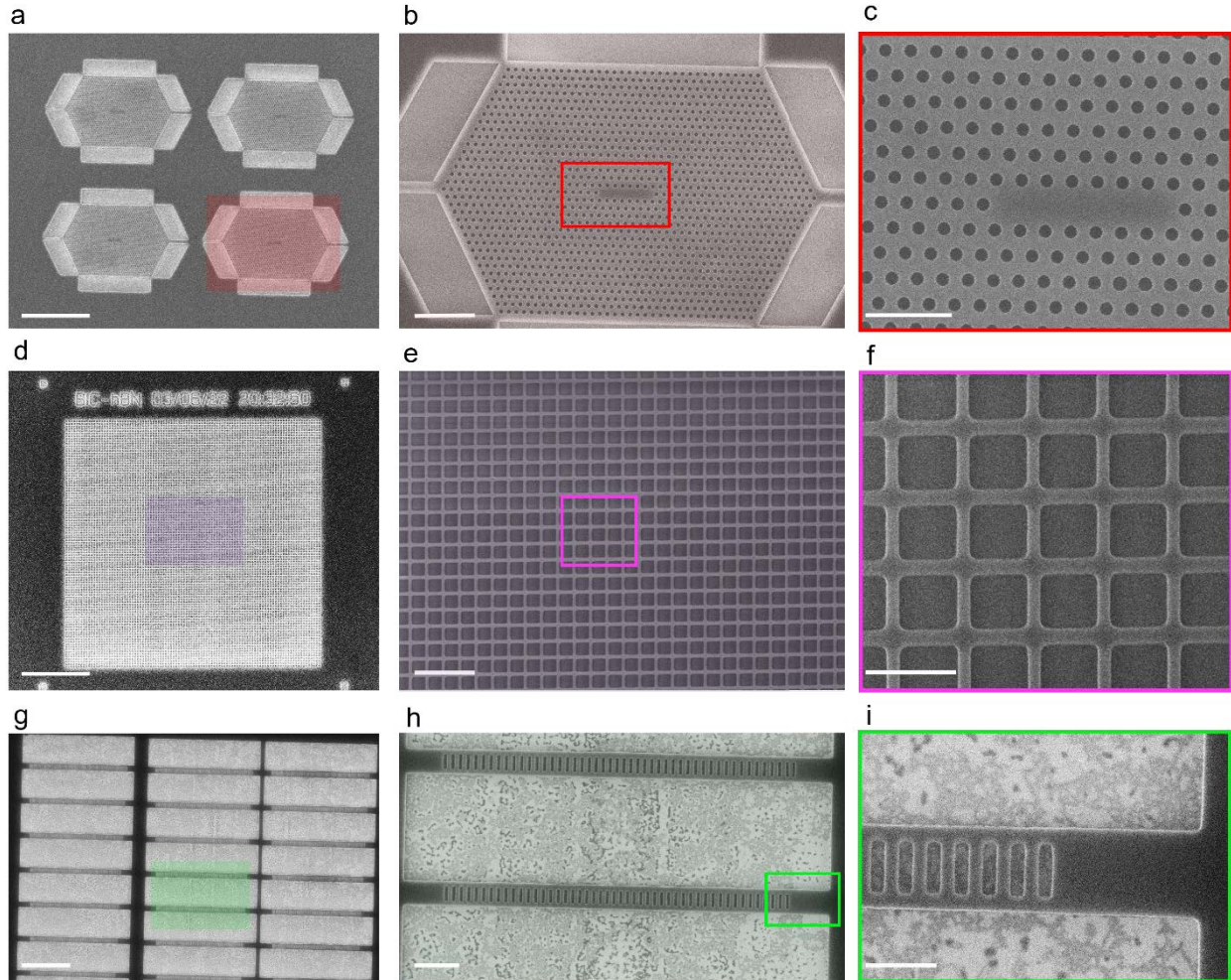
Figure 6.7. Cavity structures patterned on hBN flakes using EBL. SEM image of (a-c) a 2D photonic crystal cavity (d-f) a BIC periodic structure (g-i)1D photonic crystal cavities. Scale bar corresponds to (a) 10 µm (b) 2 µm (c) 1 µm (d) 10 µm (e) 2 µm (f) 500 nm (g) 5 µm (h) 1 µm (i) 500 nm. Images are magnified from left to right.

Next, we used the lithography patterns shown above as hard masks to transfer the patterns into the underlying hBN flake using SF$_6$/Ar gas mixture. Since this recipe skips

the mask lift-off process, the etching step can be carried out at the EBL resolution (as shown in figure 6.7) without any limitations imposed by metal masks. This results in fabrication of features down to a few tens of nanometers as shown in figure 6.8. For example, in the case of 1D PCC, the ladder-like structure (figure 6.8 c) or in BIC cavities (figure 6.8 f), the grids structures are fabricated with size of ~100 nm over an area of several micrometer through this recipe which is almost impossible via metal mask method. As shown in figure 6.8, after etching the sidewall appears vertical and well-resolved which shows the capabilities of this recipe for the monolithic structures. However, due to the high etch rate in the SF_6 environment, hBN can be laterally etched resulting in a rough top surface which is more evident for nanoscale structures. To avoid this problem, this recipe needs to be further optimized in case of etching parameters. For example, by lowering the SF_6 concentration which decreases the number of reactive species, the etching process can be carried out in a less harsh environment. Moreover, the directionality of the reactive species can be optimized by the bias power and/or chamber pressure.

As we previously mentioned, for better light confinement in the nanophotonic structures, it is necessary to maximize the refractive index contrast between cavity and the surrounding medium. However, hBN thin films may not be sticky enough to be subjected to a series of wet undercut steps in order to realize suspended structures. Alternatively, if a thin and freestanding hBN is needed, it may be possible to position hBN flake on a predefined trenched substrate using the pick-and-place method (Figure 6.9) prior to the fabrication steps. High RI contrast can be also achieved by using a lower refractive index substrate such as MgF_2 or CaF_2.
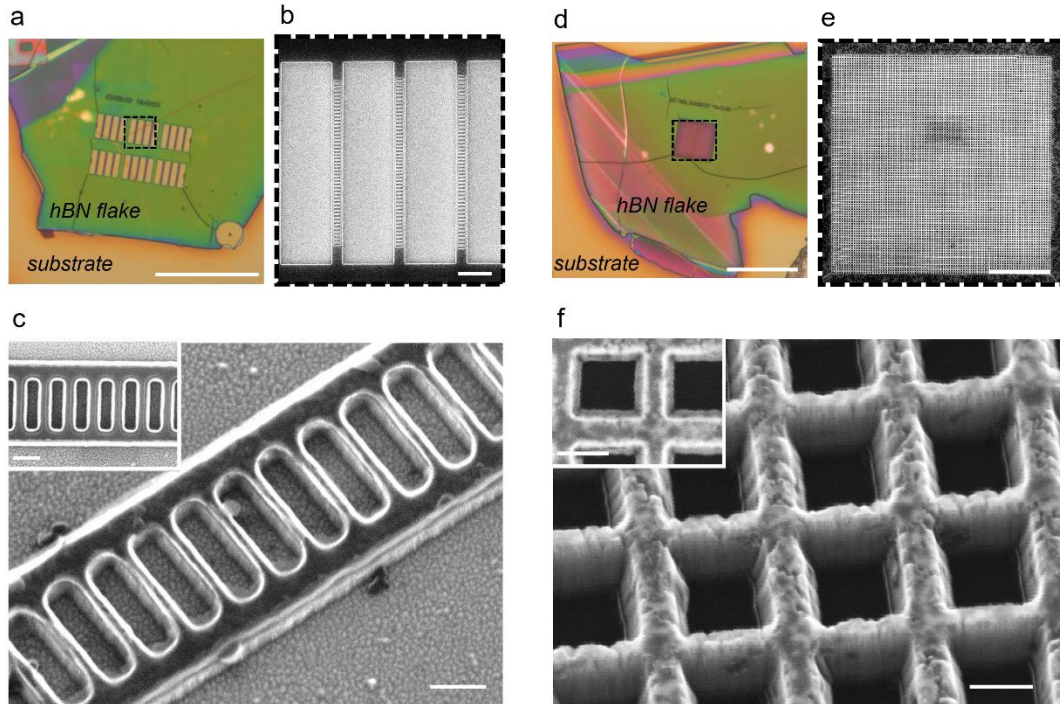
Figure 6.8. High resolution fabrication of hBN monolithic *(a-c) 1D photonic crystal cavity and (d-f) BIC grids. (a) optical image of post-fabricated 1D photonic crystal cavities. Scale bar is 50 μm. (b) SEM image of an array of 1D PCC cavities outlined in (a). Scale bar corresponds to 2 μm. (c) Tilted and magnified image of the 1D PCC shown in (b). Scale bar is 200 nm. The inset shows top view of the same 1D PCC, with a scale bar of 200nm. (d) optical image of the fabricated BIC grids on hBN. Scale bar corresponds to 50 μm. (e) SEM image of the outlined section in (d). Scale bar corresponds to 10 μm. (f) Tilted and magnified image of the device shown in (e). Scale bar is 200 nm. The inset illustrates top view of the same structure with a scale bar of 200nm.*
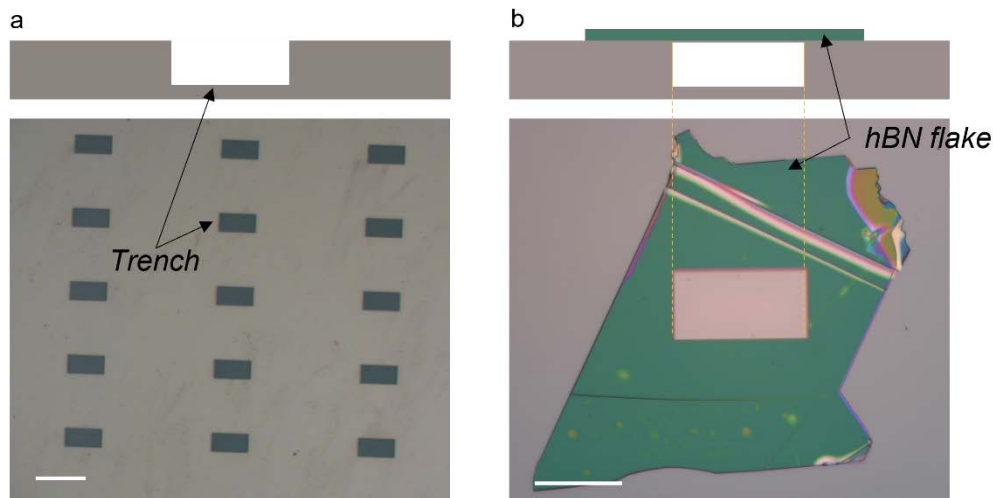
Figure 6.9. Preparation of suspended thin hBN flakes for the fabrication of high-Q cavities. *(a) Optical image of a trenched Silicon wafer. The schematic illustrates the side-view of the trench. Scale bar is 100*

µm. (b) optical image of an hBN flake placed on the trench using pick-and-place method. The schematic shows the side view of the freestanding hBN on the trench. Scale bar corresponds to 50 µm.

6.3. Conclusion

In this chapter, we demonstrate the capabilities of our fabrication method to directly pattern thin and small hBN flakes in a monolithic approach to explore the field of integrated hBN quantum photonics. We first attempt to fabricate tapered waveguide at the edge of substrate for the PLE experiments. After the fabrication, emitters were generated using hydrogen plasma method and then characterized at room and cryogenic temperature. Moreover, we also demonstrate the versatility of the fabrication process by showing a variety of IQP components including 1D and 2D PCC cavities, BIC grids etc. We detailed step-by-step fabrication procedure, the causes of fabrication artefacts we encountered during improvement of the technique and their possible solutions. Although, we successfully fabricated monolithic IQP components from hBN flakes, we emphasize that this project is on-going research and still requires further optimization in case of fabrication and integration steps.

Chapter 7: Conclusion and outlook

In this thesis, we have demonstrated the fabrication of several essential components of the integrated quantum photonics (IQP) through hybrid and monolithic approaches. The drawback and benefits of each fabrication techniques were highlighted, and the functionality of the fabrication techniques were examined through different characterization methods.

In more detail, in chapter 3, we introduced bottom-up fabrication scheme that is suitable for realization of a variety of monolithic diamond nanophotonics. Particularly, we demonstrate fabrication of an array of single crystal diamond nanopyramids from a polycrystalline substrate. In this method of fabrication, we first introduced patterned hard mask onto the polycrystalline diamond, and we overgrew the diamond using MPCVD method in the presence of germanium precursors. We discussed the possible mechanism of the growth through the restricted apertures and demonstrated controlled incorporation of the GeV centers into the photonic structures. To showcase the device functionality, we measured photoluminescence emission of the generated GeV centers at room and cryogenic temperature. We observed the emission enhancement of the GeV localized into the structures in comparison to the overgrown flat substrate. Furthermore, we identified a narrowband emitter with ~500 MHz linewidth at cryogenic temperature using resonant excitation (PLE) measurement. Finally, we showcase the possibility of the generation of single-photon emitter through this method by observing antibunching behavior from the emitters. Despite initial success in the generation of single photon sources through the patterned growth technique, the CVD method predominantly generates ensembles of emitters since the solid precursors are present throughout the entire process. Hence, to increase the probability of single defects, future effort should be put towards developing a CVD machine operating with different gaseous precursors such as germane [261] to introduce impurities for short pulses through a process called delta doping [262]. Besides, the bottom-up method can also be used for the fabrication of other structures such as photonic crystal cavities, which result in atomically smooth side walls and consequently an extremely high Q-factor. As the high Q-factor cavities require

suspended structures, this can be achieved through the patterned growth method on free-standing diamond membranes.

In the chapter 4, a method for hybrid integration of a spin defect in thin hBN flakes to a relatively high-Q cavity is introduced. Particularly, we demonstrate the fabrication method of a suspended hBN/TiO$_2$ ring resonator with a quality factor exceeding 2000. Boron vacancies (V_B^-) were deterministically generated on the hybrid structures using N$_2$ source FIB and functionality of the hybrid device were examined using a standard confocal microscope. Coupling of V_B^- to the whispering gallery modes of the cavity results in increase of photoluminescence about 7 and 3 in the unsaturation and saturation regimes, respectively. To demonstrate the coupling and guiding of spin-carrying photons into the ring resonator, we carried out ODMR measurement via two different excitation configurations. The local and non-local excitation scheme exhibited similar PL intensity and ODMR contrast indicating efficient coupling of the spin defect to the ring resonator. Although the subject of V_B^- level structure is currently the subject of a growing body of research, many fundamental aspects remain unknown. For example, there is no clear indication of zero phonon line in broad photoluminescence emission from V_B^- even at cryogenic temperatures, and the exact electronic level structure and emission dipole of V_B^- are still a mystery. Therefore, to reveal its unknown ZPL location, an extremely high Q-factor ring resonator with broad resonance and low mode volume is needed. The coupling of a broad resonance cavity with the relatively broad emission of this particular defect may facilitate the identification of a single boron vacancy defect. Therefore, the development of fabrication and characterization methods will undoubtedly lay the groundwork for future research in this direction.

Next, in the chapter 5, we studied hybrid integration of native quantum emitters in a CVD grown hBN film with TiO$_2$ nanopillars. The angle-resolved analysis revealed a dark state at zero angle of incident indicating the presence of symmetry-protected BIC mode which coincides with the same frequency as the native quantum emitters. The main rationale behind employing BIC mode was that the resonance persisted over entire nanopillar arrays and was not limited to a specific location. We transferred a few layer hBN film containing high density of quantum emitters onto the structures using the wet transfer

method. Next, we studied the coupling behavior of the emitter and BIC modes, and we successfully observed strong coupling between two systems. The strong coupling regime was confirmed by the absence of emission at normal incident, anti-crossing behavior and the characteristic Rabi splitting of 7 meV. The preliminary data of this project was presented, and still further experiment required to elaborate upon the strong coupling behavior such as detuning of the systems energy and quantum coherence measurement. Despite the observation of strong coupling in this project, the work suffers from inconsistency in the wavelength and location of the emitter. Thus, reproducibility of an efficient coupling requires predictable emission wavelengths and spatial location of the single photon source. According to recent research on native defects emitting at 590 nm, carbon appears to contribute to the defect. [77] Hence, future efforts should target the creation of predictable and site-specific hBN single emitters based on carbon implantation. In fact, the same approach was successful for diamond color centers by ion implantation leading to a number of groundbreaking works for cavity integrated color centers. [94, 263] Additionally, the integration of hBN with TiO_2 nanophotonics will provide higher field overlaps in photonic devices, leading to higher coupling efficiencies. This may be achievable for example by deposition of TiO_2 in two steps, before and after hBN transfer. In this case, hBN emitters are also better protected from interacting with their surrounding environment, and as a result, are less likely to experience charge transfers and field fluctuations.

In the last chapter, as a pathway for monolithic integration of SPEs, we demonstrated different fabrication technique to realize a set of common IQP components including waveguide and cavities. We first studied the fabrication of tapered waveguides via two different techniques namely, lithography and direct-writing method. Afterwards, the quantum emitters were generated via plasma treatment and annealing technique. We studied the integration of the emitters into the all-hBN tapered waveguide at room and cryogenic temperature using side excitation and top collection scheme. However, a full demonstration of the resonant excitation was not possible due to the instability of the emitters generated by plasma method which requires further experiments. Finally, we showcased the capabilities of the fabrication method by a variety of IQP components such as BIC grids and 1D PCC cavities which requires high-resolution fabrication technique.

Nevertheless, the availability of wafer-scale high quality hBN films with desired thickness is a major obstacle to on-chip fabrication of these monolithic integrated photonics. This problem may be overcome in the future through wafer scale growth of single crystal hBN.

All in all, in this thesis we explored a variety of fabrication techniques for the realization of hybrid and monolithic IQP components. We mainly focused on the fabrication and integration methods in order to develop potential application of SPEs integrated into on-chip nanophotonics.

Bibliography

1.   Aspect, A., P. Grangier, and G. Roger, *Experimental realization of Einstein-Podolsky-Rosen-Bohm Gedankenexperiment: a new violation of Bell's inequalities.* Physical review letters, 1982. **49**(2): p. 91.

2.   Breitenbach, G., S. Schiller, and J. Mlynek, *Measurement of the quantum states of squeezed light.* Nature, 1997. **387**(6632): p. 471-475.

3.   Kim, Y.-H., et al., *Delayed "choice" quantum eraser.* Physical Review Letters, 2000. **84**(1): p. 1.

4.   Aspect, A., *Bell's inequality test: more ideal than ever.* Nature, 1999. **398**(6724): p. 189-190.

5.   Gisin, N. and R. Thew, *Quantum communication.* Nature photonics, 2007. **1**(3): p. 165-171.

6.   Ladd, T.D., et al., *Quantum computers.* nature, 2010. **464**(7285): p. 45-53.

7.   Politi, A., et al., *Silica-on-silicon waveguide quantum circuits.* Science, 2008. **320**(5876): p. 646-649.

8.   Politi, A., J.C. Matthews, and J.L. O'brien, *Shor's quantum factoring algorithm on a photonic chip.* Science, 2009. **325**(5945): p. 1221-1221.

9.   Peruzzo, A., et al., *Quantum walks of correlated photons.* Science, 2010. **329**(5998): p. 1500-1503.

10.   Shadbolt, P.J., et al., *Generating, manipulating and measuring entanglement and mixture with a reconfigurable photonic circuit.* Nature Photonics, 2012. **6**(1): p. 45-49.

11.   Gerrits, T., et al., *On-chip, photon-number-resolving, telecommunication-band detectors for scalable photonic information processing.* Physical Review A, 2011. **84**(6): p. 060301.

12.   Pernice, W.H., et al., *High-speed and high-efficiency travelling wave single-photon detectors embedded in nanophotonic circuits.* Nature communications, 2012. **3**(1): p. 1-10.

13.   Bonneau, D., et al., *Quantum interference and manipulation of entanglement in silicon wire waveguide quantum circuits.* New Journal of Physics, 2012. **14**(4): p. 045003.

14.   Crespi, A., et al., *Integrated multimode interferometers with arbitrary designs for photonic boson sampling.* Nature photonics, 2013. **7**(7): p. 545-549.

15.   Sansoni, L., et al., *Two-particle bosonic-fermionic quantum walk via integrated photonics.* Physical review letters, 2012. **108**(1): p. 010502.

16.   He, Y.-M., et al., *On-demand semiconductor single-photon source with near-unity indistinguishability.* Nature nanotechnology, 2013. **8**(3): p. 213-217.

17.   Silverstone, J.W., et al., *On-chip quantum interference between silicon photon-pair sources.* Nature Photonics, 2014. **8**(2): p. 104-108.

18.   Arcari, M., et al., *Near-unity coupling efficiency of a quantum emitter to a photonic crystal waveguide.* Physical review letters, 2014. **113**(9): p. 093603.

19.   Peruzzo, A., et al., *A variational eigenvalue solver on a photonic quantum processor.* Nature communications, 2014. **5**(1): p. 1-7.

20. Sibson, P., et al., *Chip-based quantum key distribution.* Nature communications, 2017. **8**(1): p. 1-6.
21. Carolan, J., et al., *Universal linear optics.* Science, 2015. **349**(6249): p. 711-716.
22. Spring, J.B., et al., *Chip-based array of near-identical, pure, heralded single-photon sources.* Optica, 2017. **4**(1): p. 90-96.
23. Bentivegna, M., et al., *Experimental scattershot boson sampling.* Science advances, 2015. **1**(3): p. e1400255.
24. Ciampini, M.A., et al., *Path-polarization hyperentangled and cluster states of photons on a chip.* Light: Science & Applications, 2016. **5**(4): p. e16064-e16064.
25. Wang, H., et al., *High-efficiency multiphoton boson sampling.* Nature Photonics, 2017. **11**(6): p. 361-365.
26. Wang, J., et al., *Experimental quantum Hamiltonian learning.* Nature Physics, 2017. **13**(6): p. 551-555.
27. Wang, J., et al., *Multidimensional quantum entanglement with large-scale integrated optics.* Science, 2018. **360**(6386): p. 285-291.
28. Sparrow, C., et al., *Simulating the vibrational quantum dynamics of molecules using photonics.* Nature, 2018. **557**(7707): p. 660-667.
29. Harrow, A.W. and A. Montanaro, *Quantum computational supremacy.* Nature, 2017. **549**(7671): p. 203-209.
30. Wang, J., et al., *Integrated photonic quantum technologies.* Nature Photonics, 2020. **14**(5): p. 273-284.
31. Kim, J.-H., et al., *Hybrid integration methods for on-chip quantum photonics.* Optica, 2020. **7**(4): p. 291-308.
32. Aghaeimeibodi, S., et al., *Integration of quantum dots with lithium niobate photonics.* Applied Physics Letters, 2018. **113**(22): p. 221102.
33. Rengstl, U., et al., *On-chip beamsplitter operation on single photons from quasi-resonantly excited quantum dots embedded in GaAs rib waveguides.* Applied Physics Letters, 2015. **107**(2): p. 021101.
34. Davanco, M., et al., *Heterogeneous integration for on-chip quantum photonic circuits with single quantum dot devices.* Nature communications, 2017. **8**(1): p. 1-12.
35. Kim, S., et al., *Photonic crystal cavities from hexagonal boron nitride.* Nature communications, 2018. **9**(1): p. 1-8.
36. Uppu, R., et al., *On-chip deterministic operation of quantum dots in dual-mode waveguides for a plug-and-play single-photon source.* Nature communications, 2020. **11**(1): p. 1-6.
37. Gyger, S., et al., *Reconfigurable photonics with on-chip single-photon detectors.* Nature communications, 2021. **12**(1): p. 1-8.
38. Bogdanov, S., et al., *Material platforms for integrated quantum photonics.* Optical Materials Express, 2017. **7**(1): p. 111-132.
39. Shotan, Z., et al., *Photoinduced modification of single-photon emitters in hexagonal boron nitride.* Acs Photonics, 2016. **3**(12): p. 2490-2496.
40. White, S., et al., *Phonon dephasing and spectral diffusion of quantum emitters in hexagonal boron nitride.* Optica, 2021. **8**(9): p. 1153-1158.
41. Lounis, B. and M. Orrit, *Single-photon sources.* Reports on Progress in Physics, 2005. **68**(5): p. 1129.

42.   Couteau, C., *Spontaneous parametric down-conversion.* Contemporary Physics, 2018. **59**(3): p. 291-304.

43.   Kwiat, P.G., et al., *New high-intensity source of polarization-entangled photon pairs.* Physical Review Letters, 1995. **75**(24): p. 4337.

44.   Jennewein, T., et al., *Quantum cryptography with entangled photons.* Physical review letters, 2000. **84**(20): p. 4729.

45.   Yin, J., et al., *Entanglement-based secure quantum cryptography over 1,120 kilometres.* Nature, 2020. **582**(7813): p. 501-505.

46.   Adachi, Y., et al., *Simple and efficient quantum key distribution with parametric down-conversion.* Physical review letters, 2007. **99**(18): p. 180503.

47.   Guo, X., et al., *Parametric down-conversion photon-pair source on a nanophotonic chip.* Light: Science & Applications, 2017. **6**(5): p. e16249-e16249.

48.   Senellart, P., G. Solomon, and A. White, *High-performance semiconductor quantum-dot single-photon sources.* Nature nanotechnology, 2017. **12**(11): p. 1026-1039.

49.   Kimble, H.J., M. Dagenais, and L. Mandel, *Photon antibunching in resonance fluorescence.* Physical Review Letters, 1977. **39**(11): p. 691.

50.   García-Ripoll, J.J., P. Zoller, and J.I. Cirac, *Quantum information processing with cold atoms and trapped ions.* Journal of Physics B: Atomic, Molecular and Optical Physics, 2005. **38**(9): p. S567.

51.   Niffenegger, R.J., et al., *Integrated multi-wavelength control of an ion qubit.* Nature, 2020. **586**(7830): p. 538-542.

52.   Samutpraphoot, P., et al., *Strong coupling of two individually controlled atoms via a nanophotonic cavity.* Physical review letters, 2020. **124**(6): p. 063602.

53.   Colombe, Y., et al., *Strong atom–field coupling for Bose–Einstein condensates in an optical cavity on a chip.* Nature, 2007. **450**(7167): p. 272-276.

54.   Liu, X. and M.C. Hersam, *2D materials for quantum information science.* Nature Reviews Materials, 2019. **4**(10): p. 669-684.

55.   Awschalom, D.D., et al., *Quantum technologies with optically interfaced solid-state spins.* Nature Photonics, 2018. **12**(9): p. 516-527.

56.   Aharonovich, I., D. Englund, and M. Toth, *Solid-state single-photon emitters.* Nature Photonics, 2016. **10**(10): p. 631-641.

57.   Atatüre, M., et al., *Material platforms for spin-based photonic quantum technologies.* Nature Reviews Materials, 2018. **3**(5): p. 38-51.

58.   Bassett, L.C., et al., *Quantum defects by design.* Nanophotonics, 2019. **8**(11): p. 1867-1888.

59.   Park, Y.-S., et al., *Room temperature single-photon emission from individual perovskite quantum dots.* ACS nano, 2015. **9**(10): p. 10386-10393.

60.   Tran, T.T., et al., *Quantum emission from hexagonal boron nitride monolayers.* Nature nanotechnology, 2016. **11**(1): p. 37-41.

61.   He, X., et al., *Tunable room-temperature single-photon emission at telecom wavelengths from sp3 defects in carbon nanotubes.* Nature Photonics, 2017. **11**(9): p. 577-582.

62.   Palacios-Berraquero, C., et al., *Large-scale quantum-emitter arrays in atomically thin semiconductors.* Nature communications, 2017. **8**(1): p. 1-6.

63. Zhang, G., et al., *Material platforms for defect qubits and single-photon emitters.* Applied Physics Reviews, 2020. **7**(3): p. 031308.

64. Hepp, S., et al., *Semiconductor quantum dots for integrated quantum photonics.* Advanced Quantum Technologies, 2019. **2**(9): p. 1900020.

65. Seravalli, L. and F. Sacconi, *Reviewing quantum dots for single-photon emission at 1.55 μm: a quantitative comparison of materials.* Journal of Physics: Materials, 2020. **3**(4): p. 042005.

66. Weber, J., et al., *Quantum computing with defects.* Proceedings of the National Academy of Sciences, 2010. **107**(19): p. 8513-8518.

67. Awschalom, D.D., et al., *Quantum spintronics: engineering and manipulating atom-like spins in semiconductors.* Science, 2013. **339**(6124): p. 1174-1179.

68. Aharonovich, I., et al., *Diamond-based single-photon emitters.* Reports on progress in Physics, 2011. **74**(7): p. 076501.

69. Bradac, C., et al., *Quantum nanophotonics with group IV defects in diamond.* Nature communications, 2019. **10**(1): p. 1-13.

70. Lohrmann, A., et al., *A review on single photon sources in silicon carbide.* Reports on Progress in Physics, 2017. **80**(3): p. 034502.

71. Castelletto, S., et al., *A silicon carbide room-temperature single-photon source.* Nature materials, 2014. **13**(2): p. 151-156.

72. Siyushev, P., et al., *Coherent properties of single rare-earth spin qubits.* Nature communications, 2014. **5**(1): p. 1-6.

73. Zhong, T. and P. Goldner, *Emerging rare-earth doped material platforms for quantum nanophotonics.* Nanophotonics, 2019. **8**(11): p. 2003-2015.

74. Kianinia, M., et al., *Quantum emitters in 2D materials: Emitter engineering, photophysics, and integration in photonic nanostructures.* Applied Physics Reviews, 2022. **9**(1): p. 011306.

75. Toth, M. and I. Aharonovich, *Single photon sources in atomically thin materials.* Annual review of physical chemistry, 2019. **70**: p. 123-142.

76. He, X., et al., *Carbon nanotubes as emerging quantum-light sources.* Nature materials, 2018. **17**(8): p. 663-670.

77. Mendelson, N., et al., *Identifying carbon as the source of visible single-photon emission from hexagonal boron nitride.* Nature materials, 2021. **20**(3): p. 321-328.

78. Fournier, C., et al., *Position-controlled quantum emitters with reproducible emission wavelength in hexagonal boron nitride.* Nature communications, 2021. **12**(1): p. 1-6.

79. Ziegler, J., et al., *Deterministic quantum emitter formation in hexagonal boron nitride via controlled edge creation.* Nano letters, 2019. **19**(3): p. 2121-2127.

80. Lyu, C., et al., *Single-photon emission from two-dimensional hexagonal boron nitride annealed in a carbon-rich environment.* Applied Physics Letters, 2020. **117**(24): p. 244002.

81. Gao, X., et al., *Femtosecond laser writing of spin defects in hexagonal boron nitride.* ACS Photonics, 2021. **8**(4): p. 994-1000.

82. Xu, X., et al., *Creating quantum emitters in hexagonal boron nitride deterministically on chip-compatible substrates.* Nano Letters, 2021. **21**(19): p. 8182-8189.

83.   He, Y.-M., et al., *Single quantum emitters in monolayer semiconductors.* Nature nanotechnology, 2015. **10**(6): p. 497-502.

84.   Tonndorf, P., et al., *Single-photon emission from localized excitons in an atomically thin semiconductor.* Optica, 2015. **2**(4): p. 347-352.

85.   Koperski, M., et al., *Single photon emitters in exfoliated WSe 2 structures.* Nature nanotechnology, 2015. **10**(6): p. 503-506.

86.   Srivastava, A., et al., *Optically active quantum dots in monolayer WSe2.* Nature nanotechnology, 2015. **10**(6): p. 491-496.

87.   Klein, J., et al., *Site-selectively generated photon emitters in monolayer MoS2 via local helium ion irradiation.* Nature communications, 2019. **10**(1): p. 1-8.

88.   Ma, X., et al., *Room-temperature single-photon generation from solitary dopants of carbon nanotubes.* Nature nanotechnology, 2015. **10**(8): p. 671-675.

89.   Hofmann, M.S., et al., *Bright, long-lived and coherent excitons in carbon nanotube quantum dots.* Nature nanotechnology, 2013. **8**(7): p. 502-505.

90.   Högele, A., et al., *Photon antibunching in the photoluminescence spectra of a single carbon nanotube.* Physical review letters, 2008. **100**(21): p. 217401.

91.   Saha, A., et al., *Narrow-band single-photon emission through selective aryl functionalization of zigzag carbon nanotubes.* Nature Chemistry, 2018. **10**(11): p. 1089-1095.

92.   Pezzagna, S., et al., *Nanoscale engineering and optical addressing of single spins in diamond.* small, 2010. **6**(19): p. 2117-2121.

93.   Lesik, M., et al., *Maskless and targeted creation of arrays of colour centres in diamond using focused ion beam technology.* physica status solidi (a), 2013. **210**(10): p. 2055-2059.

94.   Schröder, T., et al., *Scalable focused ion beam creation of nearly lifetime-limited single quantum emitters in diamond nanostructures.* Nature communications, 2017. **8**(1): p. 1-7.

95.   Aharonovich, I., et al., *Bottom-up engineering of diamond micro-and nano-structures.* Laser & Photonics Reviews, 2013. **7**(5): p. L61-L65.

96.   Lenzini, F., et al., *Diamond as a platform for integrated quantum photonics.* Advanced Quantum Technologies, 2018. **1**(3): p. 1800061.

97.   Castelletto, S., et al., *Advances in diamond nanofabrication for ultrasensitive devices.* Microsystems & nanoengineering, 2017. **3**(1): p. 1-16.

98.   Babin, C., et al., *Fabrication and nanophotonic waveguide integration of silicon carbide colour centres with preserved spin-optical coherence.* Nature materials, 2022. **21**(1): p. 67-73.

99.   Lukin, D.M., M.A. Guidry, and J. Vučković, *Integrated quantum photonics with silicon carbide: Challenges and prospects.* PRX Quantum, 2020. **1**(2): p. 020102.

100.   Fröch, J.E., et al., *Photonic nanostructures from hexagonal boron nitride.* Advanced Optical Materials, 2019. **7**(4): p. 1801344.

101.   Froch, J.E., et al., *Coupling Spin Defects in Hexagonal Boron Nitride to Monolithic Bullseye Cavities.* Nano Lett, 2021. **21**(15): p. 6549-6555.

102.   Caldwell, J.D., et al., *Photonics with hexagonal boron nitride.* Nature Reviews Materials, 2019. **4**(8): p. 552-567.

103.   Fröch, J.E., et al., *Purcell Enhancement of a Cavity-Coupled Emitter in Hexagonal Boron Nitride.* Small, 2022. **18**(2): p. 2104805.

104. Blumenthal, D.J., et al., *Silicon nitride in silicon photonics.* Proceedings of the IEEE, 2018. **106**(12): p. 2209-2231.

105. Senichev, A., et al., *Silicon nitride waveguides with intrinsic single-photon emitters for integrated quantum photonics.* arXiv preprint arXiv:2205.08481, 2022.

106. Silverstone, J.W., et al. *Silicon quantum photonics.* in *2016 International Conference on Optical MEMS and Nanophotonics (OMN).* 2016. IEEE.

107. Feng, L.T., G.C. Guo, and X.F. Ren, *Progress on integrated quantum photonic sources with silicon.* Advanced Quantum Technologies, 2020. **3**(2): p. 1900058.

108. Wolters, J., et al., *Enhancement of the zero phonon line emission from a single nitrogen vacancy center in a nanodiamond via coupling to a photonic crystal cavity.* Applied Physics Letters, 2010. **97**(14): p. 141108.

109. Barclay, P.E., et al., *Coherent interference effects in a nano-assembled diamond NV center cavity-QED system.* Optics Express, 2009. **17**(10): p. 8081-8197.

110. Butcher, A., et al., *High-Q nanophotonic resonators on diamond membranes using templated atomic layer deposition of TiO2.* Nano Letters, 2020. **20**(6): p. 4603-4609.

111. Fryett, T.K., et al., *Encapsulated silicon nitride nanobeam cavity for hybrid nanophotonics.* ACS Photonics, 2018. **5**(6): p. 2176-2181.

112. Peyskens, F., et al., *Integration of single photon emitters in 2D layered materials with a silicon nitride photonic chip.* Nature communications, 2019. **10**(1): p. 1-7.

113. Zadeh, I.E., et al., *Deterministic integration of single photon sources in silicon based photonic circuits.* Nano Letters, 2016. **16**(4): p. 2289-2294.

114. Das, A., et al., *Demonstration of hybrid high-Q hexagonal boron nitride microresonators.* ACS Photonics, 2021. **8**(10): p. 3027-3033.

115. Yang, Z., et al., *A room temperature continuous-wave nanolaser using colloidal quantum wells.* Nature communications, 2017. **8**(1): p. 1-8.

116. Santori, C., et al., *Nanophotonics for quantum optics using nitrogen-vacancy centers in diamond.* Nanotechnology, 2010. **21**(27): p. 274008.

117. Hoang, T.B., G.M. Akselrod, and M.H. Mikkelsen, *Ultrafast room-temperature single photon emission from quantum dots coupled to plasmonic nanocavities.* Nano letters, 2016. **16**(1): p. 270-275.

118. Kumar, S., et al., *Generation and controlled routing of single plasmons on a chip.* Nano letters, 2014. **14**(2): p. 663-669.

119. Santhosh, K., et al., *Vacuum Rabi splitting in a plasmonic cavity at the single quantum emitter limit.* Nature communications, 2016. **7**(1): p. 1-5.

120. Böhm, F., et al., *On-chip integration of single solid-state quantum emitters with a SiO2 photonic platform.* New Journal of Physics, 2019. **21**(4): p. 045007.

121. Chen, Y., et al., *Deterministic positioning of colloidal quantum dots on silicon nitride nanobeam cavities.* Nano letters, 2018. **18**(10): p. 6404-6410.

122. Schell, A.W., et al., *Three-dimensional quantum photonic elements based on single nitrogen vacancy-centres in laser-written microstructures.* Scientific reports, 2013. **3**(1): p. 1-5.

123. Luo, Y., et al., *Deterministic coupling of site-controlled quantum emitters in monolayer WSe2 to plasmonic nanocavities.* Nature nanotechnology, 2018. **13**(12): p. 1137-1142.

124. Li, G., et al., *TiO 2 microring resonators with high Q and compact footprint fabricated by a bottom-up method.* Optics Letters, 2020. **45**(18): p. 5012-5015.
125. Choy, J.T., et al., *Enhanced single-photon emission from a diamond–silver aperture.* Nature Photonics, 2011. **5**(12): p. 738-743.
126. Li, X., et al., *Photonic trimming of quantum emitters via direct fabrication of metallic nanofeatures.* APL Photonics, 2018. **3**(7): p. 071301.
127. Ciancico, C., et al., *Narrow line width quantum emitters in an electron-beam-shaped polymer.* ACS Photonics, 2019. **6**(12): p. 3120-3125.
128. Shi, Q., et al., *Wiring up pre-characterized single-photon emitters by laser lithography.* Scientific reports, 2016. **6**(1): p. 1-7.
129. Li, C., et al., *Scalable and deterministic fabrication of quantum emitter arrays from hexagonal boron nitride.* Nano Letters, 2021. **21**(8): p. 3626-3632.
130. Zhang, J.L., et al., *Hybrid group IV nanophotonic structures incorporating diamond silicon-vacancy color centers.* Nano letters, 2016. **16**(1): p. 212-217.
131. Kunert, B., et al., *How to control defect formation in monolithic III/V hetero-epitaxy on (100) Si? A critical review on current approaches.* Semiconductor Science and Technology, 2018. **33**(9): p. 093002.
132. Wang, Z., et al., *Novel light source integration approaches for silicon photonics.* Laser & Photonics Reviews, 2017. **11**(4): p. 1700063.
133. Pan, S., et al., *Recent progress in epitaxial growth of III–V quantum-dot lasers on silicon substrate.* Journal of Semiconductors, 2019. **40**(10): p. 101302.
134. Arend, C., et al., *Site selective growth of heteroepitaxial diamond nanoislands containing single SiV centers.* Applied Physics Letters, 2016. **108**(6): p. 063111.
135. Sortino, L., et al., *Bright single photon emitters with enhanced quantum efficiency in a two-dimensional semiconductor coupled with dielectric nano-antennas.* Nature Communications, 2021. **12**(1): p. 1-9.
136. McPhillimy, J., et al., *Automated nanoscale absolute accuracy alignment system for transfer printing.* ACS applied nano materials, 2020. **3**(10): p. 10326-10332.
137. Jevtics, D., et al., *Spatially dense integration of micron-scale devices from multiple materials on a single chip via transfer-printing.* Optical Materials Express, 2021. **11**(10): p. 3567-3576.
138. Proscia, N.V., et al., *Near-deterministic activation of room-temperature quantum emitters in hexagonal boron nitride.* Optica, 2018. **5**(9): p. 1128-1134.
139. Caldwell, J.D., et al., *Photonics with hexagonal boron nitride.* Nature Reviews Materials, 2019. **4**(8): p. 552-567.
140. Maiti, R., et al., *A semi-empirical integrated microring cavity approach for 2D material optical index identification at 1.55 µm.* Nanophotonics, 2019. **8**(3): p. 435-441.
141. Rivera, P., et al., *Coupling of photonic crystal cavity and interlayer exciton in heterobilayer of transition metal dichalcogenides.* 2D Materials, 2019. **7**(1): p. 015027.
142. Elshaari, A.W., et al., *On-chip single photon filtering and multiplexing in hybrid quantum photonic circuits.* Nature communications, 2017. **8**(1): p. 1-8.
143. Najafi, F., et al., *On-chip detection of non-classical light by scalable integration of single-photon detectors.* Nature communications, 2015. **6**(1): p. 1-8.

144. Komissarenko, F., et al., *Manipulation Technique for Precise Transfer of Single Perovskite Nanoparticles.* Nanomaterials, 2020. **10**(7): p. 1306.
145. Loudon, R., *The quantum theory of light.* 2000: OUP Oxford.
146. Hunger, D., et al., *A fiber Fabry–Perot cavity with high finesse.* New Journal of Physics, 2010. **12**(6): p. 065038.
147. Lalanne, P., C. Sauvan, and J.P. Hugonin, *Photon confinement in photonic crystal nanocavities.* Laser & Photonics Reviews, 2008. **2**(6): p. 514-526.
148. Fox, A.M. and M. Fox, *Quantum optics: an introduction.* Vol. 15. 2006: Oxford university press.
149. Merzbacher, E., *Quantum mechanics.* 1961: Jones & Bartlett Publishers.
150. Haroche, S. and J.-M. Raimond, *Cavity quantum electrodynamics.* Scientific American, 1993. **268**(4): p. 54-62.
151. Purcell, E.M., H.C. Torrey, and R.V. Pound, *Resonance absorption by nuclear magnetic moments in a solid.* Physical review, 1946. **69**(1-2): p. 37.
152. Purcell, E.M., *Spontaneous emission probabilities at radio frequencies*, in *Confined electrons and photons*. 1995, Springer. p. 839-839.
153. Jaynes, E.T. and F.W. Cummings, *Comparison of quantum and semiclassical radiation theories with application to the beam maser.* Proceedings of the IEEE, 1963. **51**(1): p. 89-109.
154. Scofield, A.C., et al., *Bottom-up photonic crystal cavities formed by patterned III–V nanopillars.* Nano letters, 2011. **11**(6): p. 2242-2246.
155. von Freymann, G., et al., *Bottom-up assembly of photonic crystals.* Chemical Society Reviews, 2013. **42**(7): p. 2528-2554.
156. Behroudj, A., D. Geiger, and S. Strehle, *Epitaxial bottom-up growth of silicon nanowires on oxidized silicon by alloy-catalyzed gas-phase synthesis.* Nano Letters, 2019. **19**(11): p. 7895-7900.
157. Prieto, I., et al., *High quality factor GaAs-based photonic crystal microcavities by epitaxial re-growth.* Optics Express, 2013. **21**(25): p. 31615-31622.
158. Sovyk, D., et al., *Fabrication of diamond microstub photoemitters with strong photoluminescence of SiV color centers: bottom-up approach.* Applied Physics A, 2015. **118**(1): p. 17-21.
159. Blanco, A., et al., *Large-scale synthesis of a silicon photonic crystal with a complete three-dimensional bandgap near 1.5 micrometres.* Nature, 2000. **405**(6785): p. 437-440.
160. Santori, C., et al., *Indistinguishable photons from a single-photon device.* nature, 2002. **419**(6907): p. 594-597.
161. Washiyama, S., et al., *Coalescence of epitaxial lateral overgrowth-diamond on stripe-patterned nucleation on Ir/MgO (001).* Applied physics express, 2011. **4**(9): p. 095502.
162. Holmes, M.J., et al., *Room-temperature triggered single photon emission from a III-nitride site-controlled nanowire quantum dot.* Nano letters, 2014. **14**(2): p. 982-986.
163. Stepanova, M. and S. Dew, *Nanofabrication: techniques and principles.* 2011: Springer Science & Business Media.
164. Jansen, H., et al., *A survey on the reactive ion etching of silicon in microtechnology.* Journal of micromechanics and microengineering, 1996. **6**(1): p. 14.

165.	Jamali, M., et al., *Microscopic diamond solid-immersion-lenses fabricated around single defect centers by focused ion beam milling.* Review of Scientific Instruments, 2014. **85**(12): p. 123703.

166.	Zhong, T., et al., *Nanophotonic coherent light–matter interfaces based on rare-earth-doped crystals.* Nature communications, 2015. **6**(1): p. 1-6.

167.	Babinec, T.M., et al., *A diamond nanowire single-photon source.* Nature nanotechnology, 2010. **5**(3): p. 195-199.

168.	Li, C., et al., *Integration of hBN quantum emitters in monolithically fabricated waveguides.* ACS Photonics, 2021. **8**(10): p. 2966-2972.

169.	Lu, X., J.Y. Lee, and Q. Lin, *High-frequency and high-quality silicon carbide optomechanical microresonators.* Scientific reports, 2015. **5**(1): p. 1-9.

170.	Burek, M.J., et al., *High quality-factor optical nanocavities in bulk single-crystal diamond.* Nature communications, 2014. **5**(1): p. 1-7.

171.	Verre, R., et al., *Transition metal dichalcogenide nanodisks as high-index dielectric Mie nanoresonators.* Nature nanotechnology, 2019. **14**(7): p. 679-683.

172.	Takahashi, S., et al., *Direct creation of three-dimensional photonic crystals by a top-down approach.* Nature materials, 2009. **8**(9): p. 721-725.

173.	Wan, N.H., et al., *Large-scale integration of artificial atoms in hybrid photonic circuits.* Nature, 2020. **583**(7815): p. 226-231.

174.	Bhaskar, M.K., et al., *Experimental demonstration of memory-enhanced quantum communication.* Nature, 2020. **580**(7801): p. 60-64.

175.	Bhaskar, M.K., et al., *Quantum nonlinear optics with a germanium-vacancy color center in a nanoscale diamond waveguide.* Physical review letters, 2017. **118**(22): p. 223603.

176.	Hausmann, B.J., et al., *Integrated high-quality factor optical resonators in diamond.* Nano letters, 2013. **13**(5): p. 1898-1902.

177.	Mi, S., et al., *Integrated photonic devices in single crystal diamond.* Journal of Physics: Photonics, 2020. **2**(4): p. 042001.

178.	Dory, C., et al., *Inverse-designed diamond photonics.* Nature communications, 2019. **10**(1): p. 1-7.

179.	Aharonovich, I., A.D. Greentree, and S. Prawer, *Diamond photonics.* Nature Photonics, 2011. **5**(7): p. 397-405.

180.	Faraon, A., et al., *Resonant enhancement of the zero-phonon emission from a colour centre in a diamond cavity.* Nature Photonics, 2011. **5**(5): p. 301-305.

181.	Zhang, X. and E. Hu, *Templated growth of diamond optical resonators via plasma-enhanced chemical vapor deposition.* Applied Physics Letters, 2016. **109**(8): p. 081101.

182.	Jaffe, T., et al., *Deterministic Arrays of Epitaxially Grown Diamond Nanopyramids with Embedded Silicon-Vacancy Centers.* Advanced optical materials, 2019. **7**(2): p. 1800715.

183.	Sovyk, D., et al., *Growth of CVD diamond nanopillars with imbedded silicon-vacancy color centers.* Optical Materials, 2016. **61**: p. 25-29.

184.	Wang, C.-F., et al., *Fabrication and characterization of two-dimensional photonic crystal microcavities in nanocrystalline diamond.* Applied Physics Letters, 2007. **91**(20): p. 201112.

185. Yang, J.-K., et al., *Photonic-band-gap effects in two-dimensional polycrystalline and amorphous structures.* Physical Review A, 2010. **82**(5): p. 053838.
186. Ondič, L., et al., *Photonic crystal cavity-enhanced emission from silicon vacancy centers in polycrystalline diamond achieved without postfabrication fine-tuning.* Nanoscale, 2020. **12**(24): p. 13055-13063.
187. Williams, O.A., *Nanocrystalline diamond.* Diamond and Related Materials, 2011. **20**(5-6): p. 621-640.
188. Sartori, A.F., et al., *Inkjet‐Printed High‐Q Nanocrystalline Diamond Resonators.* Small, 2019. **15**(4): p. 1803774.
189. Checoury, X., et al., *Nanocrystalline diamond photonics platform with high quality factor photonic crystal cavities.* Applied Physics Letters, 2012. **101**(17): p. 171115.
190. Rath, P., et al., *Diamond as a material for monolithically integrated optical and optomechanical devices.* physica status solidi (a), 2015. **212**(11): p. 2385-2399.
191. Iwasaki, T., et al., *Germanium-vacancy single color centers in diamond.* Scientific reports, 2015. **5**(1): p. 1-7.
192. Chen, D., et al., *Optical gating of resonance fluorescence from a single germanium vacancy color center in diamond.* Physical review letters, 2019. **123**(3): p. 033602.
193. Siyushev, P., et al., *Optical and microwave control of germanium-vacancy center spins in diamond.* Physical Review B, 2017. **96**(8): p. 081201.
194. Ondič, L.s., et al., *Enhanced extraction of silicon-vacancy centers light emission using bottom-up engineered polycrystalline diamond photonic crystal slabs.* ACS nano, 2017. **11**(3): p. 2972-2981.
195. Schmidt, A., et al., *Fabrication of highly dense arrays of nanocrystalline diamond nanopillars with integrated silicon-vacancy color centers during the growth.* Optical Materials Express, 2019. **9**(12): p. 4545-4555.
196. Sedov, V., et al., *Growth of polycrystalline and single-crystal CVD diamonds with bright photoluminescence of Ge-V color centers using germane GeH4 as the dopant source.* Diamond and Related Materials, 2018. **90**: p. 47-53.
197. Shimoni, O., et al., *Development of a templated approach to fabricate diamond patterns on various substrates.* ACS applied materials & interfaces, 2014. **6**(11): p. 8894-8902.
198. Sartori, A.F., et al., *Template-assisted bottom-up growth of nanocrystalline diamond micropillar arrays.* Diamond and Related Materials, 2019. **95**: p. 20-27.
199. Gracio, J., Q. Fan, and J. Madaleno, *Diamond growth by chemical vapour deposition.* Journal of Physics D: Applied Physics, 2010. **43**(37): p. 374017.
200. Brinza, O., et al., *Dependence of CVD diamond growth rate on substrate orientation as a function of process parameters in the high microwave power density regime.* physica status solidi (a), 2008. **205**(9): p. 2114-2120.
201. Nishibayashi, Y., et al., *Homoepitaxial growth on fine columns of single crystal diamond for a field emitter.* Diamond and Related Materials, 2000. **9**(3-6): p. 290-294.
202. Schreck, M., et al., *Large-area high-quality single crystal diamond.* Mrs Bulletin, 2014. **39**(6): p. 504-510.
203. Schreck, M., et al., *Mosaicity reduction during growth of heteroepitaxial diamond films on iridium buffer layers: Experimental results and numerical simulations.* Journal of applied physics, 2002. **91**(2): p. 676-685.

204. Westerhausen, M.T., et al., *Controlled doping of GeV and SnV color centers in diamond using chemical vapor deposition.* ACS applied materials & interfaces, 2020. **12**(26): p. 29700-29705.

205. Gil, B., et al., *Boron nitride for excitonics, nano photonics, and quantum technologies.* Nanophotonics, 2020. **9**(11): p. 3483-3504.

206. Comtet, J., et al., *Direct observation of water-mediated single-proton transport between hBN surface defects.* Nature Nanotechnology, 2020. **15**(7): p. 598-604.

207. Fournier, C., et al., *Position-controlled quantum emitters with reproducible emission wavelength in hexagonal boron nitride.* Nature Communications, 2021. **12**(1): p. 3779.

208. Stern, H.L., et al., *Room-temperature optically detected magnetic resonance of single defects in hexagonal boron nitride.* Nat Commun, 2022. **13**(1): p. 618.

209. Chejanovsky, N., et al., *Single-spin resonance in a van der Waals embedded paramagnetic defect.* Nat Mater, 2021. **20**(8): p. 1079-1084.

210. Gottscholl, A., et al., *Initialization and read-out of intrinsic spin defects in a van der Waals crystal at room temperature.* Nat Mater, 2020. **19**(5): p. 540-545.

211. Gao, X., et al., *High-Contrast Plasmonic-Enhanced Shallow Spin Defects in Hexagonal Boron Nitride for Quantum Sensing.* Nano Lett, 2021. **21**(18): p. 7708-7714.

212. Guo, N.-J., et al., *Generation of Spin Defects by Ion Implantation in Hexagonal Boron Nitride.* ACS Omega, 2022. **7**(2): p. 1733-1739.

213. Kianinia, M., et al., *Generation of Spin Defects in Hexagonal Boron Nitride.* ACS Photonics, 2020. **7**(8): p. 2147-2152.

214. Ivády, V., et al., *Ab initio theory of the negatively charged boron vacancy qubit in hexagonal boron nitride.* npj Computational Materials, 2020. **6**(1): p. 41.

215. Gottscholl, A., et al., *Room temperature coherent control of spin defects in hexagonal boron nitride.* Sci Adv, 2021. **7**(14): p. eabf3630.

216. Gottscholl, A., et al., *Spin defects in hBN as promising temperature, pressure and magnetic field quantum sensors.* Nature Communications, 2021. **12**(1): p. 1-8.

217. Curie, D., et al., *Correlative nanoscale imaging of strained hBN spin defects.* arXiv preprint arXiv:2203.10075, 2022.

218. Auburger, P. and A. Gali, *Towards ab initio identification of paramagnetic substitutional carbon defects in hexagonal boron nitride acting as quantum bits.* Physical Review B, 2021. **104**(7): p. 075410.

219. Yang, T., et al., *Spin defects in hexagonal boron nitride for strain sensing on nanopillar arrays.* Nanoscale, 2022. **14**(13): p. 5239-5244.

220. Qian, C., et al., *Unveiling the Zero-Phonon Line of the Boron Vacancy Center by Cavity Enhanced Emission.* arXiv preprint arXiv:2202.10980, 2022.

221. Baber, S., et al., *Excited State Spectroscopy of Boron Vacancy Defects in Hexagonal Boron Nitride Using Time-Resolved Optically Detected Magnetic Resonance.* Nano Letters, 2022. **22**(1): p. 461-467.

222. Yu, P., et al., *Excited-State Spectroscopy of Spin Defects in Hexagonal Boron Nitride.* Nano Letters, 2022.

223. Mathur, N., et al., *Excited-state spin-resonance spectroscopy of V$_B$ defect centers in hexagonal boron nitride.* https://arxiv.org/abs/2111.10855, 2021.

224. Mendelson, N., et al., *Coupling Spin Defects in a Layered Material to Nanoscale Plasmonic Cavities.* Adv Mater, 2022. **34**(1): p. e2106046.

225. Khelifa, R., et al., *Coupling Interlayer Excitons to Whispering Gallery Modes in van der Waals Heterostructures.* Nano Lett, 2020. **20**(8): p. 6155-6161.

226. Ye, Y., et al., *Monolayer excitonic laser.* Nature Photonics, 2015. **9**(11): p. 733-737.

227. Wang, L., et al., *2D-material-integrated whispering-gallery-mode microcavity.* Photonics Research, 2019. **7**(8): p. 905-916.

228. Choy, J.T., et al., *Integrated TiO 2 resonators for visible photonics.* Optics letters, 2012. **37**(4): p. 539-541.

229. Evans, C.C., C. Liu, and J. Suntivich, *TiO2 nanophotonic sensors for efficient integrated evanescent Raman spectroscopy.* Acs Photonics, 2016. **3**(9): p. 1662-1669.

230. Qiu, F., A.M. Spring, and S. Yokoyama, *Athermal and high-Q hybrid TiO2–Si3N4 ring resonator via an etching-free fabrication technique.* ACS Photonics, 2015. **2**(3): p. 405-409.

231. Proscia, N.V., et al., *Microcavity-coupled emitters in hexagonal boron nitride.* Nanophotonics, 2020. **9**(9): p. 2937-2944.

232. Bradley, J.D., et al., *Submicrometer-wide amorphous and polycrystalline anatase TiO 2 waveguides for microphotonic devices.* Optics express, 2012. **20**(21): p. 23821-23831.

233. Reithmaier, J.P., et al., *Strong coupling in a single quantum dot–semiconductor microcavity system.* Nature, 2004. **432**(7014): p. 197-200.

234. Yoshie, T., et al., *Vacuum Rabi splitting with a single quantum dot in a photonic crystal nanocavity.* Nature, 2004. **432**(7014): p. 200-203.

235. Chikkaraddy, R., et al., *Single-molecule strong coupling at room temperature in plasmonic nanocavities.* Nature, 2016. **535**(7610): p. 127-130.

236. Kleemann, M.-E., et al., *Strong-coupling of WSe2 in ultra-compact plasmonic nanocavities at room temperature.* Nature communications, 2017. **8**(1): p. 1-7.

237. Xu, X. and S. Jin, *Strong coupling of single quantum dots with low-refractive-index/high-refractive-index materials at room temperature.* Science advances, 2020. **6**(47): p. eabb3095.

238. Von Neumann, J. and E. Wigner, *Über merkwürdige diskrete Eigenwerte Phys. Z,* 1929. **30**(524): p. 465-467.

239. Stillinger, F.H. and D.R. Herrick, *Bound states in the continuum.* Physical Review A, 1975. **11**(2): p. 446.

240. Marinica, D., A. Borisov, and S. Shabanov, *Bound states in the continuum in photonics.* Physical review letters, 2008. **100**(18): p. 183902.

241. Bulgakov, E.N. and A.F. Sadreev, *Bound states in the continuum in photonic waveguides inspired by defects.* Physical Review B, 2008. **78**(7): p. 075105.

242. Hsu, C.W., et al., *Observation of trapped light within the radiation continuum.* Nature, 2013. **499**(7457): p. 188-191.

243. Monticone, F. and A. Alu, *Embedded photonic eigenvalues in 3D nanostructures.* Physical Review Letters, 2014. **112**(21): p. 213903.

244. Rybin, M.V., et al., *High-Q supercavity modes in subwavelength dielectric resonators.* Physical review letters, 2017. **119**(24): p. 243901.

245. Azzam, S.I. and A.V. Kildishev, *Photonic bound states in the continuum: from basics to applications.* Advanced Optical Materials, 2021. **9**(1): p. 2001469.

246. Hsu, C.W., et al., *Bound states in the continuum.* Nature Reviews Materials, 2016. **1**(9): p. 1-13.

247. Bernhardt, N., et al., *Quasi-BIC resonant enhancement of second-harmonic generation in WS2 monolayers.* Nano Letters, 2020. **20**(7): p. 5309-5314.

248. Kravtsov, V., et al., *Nonlinear polaritons in a monolayer semiconductor coupled to optical bound states in the continuum.* Light: Science & Applications, 2020. **9**(1): p. 1-8.

249. Hu, L., et al., *Quasi-BIC Enhanced Broadband Terahertz Generation in All-Dielectric Metasurface.* Advanced Optical Materials, 2022: p. 2200193.

250. Koshelev, K., et al., *Asymmetric metasurfaces with high-Q resonances governed by bound states in the continuum.* Physical review letters, 2018. **121**(19): p. 193903.

251. Kodigala, A., et al., *Lasing action from photonic bound states in continuum.* Nature, 2017. **541**(7636): p. 196-199.

252. Ha, S.T., et al., *Directional lasing in resonant semiconductor nanoantenna arrays.* Nature nanotechnology, 2018. **13**(11): p. 1042-1047.

253. Ardizzone, V., et al., *Polariton Bose–Einstein condensate from a bound state in the continuum.* Nature, 2022. **605**(7910): p. 447-452.

254. Papasimakis, N., et al., *Electromagnetic toroidal excitations in matter and free space.* Nature materials, 2016. **15**(3): p. 263-271.

255. Kuznetsov, A.I., et al., *Optically resonant dielectric nanostructures.* Science, 2016. **354**(6314): p. aag2472.

256. Chugh, D., et al., *Flow modulation epitaxy of hexagonal boron nitride.* 2D Materials, 2018. **5**(4): p. 045018.

257. Wu, M., et al., *Room-temperature lasing in colloidal nanoplatelets via mie-resonant bound states in the continuum.* Nano Letters, 2020. **20**(8): p. 6005-6011.

258. Auffèves, A., et al., *Spontaneous emission spectrum of a two-level atom in a very-high-Q cavity.* Physical Review A, 2008. **77**(6): p. 063833.

259. Frey, L., C. Lehrer, and H. Ryssel, *Nanoscale effects in focused ion beam processing.* Applied physics A, 2003. **76**(7): p. 1017-1023.

260. Chen, Y., et al., *Generation of High-Density Quantum Emitters in High-Quality, Exfoliated Hexagonal Boron Nitride.* ACS Applied Materials & Interfaces, 2021. **13**(39): p. 47283-47292.

261. Eremchev, I.Y., et al., *Microscopic Insight into the Inhomogeneous Broadening of Zero-Phonon Lines of GeV–Color Centers in Chemical Vapor Deposition Diamond Films Synthesized from Gaseous Germane.* The Journal of Physical Chemistry C, 2021. **125**(32): p. 17774-17785.

262. Ohno, K., et al., *Engineering shallow spins in diamond with nitrogen delta-doping.* Applied Physics Letters, 2012. **101**(8): p. 082413.

263. Sipahigil, A., et al., *An integrated diamond nanophotonics platform for quantum-optical networks.* Science, 2016. **354**(6314): p. 847-850.